Development of Ion Mobility Mass Spectrometry Instrumentation to Investigate
the Gas-Phase Structures of Protein and Protein Complex Ions

Samuel J. Allen

A dissertation

submitted in partial fulfillment of the

requirements for the degree of

Doctor of Philosophy

University of Washington

2017

Reading Committee:

Matthew F. Bush, Chair

Robert E. Synovec

Joshua C. Vaughan

Program Authorized to Offer Degree:

Chemistry

University of Washington

Abstract

Development of Ion Mobility Mass Spectrometry Instrumentation to Investigate the Gas-Phase
Structures of Protein and Protein Complex Ions

Samuel J. Allen

Chair of Supervisory Committee:
Assistant Professor Matthew F. Bush
Department of Chemistry

This dissertation reports the development of new ion mobility mass spectrometry (IM-MS) instrumentation to analyze protein and protein complex ions. IM-MS is a gas-phase analytical technique that separate ions based on their collision cross section (a description of ion shape) and mass-to-charge ratio. Electrospray ionization of samples from buffered solutions at biologically relevant pH generates "native-like" protein ions, which retain noncovalent interactions and compact conformations. IM-MS analysis enables the determination of the shape and assembly of native-like ions, which can be used to infer information about the solution conformations of biomolecules. New IM devices were developed to improve the informational content obtained from IM-MS experiments. First, an RF-confining drift cell was developed and

implemented in a commercial mass spectrometer. Experimental results and ion trajectories implemented using SIMION were used to describe the separation principles of ions in RF-confining drift cells. Those results show that RF-confining drift cells separate ions similarly to traditional IM devices and that applied RF potentials have minimal effects on the effective temperatures of gas-phase ions. The RF-confining drift cells was used to report collision cross sections for 349 ions, 155 of which are for ions that have not been characterized previously using IM. The effects of ionization conditions and analyte solutions on the charge states and collision cross sections of ions was also investigated. An additional IM device based on Structures for Lossless Ion Manipulations (SLIM) was developed. SLIM is an emerging IM technology that can be implemented as modular platforms to perform ion separations, filtering, and trapping. The first collision cross sections determined using SLIM are reported. IM analysis of native-like protein ions shows that those ions exhibit significant structural heterogeneity in the gas-phase. To evaluate the stability and dynamics of native-like protein ions, IM-IM-MS functionality was implemented into the SLIM device. Dynamic gas-phase conformations were observed for native-like protein ions, which has significant implications for the broader community's interpretation of IM-MS results. The stability of structural subpopulations of native-like ions was investigated as a function of gas-phase ion lifetime at near-ambient temperatures. The conformations of subpopulations evolve continuously in the gas-phase, but even after 4 seconds, the subpopulations exhibit different distributions of collision cross sections. This suggests that native-like ions in IM-MS experiments can retain some memory of their initial gas-phase structures for up to seconds at near-ambient temperature.

Dedication

To my family.

Acknowledgements

I would like to thank my advisor, Prof. Matthew F. Bush, for the extensive mentorship and guidance during my PhD. He gave me the freedom to pursue what I wanted and provided numerous opportunities to advance my career. I would also like to thank Prof. Robert Synovec, Joshua Vaughan, James Bruce, Frantisek Turecek, Dustin Maly, Bo Zhang, and Daniel Chiu for serving on my academic committees and providing valuable discussions related to my research.

The instrumentation that I developed was enabled by tremendously experienced and helpful engineers at the University of Washington. Bob Scott (now at UW Physics - Instrument Shop Manager), John Heutnik (retired, UW Chemistry - Instrument Maker), Ed McArthur (retired, UW Chemistry - Instrument Maker), and Pat McCrory (UW APL - Machine Shop Manager) fabricated the majority of the SLIM instrument. Eric Strakbein (UW Chemistry - Facilities and Machine Shop Manager) and Brian Wadey (UW Chemistry - Instrument Maker) were extremely helpful and responsive with design considerations and fabrication of a new instrument that I helped design. Electronics Shop research engineers Lon Buck, William Beaty, and Roy Olund created several electronics that were used in instruments I developed, and were always present to loan test equipment or impart expert electrical engineering advice. I would also like to thank the SLIM consortium at Pacific Northwest National Laboratory, including Dr. Richard Smith, Dr. Yehia Ibrahim, Dr. Randy Norheim, Dr. Tsung-Chi Chen (now at ThermoFisher Scientific), Spencer Prost, and Dr. Ian Webb for sharing designs, software, and technical expertise. I would also like to specifically thank Dr. Gordon Anderson (GAA Custom Engineering) who was present for the first ion signal the SLIM instrument and was always available to assist me in troubleshooting. Kevin Giles and Tony Gilbert (Waters Corporation) fabricated the RF-confining drift cell and helped me obtain my first ion mobility results.

Lastly, thank you to my wife, Sonja. In the chaos that is graduate school, she gave me clarity, compassion, and our beautiful son Leo. This time in graduate school will be a footnote in the grander story of our lives.

Nomenclature

CRM	Charged-Residue Model
Da	Dalton, the unified atomic mass unit
DC	Direct Current
e	elementary charge, $1.6021766208(98) \times 10^{-19}$ C
E	Electric Field
electrodynamic	referring to time-dependent electric potentials
electrostatic	referring to time-independent electric potentials
$E \cdot P^{-1}$	drift field strength: electric field divided by pressure, $V \cdot cm^{-1} \cdot Torr^{-1}$
ESI	Electrospray Ionization
He	helium, in reference to IM buffer gas
IM	Ion Mobility
k_B	Boltzmann's constant, $1.38064852(79) \times 10^{-23}$ $J \cdot K^{-1}$
μ	reduced mass, often between ion and neutral masses
MS	Mass Spectrometry
m/z	mass-to-charge ratio, the standard measurement unit in MS
N_2	nitrogen, in reference to IMS buffer gas
Ω	ion-neutral collision cross section
RF	Radio-Frequency, referring the frequency of AC potentials
SIMION	Ion and Electron Optics Simulator
SLIM	Structures for Lossless Ion Manipulations
t_D	drift time
T_{eff}	Effective Temperature
TOF	time-of-flight, an MS analyzer
V_{PP}	Peak-to-Peak Voltage, referring to the amplitudes of RF potentials
z	ion charge state

Table of Contents

CHAPTER 1

***

Introduction

1.1 General Overview

  The structures and interactions of proteins and protein complexes define the biological functions of organisms.[1] Condensed-phase structural biology approaches are used to determine protein structures, but those approaches can be laborious and highly dependent on sample quality. For example, structural determination using X-ray crystallography, a gold-standard structural biology technique, can be interrupted at each step between purifying the sample to solving the diffraction data.[2] An alternative approach to determining the structures and assemblies of proteins is ion mobility mass spectrometry (IM-MS). IM-MS is a gas-phase analytical technique that utilizes the benefits of MS (*e.g.*, speed, sensitivity, selectivity) and IM (*e.g.*, separation of ions based on shape) to generate a two-dimensional gas-phase separation based on the mass-to-charge ratio and shape of the ion. Advances in IM-MS theory, methodology, and instrumentation are critical to enable complementary structural biology tools to evaluate the structures of proteins. In this dissertation, new IM-MS technologies are developed to investigate the gas-phase structures of proteins and protein complexes. The results of this work describe the effects of different ionization conditions on protein structure, a statistical model to evaluate the effective temperature of ions, and the dynamic conformations of ensembles of structures observed in IM-MS analysis of proteins and protein complexes.

1.2 Mass Spectrometry

Mass spectrometry (MS) is a gas-phase analytical technique that isolates ions based on their mass-to-charge (m/z) ratio. All MS instrumentation, in its most basic form, consists of an ion source, analyzer, and detector. The two commonly used ionization techniques for MS are matrix-assisted laser desorption ionization (MALDI)[3] and electrospray ionization (ESI).[4,5] Both are soft ionization techniques that preserve intact protein samples. Generally, MALDI produces singly-charged ions, whereas ESI generates a distribution of multiply-charged ions. The range of charge states produced by ESI results in ions with lower m/z values, which enables analysis on low m/z analyzers. Additionally, ESI is a continuous ionization method and enables direct sampling of proteins from biologically relevant solutions. As a result, ESI is preferentially used for the ionization of protein samples.[6,7]

1.3 Electrospray Ionization of Protein Ions

In ESI, a solution containing the analyte is infused through a capillary emitter that is electrically biased by kilovolts relative to the inlet of the mass spectrometer. The electrical potential forms a Taylor Cone at the end of the capillary, which generates a plume of charged droplets.[8] The charged droplets desolvate and the resulting solvent-free ions are analyzed using a mass spectrometer. In the initial implementations of ESI, proteins were dissolved in acidified aqueous/organic solutions which produced broad distributions of highly charged ions.[9] Those highly charged ions correspond to denatured structures that exhibit extended conformations in the gas phase.[10,11] ESI of proteins from non-denaturing solutions was difficult in the early years of ESI due to the upper m/z limits of commonly used quadrupole mass analyzers. In 1993, Smith and coworkers developed an extended m/z range (~45000) quadrupole mass analyzer which was

used for the high *m/z* analysis of protein complex ions that retained noncovalent interactions.[12]

That study used ESI of concanavalin A (~103 kDa tetrameric protein complex) from buffered

solutions containing 10 mM ammonium acetate at pH = 6.7. The ions produced under those

conditions had a narrow charge-state distribution and lower charge states compared to ions

generated from denaturing solutions. This led to several studies[13–16] reporting the retention of

noncovalent interactions of protein ions electrosprayed from buffered solutions at biologically

relevant pH (native-like solutions), and later led to the burgeoning field of native MS.[6,17–19]

1.4 Charged-Residue Model

For protein and protein complex ions generated from ESI of native-like solutions, the

observed charge states have been shown to be correlated with mass[20,21] and solvent-accessible

surface area.[22] Those relationships are consistent with the Charged-Residue Model (CRM) for

ESI. In the CRM, initial charged droplets evaporate and undergo Coulombic fissions when the

charge repulsion exceeds the surface tension of the droplet (the Rayleigh Limit):[23]

$$z \cdot e = \pi(8\varepsilon_0\gamma)^{1/2} D^{3/2} \tag{1.1}$$

where z is the number of charges, e is the elementary charge, ε_0 is the permittivity of free space,

γ is the surface tension (72 mN/m for water at 25 °C), and D is the droplet diameter (often

calculated from the mass and an estimated density). Coulombic fissions produce progeny

droplets that undergo evaporation of the final solvent molecules and result in a solvent-free gas-

phase ion.

The CRM is a good approximation for describing the origin of most native-like protein

ion charge states, but there are some discrepancies between experimental results and those

predicted using the CRM. For example, proteins ions electrosprayed in positive or negative ion

mode result in different charge states,[21] yet Equation 1.1 does not contain a polarity-dependent variable. Additionally, adding salts,[24–26] basic molecules,[27] or supercharging reagents[28–30] can affect the observed charge states of protein ions without changing the size of ions (variable D in Equation 1.1). The origin of protein ion charge states produced from ESI of native-like solutions is still actively investigated through experimental results[31–33] and MD simulations.[34] Understanding how condensed-phase structures are transferred to the gas phase and how charge states affect protein structure are immensely important for conclusions to be drawn from native MS measurements.

1.5 Ion Mobility

    1.5.1 Theory. Ion mobility (IM) is a gas-phase technique that separates ions based on their shape and charge. Ions are separated by applying an electric potential to a drift region, which is often an enclosed chamber containing a neutral background gas. Ions achieve a steady-state drift velocity from the force balance of ion-neutral collisions and the applied electric field. The net drift velocity of ions (v_D) depends on the applied electric field (E) and the mobility of the ion (K):

$$v_D = KE = K\frac{V}{L} \tag{1.2}$$

where E is equal to the applied drift voltage (V) divided by the length of the drift region (L). By measuring ion drift times (t_D) over a range V, K values can be determined from the slopes of t_D versus reciprocal V plots:

$$t_D = \frac{L^2}{K}\frac{1}{V} \tag{1.3}$$

A critical restraint to this theory is the low-field limit,[35] which depends on the analyte diameter

(*d*) and charge (*z*), and defines the upper limit of drift field strength (*E/P*, V cm^{-1} Torr^{-1}) that can

be used to determine *K* of an ion:

$$\frac{E}{P} < \left(\frac{m}{m+M}\right)^{1/2} \frac{d^2}{ez} \quad (1.4)$$

Where *P* is the pressure, *m* is the mass of the ion, and *M* is the mass of the neutral drift gas. Ions

are within the low-field limit when their translational energy between collisions is less than the

thermal energy of the collision gas. Most importantly, *K* is independent of the applied drift

voltage under the low-field limit, *i.e.* t_D and reciprocal *V* are linearly related according to

Equation 1.3. These experiments can be used to extract structural information by converting the

measured *K* into a collision cross section (*Ω*) using the Mason-Schamp equation:[36]

$$\Omega = \frac{3ez}{16N} \left(\frac{2\pi}{\mu k_B T}\right)^{1/2} \frac{1}{K} \quad (1.5)$$

where *N* is the drift-gas number density, *μ* is the reduced mass of the ion and drift gas, k_B is the

Boltzmann constant, and *T* is the drift-gas temperature. To the first approximation, the *Ω*

describes the orientationally-averaged projection area of an ion-neutral pair.[36,37] Note, *Ω* values

also depend on long-range interactions of the ion-neutral pair, which is temperature dependent.[36-38]

1.5.2 Resolving Power. The conventional metric to describe the separation efficiency of

IM devices is the single-peak, diffusion-limited resolving power. The diffusion-limited resolving

power depends on the thermal diffusion along the axis of transmission:[39,40]

$$\frac{t_D}{\Delta t_{diff}} = \frac{1}{4} \left(\frac{Vez}{k_B T \ln 2}\right)^{1/2} \quad (1.6)$$

where Δt_{diff} is the full width at half maximum of the drift-time distribution. Maximizing the

resolving power of IM devices is critical for differentiating species with similar mobilities, and is

thus an important parameter in the optimization and design of new IM instrumentation. According to Equation 1.6, higher resolving power mobility measurements can be achieved using higher drift voltages. Though, electrical discharge limits the maximum voltage that can be applied to nearby electrodes. Electrical discharge occurs when appropriate pressures and nearby potentials (defined by Paschen curves) enable a plasma path,[41] which can be damaging to ion optics. To overcome electrical discharge, the length of the drift region is increased in order to use higher drift voltages. This decreases the relative difference in voltage of nearby ion optics, thereby preventing conditions in which electrical discharge can occur. Other strategies include doping the background gas with molecules, such as SF_6,[42] that have favorable electrical discharge properties. The apparent resolving power of gas-phase ions can also depend on other sources of broadening including field inhomogeneity, space-charge effects, inelastic ion-neutral collisions, and ion gating.[39,40]

1.6 Ion Mobility Mass Spectrometry

It was not until the early 1990s, after the invention of ESI,[9] that IM-MS was used to determine the structures of protein ions. Douglas and French estimated a theoretical Ω value of myglobin using Monte Carlo simulations of the energy loss process for ions passing through a conventional two-dimensional quadrupole.[43] Later, Covey and Douglas used a triple quadrupole instrument to show one of the first examples of experimentally determined Ω values of protein ions.[44] That study showed the utility of Ω values to describe the gas-phase behavior of protein ions, and also noted that protein ion conformations depend on charge state. At this point in time, researchers began noting the utility of Ω analysis of protein ions.[45–47] The remainder of the 1990s saw custom-built IM instruments that were coupled to mass spectrometers. Those instruments

were used to conduct IM-MS measurements of several proteins including cytochrome *c*,[48] myoglobin,[49] and others.[50,51] Later, the release of first commercial IM-MS instrument[52] enabled one of the first examples of IM-MS analysis of a native-like protein complex,[53] which showed that noncovalent interactions and compact conformations of proteins are preserved in those experiments.

1.6.1 Instrumentation. Traditionally, IM devices are coupled to time-of-flight (ToF) mass analyzers due to their relatively short timescales of mass analysis, which increases duty cycle. IM separations occur on the millisecond timescale while ToF separations occur on the microsecond timescale. Thus, hundreds to thousands of mass spectra can be measured for a single IM separation. Coupling an IM device to a ToF analyzer was first described in 1967 by McAfee et al.[54] Later, IM devices were coupled to orthogonal-acceleration ToF analyzers which enabled improved ion sampling from continuous ion sources (*e.g.*, ESI) and higher mass spectral resolution.[55]

Early IM implementations have been reviewed previously.[56–59] Here, the discussion of IM instruments is limited to low-pressure devices (1 to 15 Torr) that are used to study biomolecular ions. Electrostatic ion mobility devices, often called drift tubes, consist of a series of stacked-ring electrodes that are connected to a voltage divider network (Figure 1.1A).[42,60–65] Direct current (DC) potentials are applied to the voltage divider network to create a uniform DC gradient, which acts as the electric field that separates ions according to Equation 1.2. As ions traverse the drift region in electrostatic drift tubes, diffusion in the radial direction occurs due to collisions with the background gas. Early implementations of drift tubes suffered from low ion transmission due to radial diffusion, especially at lower applied electric fields. To correct for radial diffusion, electrostatic lenses[50,66–68] or ion funnels[42,61,63,64] were implemented onto the

back-end of several electrostatic drift tubes. Ion funnels are electrodynamic devices that contain incrementally decreasing internal-diameter ring electrodes.[69,70] A uniform DC gradient is applied to the electrodes in addition to alternating radio-frequency (RF) potentials (electrodynamic potentials) which are used to establish a pseudopotential that radially confines ions, similar to a stacked-ring ion guide.[71] The introduction of ion funnels to IM enabled more efficient ion trapping for mobility injection[72] and IM measurements with extended path lengths. Examples of the latter include instruments built by Clemmer and coworkers that used ion funnels to transfer ions between consecutive drift tubes to enable multidimensional IM, *e.g.*, IM-IM[73] and IM-IM-IM.[74] Additionally, a cyclical drift tube used ion funnels to refocus ions that traveled over a circular path, and showed substantially higher resolving powers than observed in previous IM instrumentation.[75–77]

The instruments described above generated much of the pioneering IM data that has formed our understanding of protein ions, but those investigations were limited to research groups that custom-built IM instruments. In 2005, Waters Corporation released the first commercially available IM-MS instrument, the Synapt HDMS, which is a hybrid traveling-wave IM/ToF instrument.[52] Traveling-wave IM uses time-dependent DC potentials to separate ions. The time-dependent potentials propagate across a series of stacked-ring electrodes with a defined velocity and amplitude.[78] Alternating RF potentials are also applied to the ring electrodes to radially confine ions, which improves ion transmission. Later, longer path lengths and higher traveling-wave amplitudes in a second-generation traveling-wave commercial instrument improved the separation capabilities relative to the first-generation instrument.[79,80] Traveling-wave IM enabled the broader analytical chemistry community to conduct IM experiments, which has led to IM-MS measurements of lipids,[81] peptides,[82,83] proteins,[84–86] and protein

complexes.[53,87] Although, because ions are separated in a non-uniform DC electric field, ion drift

times are no longer proportional to the electric field as described in Equation 1.3. Drift time

calibration using appropriate calibrants of known Ω values is required in traveling-wave IM

experiments to determine accurate Ω values.[88,89]
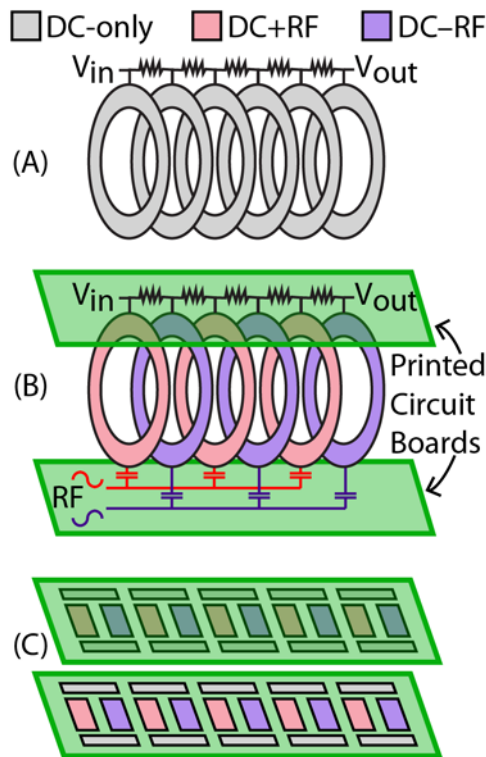
Figure 1.1. (A) Electrostatic drift tube. (B) RF-confining drift cell. (C) Structures

for Lossless Ion Manipulations (SLIM).

To circumvent the requirement of drift time calibrations for IM separations performed in

a Waters Synapt HDMS, Bush et al. developed an RF-confining drift cell to directly measure the

mobilities of ions.[89] That drift cell replaced a traveling-wave IM device in a Waters Synapt G1

HDMS. In RF-confining drift cells, a uniform DC gradient and alternating RF potentials are

applied to a series of stacked-ring electrodes (Figure 1.1B). This device retains the benefits of

traditional drift tubes in which ions are separated according to Equation 1.2, but also improves ion transmission by utilizing RF confinement on all ring electrodes. Increasing ion transmission by RF confinement has been implemented in other IM devices including segmented-quadrupoles,[90–93] modified triple quadrupole instruments,[44,94] a stacked-ring ion guide with an applied staircase-like DC gradient,[95] trapped IM cells,[96] a gridless-overtone mobility cell,[97] and Structures for Lossless Ion Manipulations (SLIM).[98]

SLIM is an emerging IM technology based on batch-fabricated, low-cost printed circuit board technology. In contrast to stacked-ring electrode IM devices, SLIM is composed of parallel pairs of printed circuit boards that deliver potentials to planar electrodes deposited directly onto the boards (Figure 1.1C).[99,100] Initially, SLIM was implemented as 7.62 x 7.62 cm boards that were stacked with a board-to-board spacing of 3 to 6 mm. Those boards use a uniform DC gradient to establish electric fields for IM separations and a combination of DC and RF potentials to confine ions. Arrays of SLIM boards are connected and can be used as an alternative to a stacked-ring electrode design for IM separations.[99] Owing to the modular nature of SLIM, boards with different planar electrode paths can be implemented. For example, a SLIM "switch" contains a linear and an orthogonal path of planar electrodes.[101,102] Using time-dependent potentials, the switch can be pulsed to selectively divert specific ions from the linear path to the orthogonal path. This enables IM experiments in which a specific ion can be selectively eliminated or enriched.[101,103,104] Non-uniform DC gradients can also be used to generate traveling-waves to separate ions.[105–107] SLIM traveling-wave devices have been used to separate ions along a 13 m serpentine path.[108] SLIM boards with new functionality are still being developed,[109,110] and the growing versatility and modularity of these designs will aid in the design of future IM instrumentation.

1.6.2 Applications to Native-Like Protein Ions. The efforts outlined above, including ESI from native-like solutions and improvements in IM-MS separations, worked in concert to develop technologies capable of performing IM-MS measurements of intact proteins and protein complexes. Notable examples of native IM-MS include structure and assembly determination of membrane-bound proteins,[87,111,112] intrinsically-disordered proteins,[113–115] virus capsids,[116,117] and protein aggregates related to neurodegenerative diseases.[118,119] A debate still remains related to the exact chemistry that occurs during the gas-phase lifetimes of ions,[120] but experiments have shown that gas-phase ions can retain some memory of their condensed-phase structures.[121–124] Additionally, compact Ω values determined from native IM-MS experiments have been shown to correlate well with Ω values calculated from crystal structures.[53,117,125,126]

IM-MS has also been used in tandem to other gas-phase techniques such as collision induced unfolding (CIU). In CIU, ions are accelerated into a chamber containing a neutral gas. Collisional activation increases the internal energy of the ions which can result in gas-phase structural changes that are monitored using IM. For example, CIU of native-like protein complexes shows stable, unfolded conformations at increasing energies.[127] In some examples, noncovalent adducts[128] or ligands[129] can stabilize compact conformations and mitigate the extent of gas-phase unfolding. Additionally, CIU experiments of some protein complexes show that activation can result in a more compact conformation, the extent of which is highly correlated with the charge state and native structure of the ion.[130,131] The exact mechanism of CIU and the inherent protein contributions to gas-phase stability are still debated.[132–134] These examples of CIU show that gas-phase ions contain a conformational landscape that is defined by barriers of isomerization to more energetically-stable structures, and that the properties of the ion (*e.g.*, charge state, bound ligands, etc.) can affect those barriers.

Several studies have shown that IM-MS of protein ions can result in IM distributions that are broader than expected based on diffusion-limited theory (Δt_{diff} in Equation 1.6).[50,121,135,136] Using multidimensional IM techniques, Clemmer and coworkers showed that broad IM distributions of protein ions consist of an ensemble of structures that are stable on the millisecond timescale.[136] The origin of the structural heterogeneity observed for gas-phase ions and how those ensembles relate to condensed-phase structures is still not known. Robinson and coworkers have used broad IM distributions of protein complexes as an additional metric to compare the ensembles of structures in structural biology investigations.[87,137] Future native IM-MS investigations will benefit from an analytical understanding of the contributions to broad IM distributions of protein ions, but this requires advances in IM instrumentation and complementary techniques to evaluate the stability and conformational landscapes of gas-phase ions.

1.7 Outline of the Present Study

This dissertation focuses on the development and application of new IM-MS technologies to investigate the structures and charging of protein and protein complex ions. Ions are produced using ESI of native-like solutions to preserve noncovalent interactions and compact conformations of proteins. Ion trajectories implemented using SIMION are used to support and validate experimental results of ion transport in new IM-MS instrumentation.

Chapters 2 to 4 describe the development of new IM-MS instruments for determining the Ω values of gas-phase ions. Chapter 2 reports the fundamentals of ion separations in an RF-confining drift cell. Despite the use of electrodynamic potentials to radially confine ions, RF-confining drift cells separate ions similarly to an electrostatic drift tube. Additionally, a new

statistical approach is developed to evaluate the effective temperatures of gas-phase ions. This approach shows that electrodynamic potentials in RF-confining drift cells have a negligible effect on the temperatures of gas-phase ions, which is an important conclusion for other IM devices that use electrodynamic potentials.[79,96,97] Chapter 3 reports the design and implementation of a new RF-confining drift cell. IM-MS of native-like protein and protein complex ions indicate that structural heterogeneity in the gas phase limits the apparent resolving power of those measurements. Chapter 4 reports the design and implementation of a new IM-MS instrument based on Structures for Lossless Ion Manipulations (SLIM). SLIM is a recent IM technology that can be implemented as modular platforms to perform a variety of gas-phase experiments.[98,99,101] The first Ω values determined using SLIM are reported and those measurements represent the highest apparent resolving power measurements of a protein complex ion. This platform represents a significant advancement of IM-MS to study the native-like structures of protein ions.

Chapters 5 describes the application of SLIM to perform multidimensional IM separations in order to evaluate the structural heterogeneity and stability of gas-phase ions. Results from tandem IM of broad native-like IM distributions show that structural heterogeneity can bias the measured Ω distributions in tandem IM experiments, which has implications for previous tandem IM implementations.[73,74] Chapter 5 reports the application of SLIM tandem IM to investigate the gas-phase stability and dynamics of native-like cytochrome *c* ions at near-ambient temperature. Currently, the interpretation of most native IM-MS experiments implicitly assumes that ion structures are static during experiments. In contrast, the results from this study show that the gas-phase structures of native-like ions evolve continuously on the tens to hundreds of milliseconds timescale. This outcome will require a critical evaluation of protein

characterization using different IM-MS instruments with similar timescales. Additionally, the structures of selected subpopulations evolve at different rates, which suggests that native-like ions retain some memory of their initial gas-phase structures for seconds at near-ambient temperature.

Chapters 6 and 7 focus on addressing the IM-MS community's unanswered questions relating to the effects of different ionization conditions on the Ω values of native-like protein ions. Chapter 6 reports Ω values and charge states for protein ions produced from ESI in either positive or negative ion mode. Using the same native solutions for ESI, different charge states, but similar Ω values, are observed for cations and anions. This suggests that the Ω values of native-like ions are independent of polarity. The differences in cation and anion charge states are attributed to the emission of ESI-polarity dependent charge-carriers during the final stages of droplet desolvation. Chapter 7 reports Ω values for several protein ions with enhanced charge states produced from ESI of supercharging solutions. Intermediate supercharged charge states can exhibit Ω values similar to native-like values. Although, the highest observed charge states have large Ω values which indicates a significant loss of native-like structure. These results address an ongoing debate as to the effects of supercharged charge states on the native-like structures of proteins ions, and provide insights into the mechanism of ion formation in those experiments.

1.8 References

(1)   Marsh, J. A.; Teichmann, S. A. Structure, Dynamics, Assembly, and Evolution of Protein Complexes. *Annu. Rev. Biochem.* **2015**, *84* (1), 551–575.
(2)   Stacy, R.; Begley, D. W.; Phan, I.; Staker, B. L.; Van Voorhis, W. C.; Varani, G.; Buchko, G. W.; Stewart, L. J.; Myler, P. J. Structural Genomics of Infectious Disease Drug Targets: The SSGCID. *Acta Crystallograph. Sect. F Struct. Biol. Cryst. Commun.* **2011**, *67* (9), 979–984.

(3)   Karas, M.; Hillenkamp, F. Laser Desorption Ionization of Proteins with Molecular Masses Exceeding 10,000 Daltons. *Anal. Chem.* **1988**, *60* (20), 2299–2301.

(4)   Dole, M. Molecular Beams of Macroions. *J. Chem. Phys.* **1968**, *49* (5), 2240.

(5)   Yamashita, M.; Fenn, J. B. Electrospray Ion Source. Another Variation on the Free-Jet Theme. *J. Phys. Chem.* **1984**, *88* (20), 4451–4459.

(6)   Heck, A. J. R. Native Mass Spectrometry: A Bridge between Interactomics and Structural Biology. *Nat. Methods* **2008**, *5* (11), 927–933.

(7)   Mehmood, S.; Allison, T. M.; Robinson, C. V. Mass Spectrometry of Protein Complexes: From Origins to Applications. *Annu. Rev. Phys. Chem.* **2015**, *66*, 453–474.

(8)   Gomez, A.; Tang, K. Charge and Fission of Droplets in Electrostatic Sprays. *Phys. Fluids* **1994**, *6* (1), 404–414.

(9)   Fenn, J. B.; Mann, M.; Meng, C. K.; Wong, S. F.; Whitehouse, C. M. Electrospray Ionization for Mass Spectrometry of Large Biomolecules. *Science* **1989**, *246* (4926), 64–71.

(10)   Chowdhury, S. K.; Katta, V.; Chait, B. T. Probing Conformational Changes in Proteins by Mass Spectrometry. *J. Am. Chem. Soc.* **1990**, *112* (24), 9012–9013.

(11)   Dobo, A.; Kaltashov, I. A. Detection of Multiple Protein Conformational Ensembles in Solution via Deconvolution of Charge-State Distributions in ESI MS. *Anal. Chem.* **2001**, *73* (20), 4763–4773.

(12)   Light-Wahl, K. J.; Winger, B. E.; Smith, R. D. Observation of the Multimeric Forms of Concanavalin A by Electrospray Ionization Mass Spectrometry. *J. Am. Chem. Soc.* **1993**, *115* (13), 5869–5870.

(13)   Schwartz, B. L.; Light-Wahl, K. J.; Smith, R. D. Observation of Noncovalent Complexes to the Avidin Tetramer by Electrospray Ionization Mass Spectrometry. *J. Am. Soc. Mass Spectrom.* **1994**, *5* (3), 201–204.

(14)   Schwartz, B. L.; Bruce, J. E.; Anderson, G. A.; Hofstadler, S. A.; Rockwood, A. L.; Smith, R. D.; Chilkoti, A.; Stayton, P. S. Dissociation of Tetrameric Ions of Noncovalent Streptavidin Complexes Formed by Electrospray Ionization. *J. Am. Soc. Mass Spectrom.* **1995**, *6* (6), 459–465.

(15)   Loo, J. A. Observation of Large Subunit Protein Complexes by Electrospray Ionization Mass Spectrometry. *J. Mass Spectrom.* **1995**, *30* (1), 180–183.

(16)   Eckart, K.; Spiess, J. Electrospray Ionization Mass Spectrometry of Biotin Binding to Streptavidin. *J. Am. Soc. Mass Spectrom.* **1995**, *6* (10), 912–919.

(17)   Zhou, M.; Sandercock, A. M.; Fraser, C. S.; Ridlova, G.; Stephens, E.; Schenauer, M. R.; Yokoi-Fong, T.; Barsky, D.; Leary, J. A.; Hershey, J. W.; et al. Mass Spectrometry Reveals Modularity and a Complete Subunit Interaction Map of the Eukaryotic Translation Factor eIF3. *Proc. Natl. Acad. Sci.* **2008**, *105* (47), 18139–18144.

(18)   Uetrecht, C.; Versluis, C.; Watts, N. R.; Roos, W. H.; Wuite, G. J. L.; Wingfield, P. T.; Steven, A. C.; Heck, A. J. R. High-Resolution Mass Spectrometry of Viral Assemblies: Molecular Composition and Stability of Dimorphic Hepatitis B Virus Capsids. *Proc. Natl. Acad. Sci.* **2008**, *105* (27), 9216–9220.

(19)   Boeri Erba, E.; Petosa, C. The Emerging Role of Native Mass Spectrometry in Characterizing the Structure and Dynamics of Macromolecular Complexes. *Protein Sci.* **2015**, *24* (8), 1176–1192.

(20)   Fernandez de la Mora, J. Electrospray Ionization of Large Mutliply Charged Species Proceeds via Dole's Charged Residue Mechanism. *Anal. Chim. Acta* **2000**, *406* (1), 93–104.

(21)   Heck, A. J. R.; van den Heuvel, R. H. H. Investigation of Intact Protein Complexes by Mass Spectrometry. *Mass Spectrom. Rev.* **2004**, *23* (5), 368–389.

(22)   Kaltashov, I. A.; Mohimen, A. Estimates of Protein Surface Areas in Solution by Electrospray Ionization Mass Spectrometry. *Anal. Chem.* **2005**, *77* (16), 5370–5379.

(23)   Rayleigh, Lord. On the Equilibrium of Conducting Masses Charged with Electricity. *Philos. Mag.* **1882**, *14*, 184–186.

(24)   Wang, G.; Cole, R. B. Effect of Solution Ionic Strength on Analyte Charge State Distributions in Positive and Negative Ion Electrospray Mass Spectrometry. *Anal. Chem.* **1994**, *66* (21), 3702–3708.

(25)   Felitsyn, N.; Peschke, M.; Kebarle, P. Origin and Number of Charges Observed on Multiply-Protonated Native Proteins Produced by ESI. *Int. J. Mass Spectrom.* **2002**, *219* (1), 39–62.

(26)   Verkerk, U. H.; Peschke, M.; Kebarle, P. Effect of Buffer Cations and of H3O+ on the Charge States of Native Proteins. Significance to Determinations of Stability Constants of Protein Complexes. *J. Mass Spectrom.* **2003**, *38* (6), 618–631.

(27)   Catalina, M. I.; van den Heuvel, R. H. H.; van Duijn, E.; Heck, A. J. R. Decharging of Globular Proteins and Protein Complexes in Electrospray. *Chem. - Eur. J.* **2005**, *11* (3), 960–968.

(28)   Lomeli, S. H.; Yin, S.; Ogorzalek Loo, R. R.; Loo, J. A. Increasing Charge While Preserving Noncovalent Protein Complexes for ESI-MS. *J. Am. Soc. Mass Spectrom.* **2009**, *20* (4), 593–596.

(29)   Lomeli, S. H.; Peng, I. X.; Yin, S.; Ogorzalek Loo, R. R.; Loo, J. A. New Reagents for Increasing ESI Multiple Charging of Proteins and Protein Complexes. *J. Am. Soc. Mass Spectrom.* **2010**, *21* (1), 127–131.

(30)   Going, C. C.; Xia, Z.; Williams, E. R. New Supercharging Reagents Produce Highly Charged Protein Ions in Native Mass Spectrometry. *Analyst* **2015**, *140* (21), 7184–7194.

(31)   Hogan, C. J.; Carroll, J. A.; Rohrs, H. W.; Biswas, P.; Gross, M. L. Combined Charged Residue-Field Emission Model of Macromolecular Electrospray Ionization. *Anal. Chem.* **2009**, *81* (1), 369–377.

(32)   Loo, R. R. O.; Lakshmanan, R.; Loo, J. A. What Protein Charging (and Supercharging) Reveal about the Mechanism of Electrospray Ionization. *J. Am. Soc. Mass Spectrom.* **2014**, *25* (10), 1675–1693.

(33)   Susa, A. C.; Xia, Z.; Tang, H. Y. H.; Tainer, J. A.; Williams, E. R. Charging of Proteins in Native Mass Spectrometry. *J. Am. Soc. Mass Spectrom.* **2017**, *28* (2), 332–340.

(34)   McAllister, R. G.; Metwally, H.; Sun, Y.; Konermann, L. Release of Native-like Gaseous Proteins from Electrospray Droplets via the Charged Residue Mechanism: Insights from Molecular Dynamics Simulations. *J. Am. Chem. Soc.* **2015**, *137* (39), 12667–12676.

(35)   Mason, E. A.; McDaniel, E. W. *Transport Properties of Ions in Gases*, pg. 151.; Wiley: New York, 1988.

(36)   Mason, E. A.; McDaniel, E. W. *Transport Properties of Ions in Gases*, pg. 276.; Wiley: New York, 1988.

(37) Wyttenbach, T.; Bleiholder, C.; Bowers, M. T. Factors Contributing to the Collision Cross Section of Polyatomic Ions in the Kilodalton to Gigadalton Range: Application to Ion Mobility Measurements. *Anal. Chem.* **2013**, *85* (4), 2191–2199.

(38) Bleiholder, C.; Johnson, N. R.; Contreras, S.; Wyttenbach, T.; Bowers, M. T. Molecular Structures and Ion Mobility Cross Sections: Analysis of the Effects of He and N2 Buffer Gas. *Anal. Chem.* **2015**, *87* (14), 7196–7203.

(39) Revercomb, H. E.; Mason, E. A. Theory of Plasma Chromatography/Gaseous Electrophoresis. Review. *Anal. Chem.* **1975**, *47* (7), 970–983.

(40) Kanu, A. B.; Gribb, M. M.; Hill, H. H. Predicting Optimal Resolving Power for Ambient Pressure Ion Mobility Spectrometry. *Anal. Chem.* **2008**, *80* (17), 6610–6619.

(41) Wadhwa, C. L. *High Voltage Engineering*, pg. 10-14.; New Age International, 2007.

(42) Kemper, P. R.; Dupuis, N. F.; Bowers, M. T. A New, Higher Resolution, Ion Mobility Mass Spectrometer. *Int. J. Mass Spectrom.* **2009**, *287* (1–3), 46–57.

(43) Douglas, D. J.; French, J. B. Collisional Focusing Effects in Radio Frequency Quadrupoles. *J. Am. Soc. Mass Spectrom.* **1992**, *3* (4), 398–408.

(44) Covey, T.; Douglas, D. J. Collision Cross Sections for Protein Ions. *J. Am. Soc. Mass Spectrom.* **1993**, *4* (8), 616–623.

(45) Cox, K. A.; Julian Jr., R. K.; Cooks, R. G.; Kaiser Jr., R. E. Conformer Selection of Protein Ions by Ion Mobility in a Triple Quadrupole Mass Spectrometer. *J. Am. Soc. Mass Spectrom.* **1994**, *5* (3), 127–136.

(46) Ogorzalek Loo, R. R.; Winger, B. E.; Smith, R. D. Proton Transfer Reaction Studies of Multiply Charged Proteins in a High Mass-to-Charge Ratio Quadrupole Mass Spectrometer. *J. Am. Soc. Mass Spectrom.* **1994**, *5* (12), 1064–1071.

(47) Schnier, P. D.; Gross, D. S.; Williams, E. R. On the Maximum Charge State and Proton Transfer Reactivity of Peptide and Protein Ions Formed by Electrospray Ionization. *J. Am. Soc. Mass Spectrom.* **1995**, *6* (11), 1086–1097.

(48) Clemmer, D. E.; Hudgins, R. R.; Jarrold, M. F. Naked Protein Conformations: Cytochrome c in the Gas Phase. *J. Am. Chem. Soc.* **1995**, *117* (40), 10141–10142.

(49) Shelimov, K. B.; Jarrold, M. F. Conformations, Unfolding, and Refolding of Apomyoglobin in Vacuum: An Activation Barrier for Gas-Phase Protein Folding. *J. Am. Chem. Soc.* **1997**, *119* (13), 2987–2994.

(50) Shelimov, K. B.; Clemmer, D. E.; Hudgins, R. R.; Jarrold, M. F. Protein Structure in Vacuo: Gas-Phase Conformations of BPTI and Cytochrome c. *J. Am. Chem. Soc.* **1997**, *119* (9), 2240–2248.

(51) Valentine, S. J.; Anderson, J. G.; Ellington, A. D.; Clemmer, D. E. Disulfide-Intact and-Reduced Lysozyme in the Gas Phase: Conformations and Pathways of Folding and Unfolding. *J. Phys. Chem. B* **1997**, *101* (19), 3891–3900.

(52) Pringle, S. D.; Giles, K.; Wildgoose, J. L.; Williams, J. P.; Slade, S. E.; Thalassinos, K.; Bateman, R. H.; Bowers, M. T.; Scrivens, J. H. An Investigation of the Mobility Separation of Some Peptide and Protein Ions Using a New Hybrid Quadrupole/Travelling Wave IMS/Oa-ToF Instrument. *Int. J. Mass Spectrom.* **2007**, *261* (1), 1–12.

(53) Ruotolo, B. T.; Giles, K.; Campuzano, I.; Sandercock, A. M.; Bateman, R. H.; Robinson, C. V. Evidence for Macromolecular Protein Rings in the Absence of Bulk Water. *Science* **2005**, *310* (5754), 1658–1661.

(54) McAfee, K. B.; Sipler, D.; Edelson, D. Mobilities and Reactions of Ions in Argon. *Phys. Rev.* **1967**, *160* (1), 130–135.

(55) Guilhaus, M.; Selby, D.; Mlynski, V. Orthogonal Acceleration Time-of-Flight Mass Spectrometry. *Mass Spectrom. Rev.* **2000**, *19* (2), 65–107.

(56) Hill, H. H.; Siems, W. F.; Louis, R. H. S.; McMinn, D. G. ION MOBILITY SPECTROMETRY. *Anal. Chem.* **1990**, *62* (23), 1201A–1209A.

(57) Clemmer, D. E.; Jarrold, M. F. Ion Mobility Measurements and Their Applications to Clusters and Biomolecules. *J. Mass Spectrom.* **1997**, *32* (6), 577–592.

(58) Wyttenbach, T.; Bowers, M. T. Gas-Phase Conformations: The Ion Mobility/Ion Chromatography Method. In *Modern Mass Spectrometry*; Schalley, D. C. A., Ed.; Topics in Current Chemistry; Springer Berlin Heidelberg, 2003; pp 207–232.

(59) May, J. C.; McLean, J. A. Ion Mobility-Mass Spectrometry: Time-Dispersive Instrumentation. *Anal. Chem.* **2015**, *87* (3), 1422–1436.

(60) Tang, K.; Shvartsburg, A. A.; Lee, H.-N.; Prior, D. C.; Buschbach, M. A.; Li, F.; Tolmachev, A. V.; Anderson, G. A.; Smith, R. D. High-Sensitivity Ion Mobility Spectrometry/Mass Spectrometry Using Electrodynamic Ion Funnel Interfaces. *Anal. Chem.* **2005**, *77* (10), 3330–3339.

(61) Baker, E. S.; Clowers, B. H.; Li, F.; Tang, K.; Tolmachev, A. V.; Prior, D. C.; Belov, M. E.; Smith, R. D. Ion Mobility Spectrometry–Mass Spectrometry Performance Using Electrodynamic Ion Funnels and Elevated Drift Gas Pressures. *J. Am. Soc. Mass Spectrom.* **2007**, *18* (7), 1176–1187.

(62) McCullough, B. J.; Kalapothakis, J.; Eastwood, H.; Kemper, P.; MacMillan, D.; Taylor, K.; Dorin, J.; Barran, P. E. Development of an Ion Mobility Quadrupole Time of Flight Mass Spectrometer. *Anal. Chem.* **2008**, *80* (16), 6336–6344.

(63) May, J. C.; Goodwin, C. R.; Lareau, N. M.; Leaptrot, K. L.; Morris, C. B.; Kurulugama, R. T.; Mordehai, A.; Klein, C.; Barry, W.; Darland, E.; et al. Conformational Ordering of Biomolecules in the Gas Phase: Nitrogen Collision Cross Sections Measured on a Prototype High Resolution Drift Tube Ion Mobility-Mass Spectrometer. *Anal. Chem.* **2014**, *86* (4), 2107–2116.

(64) Ibrahim, Y. M.; Baker, E. S.; Danielson III, W. F.; Norheim, R. V.; Prior, D. C.; Anderson, G. A.; Belov, M. E.; Smith, R. D. Development of a New Ion Mobility Time-of-Flight Mass Spectrometer. *Int. J. Mass Spectrom.* **2015**, *377*, 655–662.

(65) Kurulugama, R. T.; Darland, E.; Kuhlmann, F.; Stafford, G.; Fjeldsted, J. Evaluation of Drift Gas Selection in Complex Sample Analyses Using a High Performance Drift Tube Ion Mobility-QTOF Mass Spectrometer. *Analyst* **2015**, *140* (20), 6834–6844.

(66) Dugourd, P.; Hudgins, R. R.; Clemmer, D. E.; Jarrold, M. F. High-Resolution Ion Mobility Measurements. *Rev. Sci. Instrum.* **1997**, *68* (2), 1122–1129.

(67) Guevremont, R.; Siu, K. W. M.; Wang, J.; Ding, L. Combined Ion Mobility/Time-of-Flight Mass Spectrometry Study of Electrospray-Generated Ions. *Anal. Chem.* **1997**, *69* (19), 3959–3965.

(68) Gillig, K. J.; Ruotolo, B.; Stone, E. G.; Russell, D. H.; Fuhrer, K.; Gonin, M.; Schultz, A. J. Coupling High-Pressure MALDI with Ion Mobility/Orthogonal Time-of-Flight Mass Spectrometry. *Anal. Chem.* **2000**, *72* (17), 3965–3971.

(69) Kim, T.; Tolmachev, A. V.; Harkewicz, R.; Prior, D. C.; Anderson, G.; Udseth, H. R.; Smith, R. D.; Bailey, T. H.; Rakov, S.; Futrell, J. H. Design and Implementation of a New Electrodynamic Ion Funnel. *Anal. Chem.* **2000**, *72* (10), 2247–2255.

(70) Lynn, E. C.; Chung, M. C.; Han, C. C. Characterizing the Transmission Properties of an Ion Funnel. *Rapid Commun. Mass Spectrom. RCM* **2000**, *14* (22), 2129–2134.

(71)   Gerlich, D. *In State Selected and State-to State Ion–Molecule Reaction Dynamics. Part 1. Experiment*; Wiley: New York, 1992; Vol. LXXXII.

(72)   Clowers, B. H.; Ibrahim, Y. M.; Prior, D. C.; Danielson, W. F.; Belov, M. E.; Smith, R. D. Enhanced Ion Utilization Efficiency Using an Electrodynamic Ion Funnel Trap as an Injection Mechanism for Ion Mobility Spectrometry. *Anal. Chem.* **2008**, *80* (3), 612–623.

(73)   Koeniger, S. L.; Merenbloom, S. I.; Valentine, S. J.; Jarrold, M. F.; Udseth, H. R.; Smith, R. D.; Clemmer, D. E. An IMS−IMS Analogue of MS−MS. *Anal. Chem.* **2006**, *78* (12), 4161–4174.

(74)   Merenbloom, S. I.; Koeniger, S. L.; Valentine, S. J.; Plasencia, M. D.; Clemmer, D. E. IMS−IMS and IMS−IMS−IMS/MS for Separating Peptide and Protein Fragment Ions. *Anal. Chem.* **2006**, *78* (8), 2802–2809.

(75)   Merenbloom, S. I.; Glaskin, R. S.; Henson, Z. B.; Clemmer, D. E. High-Resolution Ion Cyclotron Mobility Spectrometry. *Anal. Chem.* **2009**, *81* (4), 1482–1487.

(76)   Glaskin, R. S.; Valentine, S. J.; Clemmer, D. E. A Scanning Frequency Mode for Ion Cyclotron Mobility Spectrometry. *Anal. Chem.* **2010**, *82* (19), 8266–8271.

(77)   Glaskin, R. S.; Ewing, M. A.; Clemmer, D. E. Ion Trapping for Ion Mobility Spectrometry Measurements in a Cyclical Drift Tube. *Anal. Chem.* **2013**, *85* (15), 7003–7008.

(78)   Giles, K.; Pringle, S. D.; Worthington, K. R.; Little, D.; Wildgoose, J. L.; Bateman, R. H. Applications of a Travelling Wave-Based Radio-Frequency-Only Stacked Ring Ion Guide. *Rapid Commun. Mass Spectrom.* **2004**, *18* (20), 2401–2414.

(79)   Giles, K.; Williams, J. P.; Campuzano, I. Enhancements in Travelling Wave Ion Mobility Resolution. *Rapid Commun. Mass Spectrom.* **2011**, *25* (11), 1559–1566.

(80)   Zhong, Y.; Hyung, S.-J.; Ruotolo, B. T. Characterizing the Resolution and Accuracy of a Second-Generation Traveling-Wave Ion Mobility Separator for Biomolecular Ions. *Analyst* **2011**, *136* (17), 3534–3541.

(81)   Ridenour, W. B.; Kliman, M.; McLean, J. A.; Caprioli, R. M. Structural Characterization of Phospholipids and Peptides Directly from Tissue Sections by MALDI Traveling-Wave Ion Mobility-Mass Spectrometry. *Anal. Chem.* **2010**, *82* (5), 1881–1889.

(82)   Thalassinos, K.; Grabenauer, M.; Slade, S. E.; Hilton, G. R.; Bowers, M. T.; Scrivens, J. H. Characterization of Phosphorylated Peptides Using Traveling Wave-Based and Drift Cell Ion Mobility Mass Spectrometry. *Anal. Chem.* **2009**, *81* (1), 248–254.

(83)   Lietz, C. B.; Yu, Q.; Li, L. Large-Scale Collision Cross-Section Profiling on a Traveling Wave Ion Mobility Mass Spectrometer. *J. Am. Soc. Mass Spectrom.* **2014**, *25* (12), 2009–2019.

(84)   Scarff, C. A.; Thalassinos, K.; Hilton, G. R.; Scrivens, J. H. Travelling Wave Ion Mobility Mass Spectrometry Studies of Protein Structure: Biological Significance and Comparison with X-Ray Crystallography and Nuclear Magnetic Resonance Spectroscopy Measurements. *Rapid Commun. Mass Spectrom.* **2008**, *22* (20), 3297–3304.

(85)   Hilton, G. R.; Thalassinos, K.; Grabenauer, M.; Sanghera, N.; Slade, S. E.; Wyttenbach, T.; Robinson, P. J.; Pinheiro, T. J. T.; Bowers, M. T.; Scrivens, J. H. Structural Analysis of Prion Proteins by Means of Drift Cell and Traveling Wave Ion Mobility Mass Spectrometry. *J. Am. Soc. Mass Spectrom.* **2010**, *21* (5), 845–854.

(86)   Salbo, R.; Bush, M. F.; Naver, H.; Campuzano, I.; Robinson, C. V.; Pettersson, I.; Jørgensen, T. J. D.; Haselmann, K. F. Travelling Wave Ion Mobility Mass Spectrometry: Calibrants and Instrumental Conditions Are Crucial for Correct Collision Cross-Section Measurements. *Rapid Commun. Mass Spectrom.* **2012**, *26*, 1181–1193.

(87) Zhou, M.; Politis, A.; Davies, R. B.; Liko, I.; Wu, K.-J.; Stewart, A. G.; Stock, D.; Robinson, C. V. Ion Mobility–mass Spectrometry of a Rotary ATPase Reveals ATP-Induced Reduction in Conformational Flexibility. *Nat. Chem.* **2014**, *6* (3), 208–215.

(88) Ruotolo, B. T.; Benesch, J. L. P.; Sandercock, A. M.; Hyung, S.-J.; Robinson, C. V. Ion Mobility–mass Spectrometry Analysis of Large Protein Complexes. *Nat. Protoc.* **2008**, *3* (7), 1139–1152.

(89) Bush, M. F.; Hall, Z.; Giles, K.; Hoyes, J.; Robinson, C. V.; Ruotolo, B. T. Collision Cross Sections of Proteins and Their Complexes: A Calibration Framework and Database for Gas-Phase Structural Biology. *Anal Chem* **2010**, *82*, 9557–9565.

(90) Javahery, G.; Thomson, B. A Segmented Radiofrequency-Only Quadrupole Collision Cell for Measurements of Ion Collision Cross Section on a Triple Quadrupole Mass Spectrometer. *J. Am. Soc. Mass Spectrom.* **1997**, *8* (7), 697–702.

(91) Soulimenkov, I. V.; Kozlovski, V. I.; Pikhtelev, A. R.; Raznikov, V. V.; Chardakova, E. V.; Dodonov, A. F. A New Method to Study the Kinetics of Ion Decay in a Radio Frequency Quadrupole with Resonance Rotational Excitation. *Eur. J. Mass Spectrom.* **2002**, *8* (2), 99–105.

(92) Guo, Y.; Wang, J.; Javahery, G.; Thomson, B. A.; Siu, K. W. M. Ion Mobility Spectrometer with Radial Collisional Focusing. *Anal. Chem.* **2005**, *77* (1), 266–275.

(93) Chudinov, A. V.; Martynovich, Y. G.; Sulimenkov, I. V.; Brusov, V. S.; Filatov, V. V.; Pikhtelev, A. R.; Kozlovskiy, V. I. Study of the Dependence of Peptide Collision Cross Section on the Ion Bunch Drift Velocity in Nitrogen. *J. Anal. Chem.* **2015**, *70* (14), 1647–1653.

(94) Gill, A. C.; Jennings, K. R.; Wyttenbach, T.; Bowers, M. T. Conformations of Biopolymers in the Gas Phase: A New Mass Spectrometric Method. *Int. J. Mass Spectrom.* **2000**, *195–196*, 685–697.

(95) Thalassinos, K.; Slade, S. E.; Jennings, K. R.; Scrivens, J. H.; Giles, K.; Wildgoose, J.; Hoyes, J.; Bateman, R. H.; Bowers, M. T. Ion Mobility Mass Spectrometry of Proteins in a Modified Commercial Mass Spectrometer. *Int. J. Mass Spectrom.* **2004**, *236* (1–3), 55–63.

(96) Silveira, J. A.; Ridgeway, M. E.; Park, M. A. High Resolution Trapped Ion Mobility Spectrometery of Peptides. *Anal. Chem.* **2014**, *86* (12), 5624–5627.

(97) Zucker, S. M.; Ewing, M. A.; Clemmer, D. E. Gridless Overtone Mobility Spectrometry. *Anal. Chem.* **2013**, *85* (21), 10174–10179.

(98) Tolmachev, A. V.; Webb, I. K.; Ibrahim, Y. M.; Garimella, S. V. B.; Zhang, X.; Anderson, G. A.; Smith, R. D. Characterization of Ion Dynamics in Structures for Lossless Ion Manipulations. *Anal. Chem.* **2014**, *86* (18), 9162–9168.

(99) Webb, I. K.; Garimella, S. V. B.; Tolmachev, A. V.; Chen, T.-C.; Zhang, X.; Norheim, R. V.; Prost, S. A.; LaMarche, B.; Anderson, G. A.; Ibrahim, Y. M.; et al. Experimental Evaluation and Optimization of Structures for Lossless Ion Manipulations for Ion Mobility Spectrometry with Time-of-Flight Mass Spectrometry. *Anal. Chem.* **2014**, *86* (18), 9169–9176.

(100) Garimella, S. V. B.; Ibrahim, Y. M.; Webb, I. K.; Tolmachev, A. V.; Zhang, X.; Prost, S. A.; Anderson, G. A.; Smith, R. D. Simulation of Electric Potentials and Ion Motion in Planar Electrode Structures for Lossless Ion Manipulations (SLIM). *J. Am. Soc. Mass Spectrom.* **2014**, *25* (11), 1890–1896.

(101) Webb, I. K.; Garimella, S. V. B.; Tolmachev, A. V.; Chen, T.-C.; Zhang, X.; Cox, J. T.; Norheim, R. V.; Prost, S. A.; LaMarche, B.; Anderson, G. A.; et al. Mobility-Resolved Ion Selection in Uniform Drift Field Ion Mobility Spectrometry/Mass Spectrometry: Dynamic Switching in Structures for Lossless Ion Manipulations. *Anal. Chem.* **2014**, *86* (19), 9632–9637.

(102) Garimella, S. V. B.; Ibrahim, Y. M.; Webb, I. K.; Ipsen, A. B.; Chen, T.-C.; Tolmachev, A. V.; Baker, E. S.; Anderson, G. A.; Smith, R. D. Ion Manipulations in Structures for Lossless Ion Manipulations (SLIM): Computational Evaluation of a 90° Turn and a Switch. *Analyst* **2015**, *140* (20), 6845–6852.

(103) Zhang, X.; Garimella, S. V. B.; Prost, S. A.; Webb, I. K.; Chen, T.-C.; Tang, K.; Tolmachev, A. V.; Norheim, R. V.; Baker, E. S.; Anderson, G. A.; et al. Ion Trapping, Storage, and Ejection in Structures for Lossless Ion Manipulations. *Anal. Chem.* **2015**, *87* (12), 6010–6016.

(104) Chen, T.-C.; Ibrahim, Y. M.; Webb, I. K.; Garimella, S. V. B.; Zhang, X.; Hamid, A. M.; Deng, L.; Karnesky, W. E.; Prost, S. A.; Sandoval, J. A.; et al. Mobility-Selected Ion Trapping and Enrichment Using Structures for Lossless Ion Manipulations. *Anal. Chem.* **2016**, *88* (3), 1728–1733.

(105) Hamid, A. M.; Ibrahim, Y. M.; Garimella, S. V. B.; Webb, I. K.; Deng, L.; Chen, T.-C.; Anderson, G. A.; Prost, S. A.; Norheim, R. V.; Tolmachev, A. V.; et al. Characterization of Traveling Wave Ion Mobility Separations in Structures for Lossless Ion Manipulations. *Anal. Chem.* **2015**, *87* (22), 11301–11308.

(106) Deng, L.; Ibrahim, Y. M.; Baker, E. S.; Aly, N. A.; Hamid, A. M.; Zhang, X.; Zheng, X.; Garimella, S. V. B.; Webb, I. K.; Prost, S. A.; et al. Ion Mobility Separations of Isomers Based upon Long Path Length Structures for Lossless Ion Manipulations Combined with Mass Spectrometry. *ChemistrySelect* **2016**, *1* (10), 2396–2399.

(107) Deng, L.; Ibrahim, Y. M.; Garimella, S. V. B.; Webb, I. K.; Hamid, A. M.; Norheim, R. V.; Prost, S. A.; Sandoval, J. A.; Baker, E. S.; Smith, R. D. Greatly Increasing Trapped Ion Populations for Mobility Separations Using Traveling Waves in Structures for Lossless Ion Manipulations. *Anal. Chem.* **2016**, *88* (20), 10143–10150.

(108) Deng, L.; Ibrahim, Y. M.; Hamid, A. M.; Garimella, S. V. B.; Webb, I. K.; Zheng, X.; Prost, S. A.; Sandoval, J. A.; Norheim, R. V.; Anderson, G. A.; et al. Ultra-High Resolution Ion Mobility Separations Utilizing Traveling Waves in a 13 M Serpentine Path Length Structures for Lossless Ion Manipulations Module. *Anal. Chem.* **2016**, *88* (18), 8957–8964.

(109) Webb, I. K.; Garimella, S. V. B.; Norheim, R. V.; Baker, E. S.; Ibrahim, Y. M.; Smith, R. D. A Structures for Lossless Ion Manipulations (SLIM) Module for Collision Induced Dissociation. *J. Am. Soc. Mass Spectrom.* **2016**, *27* (7), 1285–1288.

(110) Ibrahim, Y. M.; Hamid, A. M.; Cox, J. T.; Garimella, S. V. B.; Smith, R. D. Ion Elevators and Escalators in Multilevel Structures for Lossless Ion Manipulations. *Anal. Chem.* **2017**.

(111) Zhou, M.; Morgner, N.; Barrera, N. P.; Politis, A.; Isaacson, S. C.; Matak-Vinkovic, D.; Murata, T.; Bernal, R. A.; Stock, D.; Robinson, C. V. Mass Spectrometry of Intact V-Type ATPases Reveals Bound Lipids and the Effects of Nucleotide Binding. *Science* **2011**, *334* (6054), 380–385.

(112) Laganowsky, A.; Reading, E.; Allison, T. M.; Ulmschneider, M. B.; Degiacomi, M. T.; Baldwin, A. J.; Robinson, C. V. Membrane Proteins Bind Lipids Selectively to Modulate Their Structure and Function. *Nature* **2014**, *510* (7503), 172–175.

(113) Pagel, K.; Natan, E.; Hall, Z.; Fersht, A. R.; Robinson, C. V. Intrinsically Disordered p53 and Its Complexes Populate Compact Conformations in the Gas Phase. *Angew. Chem. Int. Ed.* **2013**, *52* (1), 361–365.

(114) Jurneczko, E.; Cruickshank, F.; Porrini, M.; Nikolova, P.; Campuzano, I. D. G.; Morris, M.; Barran, P. E. Intrinsic Disorder in Proteins: A Challenge for (Un)structural Biology Met by Ion Mobility–mass Spectrometry. *Biochem. Soc. Trans.* **2012**, *40* (5), 1021–1026.

(115) Jurneczko, E.; Cruickshank, F.; Porrini, M.; Clarke, D. J.; Campuzano, I. D. G.; Morris, M.; Nikolova, P. V.; Barran, P. E. Probing the Conformational Diversity of Cancer-Associated Mutations in p53 with Ion-Mobility Mass Spectrometry. *Angew. Chem. Int. Ed.* **2013**, *52* (16), 4370–4374.

(116) Uetrecht, C.; Barbu, I. M.; Shoemaker, G. K.; van Duijn, E.; Heck, A. J. R. Interrogating Viral Capsid Assembly with Ion Mobility–mass Spectrometry. *Nat. Chem.* **2011**, *3* (2), 126–132.

(117) Bereszczak, J. Z.; Barbu, I. M.; Tan, M.; Xia, M.; Jiang, X.; van Duijn, E.; Heck, A. J. R. Structure, Stability and Dynamics of Norovirus P Domain Derived Protein Complexes Studied by Native Mass Spectrometry. *J. Struct. Biol.* **2012**, *177* (2), 273–282.

(118) Bernstein, S. L.; Dupuis, N. F.; Lazo, N. D.; Wyttenbach, T.; Condron, M. M.; Bitan, G.; Teplow, D. B.; Shea, J.-E.; Ruotolo, B. T.; Robinson, C. V.; et al. Amyloid-β Protein Oligomerization and the Importance of Tetramers and Dodecamers in the Aetiology of Alzheimer's Disease. *Nat. Chem.* **2009**, *1* (4), 326–331.

(119) Grabenauer, M.; Bernstein, S. L.; Lee, J. C.; Wyttenbach, T.; Dupuis, N. F.; Gray, H. B.; Winkler, J. R.; Bowers, M. T. Spermine Binding to Parkinson's Protein α-Synuclein and Its Disease-Related A30P and A53T Mutants. *J. Phys. Chem. B* **2008**, *112* (35), 11147–11154.

(120) Breuker, K.; McLafferty, F. W. Stepwise Evolution of Protein Native Structure with Electrospray into the Gas Phase, 10- 12 to 102 S. *Proc. Natl. Acad. Sci.* **2008**, *105* (47), 18145.

(121) Wyttenbach, T.; Bowers, M. T. Structural Stability from Solution to the Gas Phase: Native Solution Structure of Ubiquitin Survives Analysis in a Solvent-Free Ion Mobility–Mass Spectrometry Environment. *J. Phys. Chem. B* **2011**, *115* (42), 12266–12275.

(122) Pierson, N. A.; Chen, L.; Valentine, S. J.; Russell, D. H.; Clemmer, D. E. Number of Solution States of Bradykinin from Ion Mobility and Mass Spectrometry Measurements. *J. Am. Chem. Soc.* **2011**, *133* (35), 13810–13813.

(123) Breuker, K.; Brüschweiler, S.; Tollinger, M. Electrostatic Stabilization of a Native Protein Structure in the Gas Phase. *Angew. Chem. Int. Ed.* **2011**, *50* (4), 873–877.

(124) Shi, L.; Holliday, A. E.; Shi, H.; Zhu, F.; Ewing, M. A.; Russell, D. H.; Clemmer, D. E. Characterizing Intermediates Along the Transition from Polyproline I to Polyproline II Using Ion Mobility Spectrometry-Mass Spectrometry. *J. Am. Chem. Soc.* **2014**, *136* (36), 12702–12711.

(125) Jurneczko, E.; Barran, P. E. How Useful Is Ion Mobility Mass Spectrometry for Structural Biology? The Relationship between Protein Crystal Structures and Their Collision Cross Sections in the Gas Phase. *Analyst* **2011**, *136* (1), 20–28.

(126) Hall, Z.; Politis, A.; Robinson, C. V. Structural Modeling of Heteromeric Protein Complexes from Disassembly Pathways and Ion Mobility-Mass Spectrometry. *Structure* **2012**, *20* (9), 1596–1609.

(127) Ruotolo, B. T.; Hyung, S.-J.; Robinson, P. M.; Giles, K.; Bateman, R. H.; Robinson, C. V. Ion Mobility–Mass Spectrometry Reveals Long-Lived, Unfolded Intermediates in the Dissociation of Protein Complexes. *Angew. Chem. Int. Ed.* **2007**, *46* (42), 8001–8004.

(128) Freeke, J.; Bush, M. F.; Robinson, C. V.; Ruotolo, B. T. Gas-Phase Protein Assemblies: Unfolding Landscapes and Preserving Native-like Structures Using Noncovalent Adducts. *Chem. Phys. Lett.* **2012**, *524*, 1–9.

(129) Hyung, S.-J.; Robinson, C. V.; Ruotolo, B. T. Gas-Phase Unfolding and Disassembly Reveals Stability Differences in Ligand-Bound Multiprotein Complexes. *Chem. Biol.* **2009**, *16* (4), 382–390.

(130) Hall, Z.; Politis, A.; Bush, M. F.; Smith, L. J.; Robinson, C. V. Charge-State Dependent Compaction and Dissociation of Protein Complexes: Insights from Ion Mobility and Molecular Dynamics. *J. Am. Chem. Soc.* **2012**, *134* (7), 3429–3438.

(131) Zhou, M.; Dagan, S.; H. Wysocki, V. Impact of Charge State on Gas-Phase Behaviors of Noncovalent Protein Complexes in Collision Induced Dissociation and Surface Induced Dissociation. *Analyst* **2013**, *138* (5), 1353–1362.

(132) Hall, Z.; Robinson, C. V. Do Charge State Signatures Guarantee Protein Conformations? *J. Am. Soc. Mass Spectrom.* **2012**, *23* (7), 1161–1168.

(133) Hall, Z.; Hernández, H.; Marsh, J. A.; Teichmann, S. A.; Robinson, C. V. The Role of Salt Bridges, Charge Density, and Subunit Flexibility in Determining Disassembly Routes of Protein Complexes. *Structure* **2013**, *21* (8), 1325–1337.

(134) Loo, R. R. O.; Loo, J. A. Salt Bridge Rearrangement (SaBRe) Explains the Dissociation Behavior of Noncovalent Complexes. *J. Am. Soc. Mass Spectrom.* **2016**, *27* (6), 975–990.

(135) Counterman, A. E.; Valentine, S. J.; Srebalus, C. A.; Henderson, S. C.; Hoaglund, C. S.; Clemmer, D. E. High-Order Structure and Dissociation of Gaseous Peptide Aggregates That Are Hidden in Mass Spectra. *J. Am. Soc. Mass Spectrom.* **1998**, *9* (8), 743–759.

(136) Koeniger, S. L.; Merenbloom, S. I.; Clemmer, D. E. Evidence for Many Resolvable Structures within Conformation Types of Electrosprayed Ubiquitin Ions. *J. Phys. Chem. B* **2006**, *110* (13), 7017–7021.

(137) Wang, S. C.; Politis, A.; Di Bartolo, N.; Bavro, V. N.; Tucker, S. J.; Booth, P. J.; Barrera, N. P.; Robinson, C. V. Ion Mobility Mass Spectrometry of Two Tetrameric Membrane Protein Complexes Reveals Compact Structures and Differences in Stability and Packing. *J. Am. Chem. Soc.* **2010**, *132* (44), 15468–15470.

CHAPTER 2

Radio-Frequency (rf) Confinement in Ion Mobility Spectrometry: Apparent Mobilities and Effective Temperatures

This chapter is reproduced with permission from Allen, S. J.; Bush, M. F. "Radio-Frequency (rf) Confinement in Ion Mobility Spectrometry: Apparent Mobilities and Effective Temperatures" *Journal of The American Society for Mass Spectrometry* **2016**. Copyright 2016 American Society for Mass Spectrometry.

2.1 Abstract

Ion mobility is a powerful tool for separating and characterizing the structures of ions. Here, a radio-frequency (RF) confining drift cell is used to evaluate the drift times of ions over a broad range of drift field strengths (E/P, V cm^{-1} Torr^{-1}). The presence of RF potentials radially confines ions and results in excellent ion transmission at low E/P (less than 1 V cm^{-1} Torr^{-1}), thereby reducing the dependence of ion transmission on the applied drift voltage. Non-linear responses between drift time and reciprocal drift voltages are observed for extremely low E/P and high RF amplitudes. Under these conditions, pseudopotential wells generated by the RF potentials dampen the mobility of ions. The effective potential approximation is used to characterize this mobility dampening behavior, which can be mitigated by adjusting RF amplitudes and electrode dimensions. Using SIMION trajectories and statistical arguments, the effective temperatures of ions in an RF-confining drift cell are evaluated. Results for the doubly charged peptide GRGDS suggest that applied RF potentials can result in a subtle increase (2 K)

in effective temperature compared to an electrostatic drift tube. Additionally, simulations of native-like ions of the protein complex avidin suggest that RF potentials have a negligible effect on the effective temperature of these ions. In general, the results of this study suggest that applied RF potentials enable the measurement of drift times at extremely low *E/P* and that these potentials have negligible effects on ion effective temperature.

2.2 Introduction

Ion mobility (IM) is a gas-phase technique that separates ions based on their size, shape, and charge.[1] When used with mass spectrometry (MS), IM-MS enables the simultaneous characterization of structure and composition.[2–5] IM-MS has been used to characterize a broad range of analytes including chemical warfare agents,[6] organic compounds,[7] drugs,[8] peptides,[9,10] carbohydrates,[11] lipids,[12] proteins,[13] and protein complexes.[9,14] Although some recent mobility techniques such as traveling-wave[15] or trapped[16] IM can enable high resolving power separations, electrostatic drift tube IM offers the advantage of direct determination of the mobility of the ion (*K*).[17–19]

Implementations of electrostatic drift tubes typically include a series of stacked rings that are connected to a voltage divider network.[18–22] Direct-current (DC) potentials applied to the voltage divider network establish a constant DC gradient that ions experience as they traverse the drift region. The drift velocity of ions (v_D) depends on the applied electric field (*E*) and *K*:

$$v_D = KE = K\frac{V}{L} \tag{2.1}$$

where *E* is equal to the applied drift voltage (*V*) divided by the length of the drift region (*L*). *K* depends on the charge and shape of the ion. *K* values can be determined from the slopes of drift time (t_D) versus reciprocal *V* plots:

$$t_D = \frac{L^2}{K}\frac{1}{V} \tag{2.2}$$

These experiments can be used to extract structural information by converting the measured K into a collision cross section (Ω) using the Mason-Schamp equation.[23]

As ions traverse an electrostatic drift tube, a steady-state drift velocity is achieved from the force-balance of ion-neutral collisions and the applied electric field (Equation 2.1). During this time, ions also diffuse axially, which limits resolving power,[24] and radially, which can decrease ion transmission.[25] One strategy to correct for radial diffusion is to position electrostatic lenses[17,20,26,27] or an ion funnel[18,19,21,22] after the drift tube to refocus ions. Ion funnels contain a constant DC gradient in addition to alternating RF (electrodynamic) potentials, similar to a stacked-ring ion guide,[28] applied to incrementally decreasing inner diameter (i.d.) electrodes that refocus radially diffuse ions.[29,30] Other implementations of RF confinement in IM devices include segmented-quadrupoles,[31,32] modified triple quadrupole instruments,[33,34] a stacked-ring ion guide with an applied staircase-like DC gradient,[35] traveling-wave IM cells,[15] trapped IM cells,[16] a gridless-overtone mobility cell,[36] Structures for Lossless Ion Manipulations (SLIM),[37] and RF-confining drift cells.[9,38] RF-confining drift cells contain a constant DC gradient, similar to an electrostatic drift tube, and alternating RF potentials applied to all electrodes, similar to a stacked-ring ion guide. RF-confining drift cells enable direct and absolute determination of Ω values.[9,38] Studies have shown that Ω values determined using RF-confining drift cells are similar to those determined using electrostatic drift tubes.[9,19,38,39]

Although the use of RF confinement with drift cells increases ion transmission, non-linear responses between t_D and reciprocal V (Equation 2.2) have been observed. For example, the first implementation of an RF-confining drift cell[9] and a drift tube containing an ion funnel at the end of the drift region[18] both exhibited longer t_D than expected at lower V. Somewhat

analogous results have been observed for periodically-focused drift tubes,[40] which applied a uniform E across a series of ring electrodes that have smaller i.d. and larger thicknesses than those used for traditional electrostatic drift tubes.[41–43] These electrode geometries generate atypical ion drift motion and, consequently, more ion-neutral collisions that result in longer t_D than would be expected for traditional electrostatic drift tubes.

In native IMMS experiments, analysis of ions that have folded, native-like structures is used to evaluate structures and assemblies that reflect those in solution.[5] Activation of ions can lead to gas-phase unfolding that generates structures that have less memory of those in solution.[17,44,45] Assuming elastic ion-neutral collisions, the effective translational temperature (T_{eff}) of ions in an electrostatic drift tube can be calculated from the drift-gas temperature (T_{gas}) and v_D, which depends on the applied E:[46]

$$T_{eff} = T_{gas} + \frac{M}{3k_B} v_D^2 \qquad (2.3)$$

where M is the mass of the neutral gas and k_B is the Boltzmann constant. For example, T_{eff} for potassium ions estimated from measurements as a function of E and Equation 2.3 agree well with T_{eff} estimated from ion-beam scattering measurements.[47] For electrostatic drift tube measurements performed well below the low-field limit,[48] contributions from v_D to T_{eff} will be small.

Ions in electrodynamic IM experiments may experience high instantaneous fields, therefore it is important to consider the effects of dynamic fields on the temperatures of those ions. For example, several studies have considered T_{eff} of ions in traveling-wave IM devices,[49–51] which use a time-dependent DC "wave" and alternating RF potentials applied to all electrodes.[15] Estimates of T_{eff} using Equation 2.3 and applied E values in traveling-wave IM experiments can range from ~500 to 7300 K.[49] Using chemical thermometer ions, T_{eff} of these ions in traveling-

wave IM devices were estimated to be up to 555 K[50] or 449 K.[51] In those examples, it is difficult to decouple the contributions of traveling-wave DC and RF potentials to the T_{eff} of ions.

Here, experimental measurements and ion simulations of an RF-confining drift cell are used to evaluate the effects of RF confinement on the transport properties of gas-phase ions. The advantages of RF-confining drift cells include control over the applied RF amplitude and DC gradient, which enable an evaluation of ion transport properties over a broad range of DC and RF potential environments. Generally, we find that increased RF amplitudes in a 5 mm i.d. RF-confining drift cell result in longer t_D at low drift field strengths (E/P, V cm^{-1} Torr^{-1}, where P is pressure), whereas t_D in a 7 mm i.d. RF-confining drift cell depend weakly on RF amplitude. These mobility dampening effects in a 5 mm i.d. drift cell are a result of pseudopotential wells along the axis of transmission that have a more significant effect at lower E/P. T_{eff} of ions are estimated based on ion trajectory simulations and a new statistical approach that uses the distribution of relative ion-neutral speeds. Results for the doubly charged peptide GRGDS^{2+} suggest that the presence of RF potentials has negligible effects on the T_{eff} of ions in a 7 mm i.d. RF-confining drift cell relative to that device with no RF potentials applied. In contrast, T_{eff} increases slightly (2 K) for those ions in a 5 mm i.d. RF-confining drift cell containing applied RF potentials. T_{eff} values are also estimated for E/P greater than the low-field limit, which show that higher E/P have a far more significant effect on T_{eff} than applied RF potentials. For comparison, T_{eff} were also estimated for the 17+ charge state of the native-like, homotetramer of avidin. In contrast to GRGDS^{2+} results, RF-confining drift cell i.d. and applied RF potentials have no significant effect on the T_{eff} of these ions.

2.3 Methods

GRGDS (490 Da, Waters Corporation 700005089) was diluted to 0.01 mg mL^{-1} in

49.5/49.5/1 water/methanol/acetic acid solutions. The sample solution was electrosprayed in

positive ion mode through borosilicate capillaries (0.78 mm i.d.) that have one end pulled to a tip

of 1 to 3 μm. All measurements were performed using a modified Waters Synapt G2 HDMS in

which the traveling-wave IM cell was replaced with an RF-confining drift cell as described

previously.[38] Briefly, the RF-confining drift cell is 25.2 cm in length and consists of 168 gold-

coated electrodes that are 0.5 mm thick and have center-to-center spacing of 1.5 mm. Two RF-

confining drift cells were used that differ only in the i.d. of the electrodes (5 or 7 mm). Each

electrode is connected to printed circuit boards containing voltage divider networks that establish

a constant DC voltage gradient across the length of the drift cell. Additionally, RF potentials are

applied to every electrode; the waveform applied to each electrode is 180-degrees out of phase

with that applied to the adjacent electrodes. The RF frequency was 2.8 MHz and the peak-to-

peak RF amplitude (V_{PP}) ranged from 15 to 200 V. All drift times were measured in 3.5 Torr

helium gas.

Ion trajectories were simulated using SIMION 8.1 and the HS1 hard-sphere

approximation for elastic ion-neutral collisions.[52] Briefly, the neutral gas has a Maxwell-

Boltzmann distribution of velocities, which is a function of temperature. The probability of ion-

neutral collision is a function of the mean free path, which is predicted using kinetic theory of

gases as a function of pressure, temperature, and Ω. Mean free paths of GRGDS^{2+} and avidin^{17+}

ions were estimated using published Ω values.[38] Unless specified, ion trajectories were modelled

in 3.5 Torr helium gas. To reduce the cost of calculating the potential array during each step of

the simulations, computational models used one-third the length (8.4 cm) and the same range of E/P (V cm^{-1} Torr^{-1}) used experimentally.

2.4 Results and Discussion

Here we use experiments and simulations to investigate the effects of RF confinement in an RF-confining drift cell. Experimental design and implementation of this RF-confining drift cell have been described previously.[38] The RF-confining potentials enable mobility measurements with transmission efficiencies that depend less on applied drift voltage compared to electrostatic drift tubes. For example, Figure 2.1a shows an electrostatic drift tube, with analogous dimensions to the RF-confining drift cell discussed here. Ion trajectory simulations of the peptide GRGDS^{2+} under a low E/P of 0.507 V cm^{-1} Torr^{-1} show that ions are readily lost prior to the end of the drift region due to diffusion in the radial directions. Ion trajectory simulations of GRGDS^{2+} in an RF-confining drift cell under the same E/P show that the RF potentials in the drift region radially confine ions and increase ion transmission (Figure 2.1b). The following sections evaluate the accuracy of Ω determined with t_D acquired using RF confinement at both moderate and extremely low E/P.
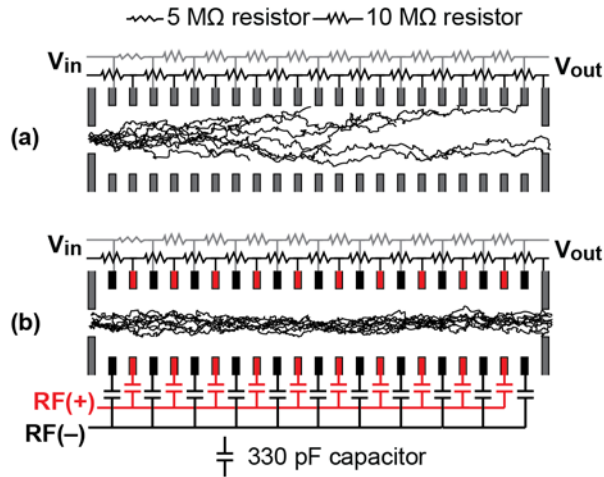
Figure 2.1. (a) Cross sectional view of an electrostatic drift tube consisting of a series of ring electrodes connected to a voltage divider network that establishes a uniform DC gradient ((V_{in} – V_{out}) / drift length) across the axial drift region (x-direction). 10 ion trajectories of GRGDS^{2+} are shown for a low *E/P* of 0.507 V cm^{-1} Torr^{-1}. (b) An RF-confining drift cell with the same physical dimensions and voltage divider network as part a, but that also applies a 2.8 MHz RF waveform to each electrode; the waveform applied to each electrode is 180-degrees out of phase with that for the adjacent electrode. Under the same *E/P* as part a, an RF-confining drift cell exhibits increased ion transmission due to radial confinement. Note, this model is one-eighth of the actual drift cell length. All other ion simulations use a model that is one-third of the length of the actual drift cell.

2.4.1 Effects of VPP on Drift Times, Transmission, and Resolving Power. The effects of varying RF peak-to-peak amplitude (V_{PP}) from 15 to 200 V on the experimental arrival-time distributions of GRGDS^{2+} under a moderate E/P (1.51 V cm^{-1} Torr^{-1}) was evaluated for a 7 mm (Figure 2.2a) and 5 mm (Figure 2.2b) i.d. RF-confining drift cell. Figure 2.2a shows that ion transmission in a 7 mm i.d. cell depends strongly on V_{PP}. In contrast, ion transmission in the 5 mm i.d. cell depends weakly on V_{PP} until $V_{PP} < 25$ V. For a given i.d. cell, the centroids of arrival-time distribution are indistinguishable over the entire V_{PP} range. The resolving powers of the arrival-time distributions in both devices vary randomly within 2.8% of the average over the V_{PP} range investigated.

Figure 2.2c shows the experimental arrival-time distributions for GRGDS^{2+} measured at V_{PP} ranging from 15 to 200 V in a 7 mm i.d. cell under a low E/P of 0.507 V cm^{-1} Torr^{-1}. Although the drift time increases 0.6% with increasing V_{PP}, this example demonstrates that ion drift times can be measured at extremely low E/P. In contrast to the 7 mm i.d. cell, the 5 mm i.d. cell yields arrival-time distributions whose centroids increase up to 3% with V_{PP} from 15 to 200 V (Figure 2.2d). Due to the RF component in the RF-confining drift cell, t_D can be measured at extremely low E/P. Note, the origin of the longer drift times observed in a 5 mm i.d. device (Figure 2.2d) compared to 7 mm i.d. (Figure 2.2c) is discussed in the next section.
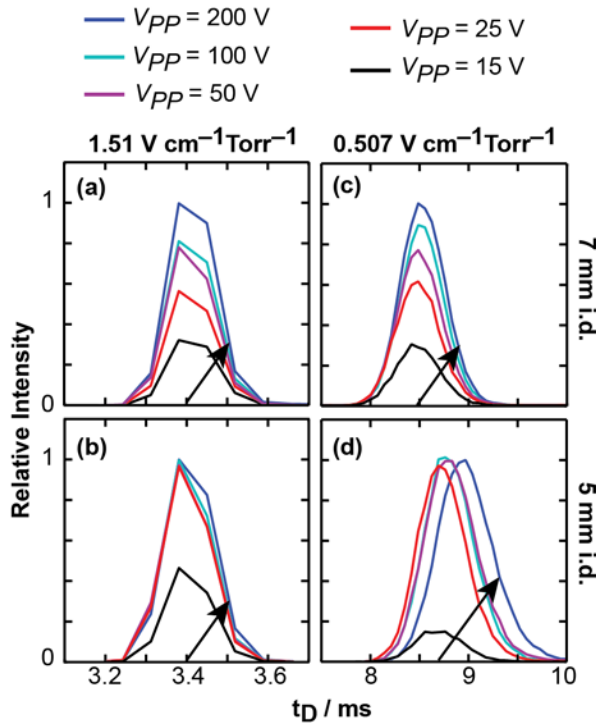
Figure 2.2. Experimental arrival-time distributions of GRGDS^{2+} in 3.5 Torr helium in a (a and c) 7 mm and (b and d) 5 mm i.d. RF-confining drift cell under moderate and low *E/P* of (a and b) 1.51 and (c and d) 0.507 V cm^{-1} Torr^{-1}, respectively. Arrival-time distributions for each *E/P* and i.d. were acquired at five different RF peak-to-peak amplitudes (V_{PP}) ranging from 15 to 200 V. The arrow represents increasing V_{PP} and the intensities are plotted relative to the $V_{PP} = 200$ V peak in each panel. Absolute intensities are not included because data acquired using different i.d. drift cells were acquired on separate days using different electrospray emitters. At high V_{PP} voltages (> 25 V) in the 5 mm i.d. RF-confining drift cell under extremely low *E/P* (part d), arrival-time distributions shift to significantly longer drift times (t_D).

Ion trajectory simulations were used to enable a direct comparison of the transmission, radial distribution, and resolving power of ions in an RF-confining drift cell relative to an electrostatic drift tube of the same dimensions. A discussion on the statistical approaches used in this analysis is described in the Supporting Information. At a drift field strength of 7.00 V cm^{-1} Torr^{-1} and after 8.4 cm in an electrostatic drift tube, 98% of the initial ions survive and have a beam waist of 3.6 mm, which is significantly greater than the diameter of the exit aperture of the drift cell (2.0 mm). For comparison, the diameter of the exit aperture is 2 mm. Ions in an RF-confining drift cell result in 100% transmission over that length and have a beam waist of 1.5 mm. The arrival-time distributions of the ions in the two devices at this field strength (Supporting Information Figure S2.1a) exhibit no significant difference in their average drift times, peak widths, or resolving powers (Supporting Information Table S2.1). At a drift field strength of 1.51 V cm^{-1} Torr^{-1} and after 8.4 cm in an electrostatic drift tube, 21% of the initial ions survive and have a beam waist of 4.0 mm. Ions in an RF-confining drift cell at 1.51 V cm^{-1} Torr^{-1} exhibit 100% transmission and a beam waste of 1.5 mm. Although the average drift time of ions in the RF-confining drift cell is slightly longer than those in the electrostatic drift tube (Supporting Information Figure S2.1b and Table S2.1), there is no significant evidence that the resolving powers in the two devices are different.
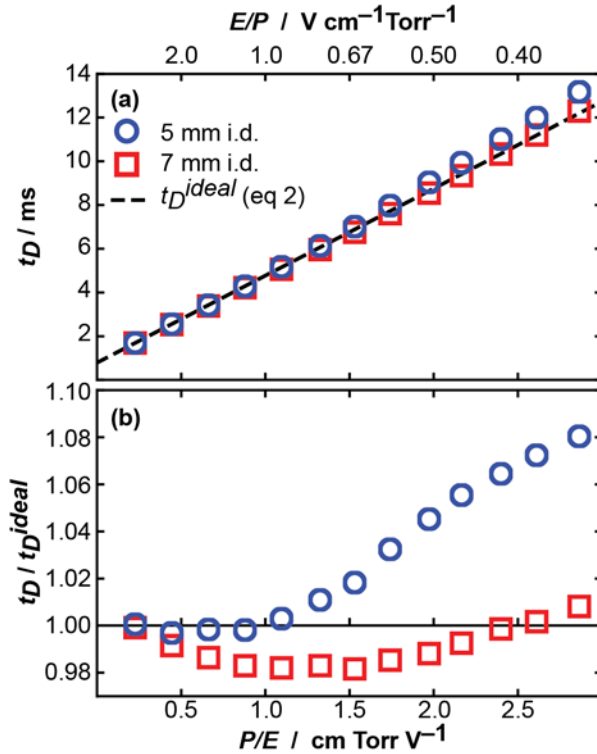
Figure 2.3. Experimental ion mobility data for GRGDS^{2+} versus *P/E* acquired using a 5 mm (*blue circles*) or 7 mm (*red squares*) i.d. RF-confining drift cell with 3.5 Torr helium gas. (a) Drift times (t_D) of GRGDS^{2+} acquired using a 7 mm i.d. cell agree well with ideal drift times (t_D^{ideal}) from Equation 2.2, whereas t_D in the 5 mm i.d. cell are longer than t_D^{ideal}. (b) Plotting t_D relative to t_D^{ideal} over a range of *P/E* show that t_D of GRGDS^{2+} ions in a 5 mm i.d. cell are up to 10% longer than t_D^{ideal}. At extremely low *E/P*, insufficient field strengths at the beginning of the drift region may inhibit the injection of ions, which may contribute to the slight increase in 7 mm i.d. values in panel b.

2.4.2 Effects of E/P on Apparent Mobilities. To evaluate the effects of *E/P* on the apparent mobilities of ions, Figure 2.3a shows experimental t_D of GRGDS^{2+} measured using RF-confining drift cells with $V_{PP} = 200$ V at 3.5 Torr helium. The data in Figure 2.3a are plotted as a

function of P/E (cm Torr V^{-1}), which depends on drift length, pressure, and drift voltages used in these experiments. For a given set of data, pressures and drift cell length are constant, thus, changes in the x-axis depend only on the drift voltage. Figure 2.3b shows that t_D measured using the 7 mm i.d. cell agree well with the drift times calculated using Equation 2.2 (t_D^{ideal}) for all E/P considered. In contrast, at extremely low E/P in the 5 mm i.d. cell, ions exhibit t_D that are up to 10% longer than expected at the lowest E/P (0.35 V cm^{-1} Torr^{-1}). Supporting Information Figure S2.2 shows that these t_D result in significant Ω errors.

Ion trajectory simulations of GRGDS^{2+} in RF-confining drift cells were then used to simulate drift times ($t_D^{sim.}$) over the same range of E/P used in the previous section (Supporting Information Figure S2.3). For each drift voltage, 150 ion trajectories were recorded, from which the averages and standard deviations were calculated. At low E/P, $t_D^{sim.}$ of ions in a 5 mm i.d. cell are longer than t_D^{ideal} expected from Equation 2.2 and $t_D^{sim.}$ of ions in a 7 mm i.d. cell. These simulated results are consistent with the corresponding experimental data (Figure 2.2).

2.4.3 Origin of Mobility Dampening in rf-Confining Drift Cells. To investigate the origin of increased t_D at low E/P, the instantaneous, axial electric field ($E_x^{sim.}$) experienced by GRGDS^{2+} was sampled at 20 MHz, *i.e.*, faster than the 2.8 MHz frequency of the RF waveform. Next, the average $E_x^{sim.}$ was compared to the the applied drift voltage divided by the drift cell length (E_x^{ideal}). Figure 2.4a shows the simulated relative to the ideal electric field ($<E_x^{sim.}>$ / E_x^{ideal}) for GRGDS^{2+} in RF-confining drift cells over a range of E/P. At moderate E/P (1.13 to 4.41 V cm^{-1} Torr^{-1}), the average electric field experienced by the ion in the two devices are indistinguishable. However at extremely low E/P, ions in a 5 mm i.d. cell experience up to 5% less electric field compared to the ideal field, which is attributed to ions spending more time in lower field regions of the drift cell. This results in $t_D^{sim.}$ that are longer than expected.

The effective potential (V_{eff}), or pseudopotential, approximation is an alternative way to describe the electrical environment experienced by an ion that is moving slowly relative to the fast alternating RF potential.[28] Tolmachev et al. evaluated V_{eff} as:[53]

$$V_{eff}(r,z) = \frac{ze(V_{PP})^2}{16m\omega^2\delta^2 I_0^2(\rho/\delta)}[I_1^2(r/\delta)cos^2(z/\delta) + I_0^2(r/\delta)sin^2(z/\delta)] \qquad (2.4)$$

where z is the ion charge, e is the elementary charge, m is ion mass, $\omega = 2\pi f$ where f is the RF frequency, ρ is the inner electrode radius, r is the radial position, z is the axial position, $\delta = d/\pi$ where d is the center-to-center electrode spacing, and I_0 and I_1 are zero- and first-order modified Bessel functions, respectively. Radial focusing in ion funnels[30,53,54] and periodic-focusing DC-ion guides[41,43] have been modelled previously using V_{eff}.

Supporting Information Figure S2.4 shows V_{eff} of GRGDS^{2+} in RF-confining drift cells with $f = 2.8$ MHz and $V_{PP} = 200$ V with no drift voltage. This representation shows the pseudopotential environment that radially confines the trajectory of the ions; as ions diffuse in the radial directions, they experience elevated potentials that confine their trajectory. Closer examination of the V_{eff} surface reveals small pseudopotential wells in a 5 mm i.d. RF-confining drift cell that ions also experience (Figure 2.4b). In other studies using ion funnels, reducing these pseudopotential wells by adjusting electrode dimensions was critical to reducing bias in m/z transmission.[30,53,54]
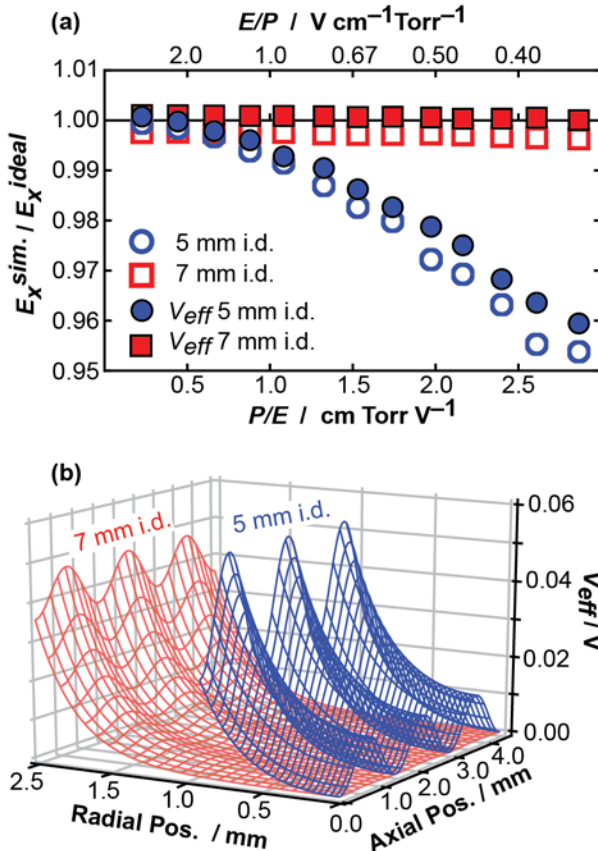
Figure 2.4. (a) The average of the instantaneous electric field ($<E_x^{sim.}>$) experienced by GRGDS^{2+} during simulations of ion trajectories relative to ideal electric field (E_x^{ideal}, defined as the drift voltage divided by the drift cell length) plotted versus *P/E*. The open symbols show data for ions in a 5 mm (*blue circles*) or 7 mm (*red squares*) i.d. RF-confining drift cell. These values are compared to $<E_x^{sim}>$ relative to E_x^{ideal} of GRGDS^{2+} in an effective potential (V_{eff}), which are plotted using closed symbols. Error bars are excluded because they are small compared to the marker size. (b) Zoomed regions (three electrodes) of V_{eff} (Equation 2.4) surfaces for GRGDS^{2+} in a 5 mm (*blue*) or 7 mm (*red*) i.d. cell with no applied drift voltage, $V_{PP} = 200$ V, and $f = 2.8$ MHz. The full surfaces are shown in Supporting Information Figure S2.4.

To interpret the validity of V_{eff} to explain ion motion in a RF-confining drift cell, potential arrays of V_{eff} were constructed by superimposing a constant DC gradient onto Equation 2.4. These potential arrays were imported into SIMION and ion trajectories were simulated to calculate the average $E_x^{sim.}$ compared to E_x^{ideal} (Figure 2.4a, solid data points). Interestingly, the average electric fields experienced by ions using V_{eff} are similar to those in trajectories that explicitly treated the RF potentials. Minor differences between the V_{eff} and RF-confining drift cell data sets (less than 1%) may be due to limitations in this effective potential approximation (Equation 2.4) or the use of a linear DC potential (rather than using a more accurate potential array for the electrostatic contributions).

These data show that in an RF-confining drift cell, pseudopotential wells generated by the RF potentials dampen the mobility of ions and the magnitude of this effect depends on electrode dimensions and E/P. For example, experimental data in Figure 2.2d shows that ions in a 5 mm i.d. device have longer drift times than those in a 7 mm i.d. device (Figure 2.2c) at low E/P. Additionally, this approach validates the use of V_{eff} to provide a robust, facile means of simulating ion trajectories with reduced computational cost. Supporting Information Discussion and Figure S2.5 provide a discussion and visual representation of the radial confinement and mobility dampening behavior of RF-confining drift cells as a function of electrode i.d. and V_{PP}. Briefly, similar radial confinement and mobility dampening effects can be achieved using both i.d. cells by adjusting V_{PP}. However, reducing mobility dampening by decreasing V_{PP} may also decrease ion transmission (Figure 2.2). Another important consideration is the ion beam waist relative to the exit aperture of the drift cell (2 mm i.d.), which can reduce ion transmission for conditions at low V_{PP} or larger i.d. This is consistent with Figures 2.2b and 2.2d, which show that for $V_{PP} > 15$ V in a 5 mm i.d. cell, ion intensity stays constant due to ion beam waists being

narrower than the exit aperture of the drift cell (in contrast to the 7 mm i.d. cell results in Figures 2.2a and 2.2c). Operating at moderate V_{PP} (50 to 100 V) values enables mobility analysis with minimal transmission loss and negligible mobility dampening.

The mobility of an ion can also affect V_{eff}. For example, Tolmachev et al. introduced a pressure correction factor (γ) to Equation 2.4 that depends on the mass of the ion, Ω, pressure, f, and other factors.[55] Supporting Information discussion and Table S2.2 show that for GRGDS^{2+}, γ = 0.984; a value of γ = 1 represents no effect from the mobility on V_{eff}. To evaluate the contributions of mobility on V_{eff} for larger systems with lower mobility than GRGDS^{2+}, γ for the 17+ charge state of the native-like, homotetramer of avidin (64 kDa) was calculated to be 0.999. This suggests that the mobilities of larger, native-like ions will not contribute significantly to the effectiveness of V_{eff}. Instead, the major contribution to V_{eff} of different ions is m/z; according to Equation 2.4, V_{eff} is inversely proportional to m/z. According to this relationship, higher m/z ions will have both reduced mobility dampening and RF-confinement than lower m/z ions.

2.4.4 Effective Temperatures. To gain insights into the effects of RF confinement on the effective temperature (T_{eff}) of ions, ion trajectories of GRGDS^{2+} in 3.5 Torr helium gas at 5.29 V cm^{-1} (1.51 V cm^{-1} Torr^{-1}) were simulated in RF-confining drift cells with V_{PP} = 200 and 0 V (the latter is an electrostatic drift tube). All ion trajectories were simulated using a hard-sphere approximations model for ion-neutral collisions (described in *Methods*). Figure 2.5a (top panel) shows that ions in a 5 mm i.d. cell with V_{PP} = 0 V experience a constant electric field (E_x). In contrast, ions in a 5 mm i.d. cell with V_{PP} = 200 V can briefly experience extremely high instantaneous E_x (up to 177 V cm^{-1}) when between ring electrodes due the alternating RF potentials (Figure 2.5b, top panel). For comparison, GRGDS^{2+} in an electrostatic drift tube with a constant E_x of 177 V cm^{-1} would have a velocity of 3250 m s^{-1}, which would yield a T_{eff} of

~1990 K, based on Equations 2.1 and 2.3, and result in rapid dissociation of peptide ions.[56] The instantaneous drift velocities (v_x) of these ions are shown in Figure 2.5 (middle panels). Although the distribution of v_x is broader in the presence of RF potentials (Figure 2.5b), the peak v_x (585 m s^{-1}, which would correspond to a T_{eff} of 353 K using Equation 2.3) is substantially less than that expected based on the peak E_x. Because the RF waveforms have such a high frequency (2.8 MHz), the ion does not accelerate substantially during a single RF cycle. For the ion trajectories shown in Figure 2.5a and 2.5b, average E_x values (5.29 and 5.26 V cm^{-1}, respectively) and v_x values (104.4 and 100.6 m s^{-1}, respectively) are similar. Using these average v_x values and Equation 2.3, ions in an RF-confining drift cell with $V_{PP} = 0$ or 200 V have T_{eff} values of 299.9 or 299.8 K, respectively.

For a 5 mm i.d. cell, T_{eff} values determined using the peak and average v_x are different. A similar analysis performed for the 7 mm i.d. cell is shown in Supporting Information Figure S2.6, and the resulting T_{eff} values determined using the peak and average v_x are also very different. A summary of all T_{eff} values is shown in Supporting Information Table S2.3. It is challenging to determine whether the peak or average v_x is more appropriate, particularly since Equation 2.3 was derived for ions in an electrostatic drift tube.[46] Instead, an alternative approach was developed that depends on the distribution of relative ion-neutral speeds, rather than v_x.
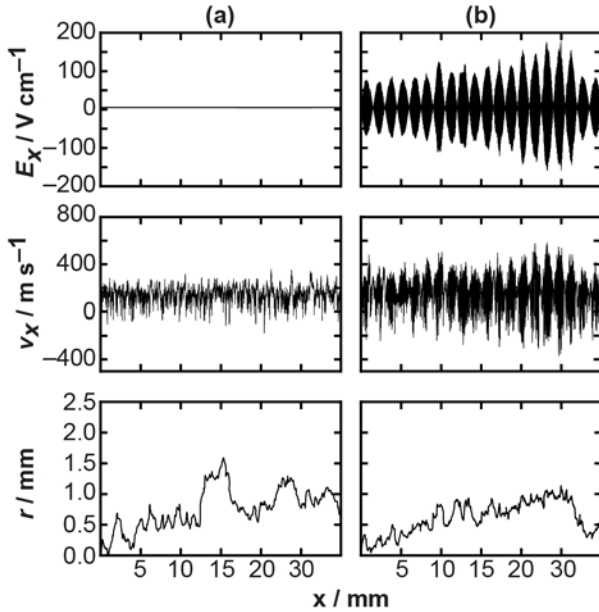
Figure 2.5. Ion trajectory simulations of GRGDS^{2+} in 3.5 Torr helium buffer gas in a 5 mm i.d. RF-confining drift cell with V_{PP} = (a) 0 or (b) 200 V. All values are plotted versus the axial position along the drift cell (x). The *top panels* show the instantaneous electric field experienced by the ion (E_x), the *middle panels* show the instantaneous velocity (v_x), and the *bottom panels* show the radial position of the ion (r). Each plot consists of a single ion trajectory with E_x, v_x, and r values sampled at 20 MHz. The x-axis only spans a small segment of the drift cell to better visualize subtle trends in data.

In order to determine the distribution of relative ion-neutral speeds, populations of ion (v_i, where $i = x$, y, and z) and neutral (V_i) velocities were used. v_i values were sampled from ion trajectory simulations. All ion trajectories were simulated using the hard-sphere approximation collision model (described in *Methods*), during which v_i values were recorded just before an ion-neutral collision. For each E/P, greater than 800,000 v_i values were recorded to generate a large

ensemble for statistical comparisons. Populations of neutral gas velocities (V_i) were sampled

from a Maxwell-Boltzmann distribution at standard ambient temperature ($T = 298.15$ K):

$$f(V_i) = \sqrt{\frac{M}{2\pi k_B T}} 4\pi V_i^2 e^{\frac{-MV_i^2}{2k_B T}} \tag{2.5}$$

where M is the mass of the neutral (4.0 Da for helium). Relative ion-neutral speeds (s) were then

calculated:

$$s = \sqrt{\sum_{i=x,y,z}(v_i - V_i)^2} \tag{2.6}$$

Histograms of the ion-neutral speeds determined using this approach for GRGDS^{2+} at 0 and 4.42

V cm^{-1} Torr^{-1} are shown in Supporting Information Figure S2.7a.

At equilibrium in the absence of an applied E, the relative ion-neutral speed distribution

should be well-described by the Maxwell-Boltzmann distribution of relative speeds:

$$f(s) = \left(\frac{\mu}{2\pi k_B T}\right)^{3/2} 4\pi s^2 e^{\frac{-\mu s^2}{2k_B T}} \tag{2.7}$$

where μ is the ion-neutral reduced mass. As expected, the Maxwell-Boltzmann speed distribution

at 298.15 K and the histogram of speeds obtained in the absence of applied E are

indistinguishable, but the histogram obtained for 4.42 V cm^{-1} Torr^{-1} is shifted towards higher

speeds (Supporting Information Figure S2.7b). The difference between the histogram of speeds

obtained for 4.42 V cm^{-1} Torr^{-1} and the Maxwell-Boltzmann speed distribution was minimized

by optimizing T in Equation 2.7 using a Levenberg−Marquardt, least-squares minimization

algorithm.[57] That process yielded a T of 311 K and the resulting Maxwell-Boltzmann speed

distribution is indistinguishable from the histogram of speeds (Supporting Information Figure

S2.7c). Temperatures determined using this approach will be referred to as T_{eff}^{*} and represent the

effective translational temperature of the ions in these simulations. Note that the structural

dynamics of ions will depend on their internal-energy distributions, which will also depend on

how efficiently energy is converted between translational and internal degrees of freedom. Therefore, the effective translational temperature likely represents the upper limit to the effective internal temperature of the ions.

Figure 2.6a shows T_{eff}^{*} values of GRGDS^{2+} ions in 3.5 Torr helium buffer gas that were calculated from ion trajectory simulations of RF-confining drift cells with $V_{PP} = 0$ V (analogous to an electrostatic drift tube) for a broad range of E. T_{eff}^{*} of GRGDS^{2+} significantly increases at E/P values greater than 2 V cm^{-1} Torr^{-1} due to significantly higher v_i under these conditions. For E/P values lower than 2 V cm^{-1} Torr^{-1}, T_{eff}^{*} is relatively constant at ~299 K. T_{eff}^{*} values determined using the method above for ions when $V_{PP} = 0$ V are indistinguishable from T_{eff} estimated from Equation 2.3 (Figure 2.6a, black line), which validates using this approach to estimate effective temperatures.

Next, the above approach was used to estimate T_{eff}^{*} values for GRGDS^{2+} ions in RF-confining drift cells with $V_{PP} = 200$ V (Figure 2.6a). These values show a similar increase to higher T_{eff}^{*} at E/P values higher than 2 V cm^{-1} Torr^{-1} compared to T_{eff}^{*} values from the $V_{PP} = 0$ V devices. Interestingly, applied RF potentials in a 5 mm i.d. cell results, on average, in a 2 K increase in T_{eff}^{*} for a given E/P value compared to values determined using $V_{PP} = 0$ V. In contrast to the T_{eff} results from Equation 2.3 (Figure 2.6a, black line), T_{eff}^{*} results show that there is a systematic, yet subtle, increase in effective temperature for ions in a 5 mm i.d. RF-confining drift cell with $V_{PP} = 200$ V.
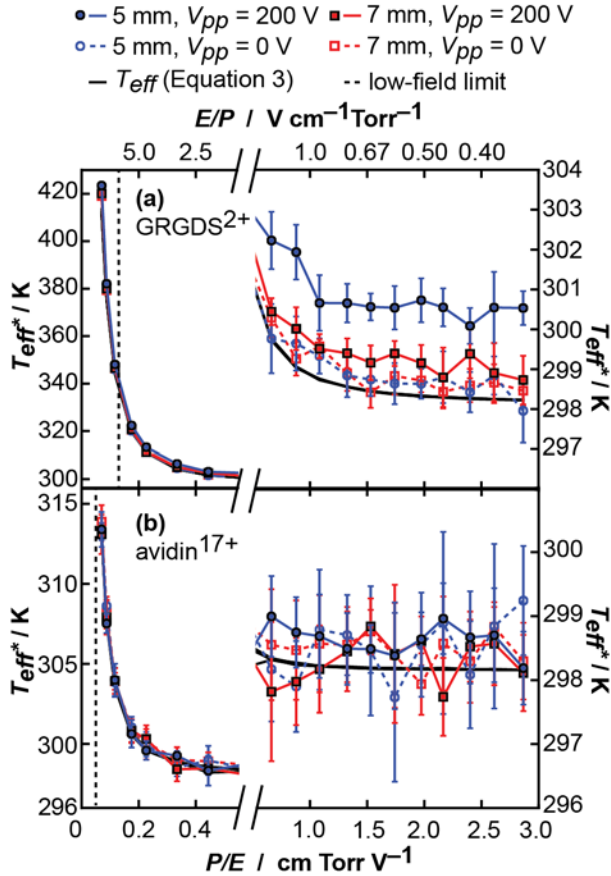
Figure 2.6. Effective temperatures (T_{eff}^*) of (a) GRGDS^{2+} and (b) avidin^{17+} in 3.5 Torr helium buffer gas as a function of *P/E*. The *solid black line* represents T_{eff} values calculated using the average v_x obtained from ion trajectory simulations and Equation 2.3. T_{eff}^* values calculated using least-squares minimization of relative-speed distributions to Maxwell-Boltzmann distributions are shown for ions in a 5 mm i.d. $V_{PP} = 200$ V (*solid blue circles*), 5 mm i.d. $V_{PP} = 0$ V (*open blue circles*), 7 mm i.d. $V_{PP} = 200$ V (*solid red squares*), or 7 mm i.d. $V_{PP} = 0$ V (*open red squares*) cell. (a) T_{eff}^* of GRGDS^{2+} ions significantly increase (up to 420 K) at *E/P* values greater than 2 V cm^{-1} Torr^{-1}. For comparison, the low-field limit[48] (*dashed black line*) of GRGDS^{2+} ions is 7.7 V cm^{-1} Torr^{-1}. Values lower than 2 V cm^{-1} Torr^{-1} show that T_{eff}^* depends weakly on *E/P*. T_{eff}^* for ions

measured in a 5 mm i.d. RF-confining drift cell with $V_{PP} = 200$ V (*solid blue circles*) are systematically higher than those for the other conditions. (b) T_{eff}^{*} values at high *E/P* for avidin[17+] are significantly lower than those found in part a. For comparison, the low-field limit (*dashed black line*) of avidin[17+] ions is 20 V cm^{−1} Torr[−1]. All T_{eff}^{*} values of avidin[17+] are indistinguishable between different i.d. and V_{PP} and similar to values calculated using Equation 2.3. Error bars represent a 95% confidence interval (Supporting Information Figure S2.7).

Figure 2.6b shows T_{eff}^{*} values that were estimated for the 17+ charge state of the native-like, homotetramer of avidin. In contrast to GRGDS[2+] results, T_{eff}^{*} values for avidin[17+] are lower, particularly at the highest *E/P* conditions. Additionally, RF-confining drift cell i.d. and applied RF potential have no effect on the T_{eff}^{*} of these ions. For comparison, T_{eff}^{*} values were calculated using trajectories for GRGDS[2+] and avidin[17+] ions in 2 Torr helium gas to evaluate the effects of pressure (Supporting Information Figure S2.8). T_{eff}^{*} values calculated in 2 or 3.5 Torr helium differ, on average, by less than 0.03%, suggesting that lower pressures do not affect T_{eff}^{*} under these conditions.

In both i.d. RF-confining drift cells and at different helium buffer gas pressures, the application of RF potentials has minimal effect on the T_{eff}^{*} of ions. Instead, T_{eff}^{*} depends predominantly on *E* and the mobility of the analyte. For comparison, typical mobility conditions used in previous 7 mm i.d. RF-confining drift cell studies used *E/P* values of 2 to 7 V cm^{−1} Torr[−1].[38,39] T_{eff}^{*} of GRGDS[2+] at those limits are ~ 304 and 332 K, respectively (Figure 2.6a). Thus, higher *E* in those experiments contribute to higher T_{eff}^{*} values, which may result in structural isomerization. For GRGDS[2+] at *E/P* of 7 V cm^{−1} Torr[−1], indistinguishable resolving

powers were found for ion trajectory simulations using an electrostatic drift tube and an RF confining drift cell (Supporting Information Figure S2.1a). This result suggests that the T_{eff}^* (332 K) and presence of RF-confining potentials do not affect the apparent resolving power under these conditions, which is consistent with the experimental resolving powers of this ions being consistent with the diffusion of a single conformer over a wide range of E/P.[38] Because RF-confining drift cells enable measurements at extremely low E, adjusting drift voltage ranges to lower values enables mobility experiments with negligible contributions from field heating. Analogous analysis for the avidin 17+ data in Figure 2.6b shows that T_{eff}^* values for E/P of 2 to 7 V cm^{-1} Torr^{-1} range from 299 to 303 K, respectively. Because large native-like protein and protein complex ions have lower mobilities than peptide ions, they experience even less field-induced heating at a given E.

2.5 Conclusions

The effects of RF confinement on the mobilities and effective temperatures of ions were evaluated using experimental results and computational models of RF-confining drift cells. For a wide range of E/P and V_{PP} values, the 7 mm i.d. RF-confining drift cell measures t_D that are similar to those expected for an analogous electrostatic drift tube (Figure 2.3a). In contrast, for the lowest E/P used here, the 5 mm i.d. RF-confining drift cell exhibits t_D that are longer than expected. Using the effective potential approximation, ion trajectory simulations showed that mobility dampening occurs due to the presence of pseudopotential wells generated by alternating RF potentials (Figure 2.4b), especially at high V_{PP} values. The effects of these pseudopotential wells on the mobility of ions is exacerbated at extremely low E/P. Mobility dampening in an RF-confining drift cell can be reduced by decreasing V_{PP}, but as a consequence, ion transmission

may decrease. These results provide a fundamental framework for increasing the drift voltage parameter space and maintaining sufficient ion transmission in RF-confining drift cells, while not compromising the accuracy of resulting structural information.

The effective temperatures of ions were evaluated using ion trajectory simulations of the peptide GRGDS^{2+} and protein complex avidin^{17+} (Figure 2.6). Analysis of the relative-speed distribution of the analyte and drift gas shows that the application of RF potentials has minimal effect on effective temperature. Rather, major contributions to effective temperatures are from drift-field induced heating at high E/P. These results assist in evaluating the effects of RF potentials on effective temperatures of ions over a broad range of E/P in RF-confining drift cells. The approach described in this work can be used to evaluate effective temperatures of ions in other IM devices containing RF potentials or other time-dependent electric fields.

This work demonstrates that RF-confining drift cells can operate under conditions, *e.g.*, 7 mm i.d. and V_{PP} less than 200 V, in which Equations 2.1 and 2.2 are valid and Ω determined using RF-confining drift cell measurements are indistinguishable from those determined using an electrostatic drift tube. Benefits of RF-confining drift cells, in which ions are confined radially throughout the entire separation, include that modest i.d. electrodes can be used for devices with long path lengths that can be operated over a wide range of E/P. To maintain transmission for an electrostatic drift tube, the i.d. of electrodes must increase with increasing path length and decreasing E/P in order to ensure that ions are not lost prior to reaching a rear ion funnel Advantages of reduced E/P measurements include reduced drift-field induced heating of the ions and longer drift times that reduce the contributions from other sources of peak broadening, e.g., ion gating. One disadvantage of RF-confining drift cells is that all electrodes are coupled to RF waveforms, which will become more challenging for significantly higher drift voltages due to

dielectric breakdown of capacitors. Ultimately, this work shows that under the appropriate conditions, ion mobility devices may benefit from electrodynamic potentials, while retaining the fundamental ion separation principles used for traditional, electrostatic drift tubes.

2.6 Acknowledgements

2.7 Supporting Information Available

The online version of this article contains supporting information, which is available to authorized users.

2.8 References

(1)   May, J. C.; McLean, J. A. Ion Mobility-Mass Spectrometry: Time-Dispersive Instrumentation. *Anal. Chem.* **2015**, *87* (3), 1422–1436.
(2)   Uetrecht, C.; Barbu, I. M.; Shoemaker, G. K.; van Duijn, E.; Heck, A. J. R. Interrogating Viral Capsid Assembly with Ion Mobility–mass Spectrometry. *Nat. Chem.* **2011**, *3* (2), 126–132.
(3)   Rabuck, J. N.; Hyung, S.-J.; Ko, K. S.; Fox, C. C.; Soellner, M. B.; Ruotolo, B. T. Activation State-Selective Kinase Inhibitor Assay Based on Ion Mobility-Mass Spectrometry. *Anal. Chem.* **2013**, *85* (15), 6995–7002.
(4)   Zhou, M.; Jones, C. M.; Wysocki, V. H. Dissecting the Large Noncovalent Protein Complex GroEL with Surface-Induced Dissociation and Ion Mobility–Mass Spectrometry. *Anal. Chem.* **2013**, *85* (17), 8262–8267.
(5)   Zhou, M.; Politis, A.; Davies, R. B.; Liko, I.; Wu, K.-J.; Stewart, A. G.; Stock, D.; Robinson, C. V. Ion Mobility–mass Spectrometry of a Rotary ATPase Reveals ATP-Induced Reduction in Conformational Flexibility. *Nat. Chem.* **2014**, *6* (3), 208–215.

(6) D'Agostino, P. A.; Chenier, C. L. Desorption Electrospray Ionization Mass Spectrometric Analysis of Organophosphorus Chemical Warfare Agents Using Ion Mobility and Tandem Mass Spectrometry. *Rapid Commun. Mass Spectrom.* **2010**, *24* (11), 1617–1624.

(7) Reynolds, J. C.; Blackburn, G. J.; Guallar-Hoyas, C.; Moll, V. H.; Bocos-Bintintan, V.; Kaur-Atwal, G.; Howdle, M. D.; Harry, E. L.; Brown, L. J.; Creaser, C. S.; et al. Detection of Volatile Organic Compounds in Breath Using Thermal Desorption Electrospray Ionization-Ion Mobility-Mass Spectrometry. *Anal. Chem.* **2010**, *82* (5), 2139–2144.

(8) Campuzano, I.; Bush, M. F.; Robinson, C. V.; Beaumont, C.; Richardson, K.; Kim, H.; Kim, H. I. Structural Characterization of Drug-like Compounds by Ion Mobility Mass Spectrometry: Comparison of Theoretical and Experimentally Derived Nitrogen Collision Cross Sections. *Anal. Chem.* **2012**, *84* (2), 1026–1033.

(9) Bush, M. F.; Hall, Z.; Giles, K.; Hoyes, J.; Robinson, C. V.; Ruotolo, B. T. Collision Cross Sections of Proteins and Their Complexes: A Calibration Framework and Database for Gas-Phase Structural Biology. *Anal. Chem.* **2010**, *82* (22), 9557–9565.

(10) Lietz, C. B.; Yu, Q.; Li, L. Large-Scale Collision Cross-Section Profiling on a Traveling Wave Ion Mobility Mass Spectrometer. *J. Am. Soc. Mass Spectrom.* **2014**, *25* (12), 2009–2019.

(11) Hofmann, J.; Hahm, H. S.; Seeberger, P. H.; Pagel, K. Identification of Carbohydrate Anomers Using Ion Mobility-Mass Spectrometry. *Nature* **2015**, *526* (7572), 241–244.

(12) Groessl, M.; Graf, S.; Knochenmuss, R. High Resolution Ion Mobility-Mass Spectrometry for Separation and Identification of Isomeric Lipids. *Analyst* **2015**, *140* (20), 6904–6911.

(13) Jurneczko, E.; Cruickshank, F.; Porrini, M.; Nikolova, P.; Campuzano, I. D. G.; Morris, M.; Barran, P. E. Intrinsic Disorder in Proteins: A Challenge for (Un)structural Biology Met by Ion Mobility–mass Spectrometry. *Biochem. Soc. Trans.* **2012**, *40* (5), 1021–1026.

(14) Ruotolo, B. T.; Giles, K.; Campuzano, I.; Sandercock, A. M.; Bateman, R. H.; Robinson, C. V. Evidence for Macromolecular Protein Rings in the Absence of Bulk Water. *Science* **2005**, *310* (5754), 1658–1661.

(15) Giles, K.; Williams, J. P.; Campuzano, I. Enhancements in Travelling Wave Ion Mobility Resolution. *Rapid Commun. Mass Spectrom.* **2011**, *25* (11), 1559–1566.

(16) Silveira, J. A.; Ridgeway, M. E.; Park, M. A. High Resolution Trapped Ion Mobility Spectrometery of Peptides. *Anal. Chem.* **2014**, *86* (12), 5624–5627.

(17) Shelimov, K. B.; Clemmer, D. E.; Hudgins, R. R.; Jarrold, M. F. Protein Structure in Vacuo: Gas-Phase Conformations of BPTI and Cytochrome c. *J. Am. Chem. Soc.* **1997**, *119* (9), 2240–2248.

(18) Kemper, P. R.; Dupuis, N. F.; Bowers, M. T. A New, Higher Resolution, Ion Mobility Mass Spectrometer. *Int. J. Mass Spectrom.* **2009**, *287* (1–3), 46–57.

(19) May, J. C.; Goodwin, C. R.; Lareau, N. M.; Leaptrot, K. L.; Morris, C. B.; Kurulugama, R. T.; Mordehai, A.; Klein, C.; Barry, W.; Darland, E.; et al. Conformational Ordering of Biomolecules in the Gas Phase: Nitrogen Collision Cross Sections Measured on a Prototype High Resolution Drift Tube Ion Mobility-Mass Spectrometer. *Anal. Chem.* **2014**, *86* (4), 2107–2116.

(20) Dugourd, P.; Hudgins, R. R.; Clemmer, D. E.; Jarrold, M. F. High-Resolution Ion Mobility Measurements. *Rev. Sci. Instrum.* **1997**, *68* (2), 1122–1129.

(21) Baker, E. S.; Clowers, B. H.; Li, F.; Tang, K.; Tolmachev, A. V.; Prior, D. C.; Belov, M. E.; Smith, R. D. Ion Mobility Spectrometry—mass Spectrometry Performance Using

Electrodynamic Ion Funnels and Elevated Drift Gas Pressures. *J. Am. Soc. Mass Spectrom.* **2007**, *18* (7), 1176–1187.

(22)   Ibrahim, Y. M.; Baker, E. S.; Danielson III, W. F.; Norheim, R. V.; Prior, D. C.; Anderson, G. A.; Belov, M. E.; Smith, R. D. Development of a New Ion Mobility Time-of-Flight Mass Spectrometer. *Int. J. Mass Spectrom.* **2015**, *377*, 655–662.

(23)   Mason, E. A.; McDaniel, E. W. *Transport Properties of Ions in Gases*; Wiley: New York, 1988.

(24)   Revercomb, H. E.; Mason, E. A. Theory of Plasma Chromatography/Gaseous Electrophoresis. Review. *Anal. Chem.* **1975**, *47* (7), 970–983.

(25)   Tang, K.; Shvartsburg, A. A.; Lee, H.-N.; Prior, D. C.; Buschbach, M. A.; Li, F.; Tolmachev, A. V.; Anderson, G. A.; Smith, R. D. High-Sensitivity Ion Mobility Spectrometry/Mass Spectrometry Using Electrodynamic Ion Funnel Interfaces. *Anal. Chem.* **2005**, *77* (10), 3330–3339.

(26)   Guevremont, R.; Siu, K. W. M.; Wang, J.; Ding, L. Combined Ion Mobility/Time-of-Flight Mass Spectrometry Study of Electrospray-Generated Ions. *Anal. Chem.* **1997**, *69* (19), 3959–3965.

(27)   Gillig, K. J.; Ruotolo, B.; Stone, E. G.; Russell, D. H.; Fuhrer, K.; Gonin, M.; Schultz, A. J. Coupling High-Pressure MALDI with Ion Mobility/Orthogonal Time-of-Flight Mass Spectrometry. *Anal. Chem.* **2000**, *72* (17), 3965–3971.

(28)   Gerlich, D. *In State Selected and State-to State Ion–Molecule Reaction Dynamics. Part 1. Experiment*; Wiley: New York, 1992; Vol. LXXXII.

(29)   Kim, T.; Tolmachev, A. V.; Harkewicz, R.; Prior, D. C.; Anderson, G.; Udseth, H. R.; Smith, R. D.; Bailey, T. H.; Rakov, S.; Futrell, J. H. Design and Implementation of a New Electrodynamic Ion Funnel. *Anal. Chem.* **2000**, *72* (10), 2247–2255.

(30)   Lynn, E. C.; Chung, M. C.; Han, C. C. Characterizing the Transmission Properties of an Ion Funnel. *Rapid Commun. Mass Spectrom.* **2000**, *14* (22), 2129–2134.

(31)   Javahery, G.; Thomson, B. A Segmented Radiofrequency-Only Quadrupole Collision Cell for Measurements of Ion Collision Cross Section on a Triple Quadrupole Mass Spectrometer. *J. Am. Soc. Mass Spectrom.* **1997**, *8* (7), 697–702.

(32)   McCullough, B. J.; Kalapothakis, J.; Eastwood, H.; Kemper, P.; MacMillan, D.; Taylor, K.; Dorin, J.; Barran, P. E. Development of an Ion Mobility Quadrupole Time of Flight Mass Spectrometer. *Anal. Chem.* **2008**, *80* (16), 6336–6344.

(33)   Covey, T.; Douglas, D. J. Collision Cross Sections for Protein Ions. *J. Am. Soc. Mass Spectrom.* **1993**, *4* (8), 616–623.

(34)   Gill, A. C.; Jennings, K. R.; Wyttenbach, T.; Bowers, M. T. Conformations of Biopolymers in the Gas Phase: A New Mass Spectrometric Method. *Int. J. Mass Spectrom.* **2000**, *195–196*, 685–697.

(35)   Thalassinos, K.; Slade, S. E.; Jennings, K. R.; Scrivens, J. H.; Giles, K.; Wildgoose, J.; Hoyes, J.; Bateman, R. H.; Bowers, M. T. Ion Mobility Mass Spectrometry of Proteins in a Modified Commercial Mass Spectrometer. *Int. J. Mass Spectrom.* **2004**, *236* (1–3), 55–63.

(36)   Zucker, S. M.; Ewing, M. A.; Clemmer, D. E. Gridless Overtone Mobility Spectrometry. *Anal. Chem.* **2013**, *85* (21), 10174–10179.

(37)   Tolmachev, A. V.; Webb, I. K.; Ibrahim, Y. M.; Garimella, S. V. B.; Zhang, X.; Anderson, G. A.; Smith, R. D. Characterization of Ion Dynamics in Structures for Lossless Ion Manipulations. *Anal. Chem.* **2014**, *86* (18), 9162–9168.

(38) Allen, S. J.; Giles, K.; Gilbert, T.; Bush, M. F. Ion Mobility Mass Spectrometry of Peptide, Protein, and Protein Complex Ions Using a Radio-Frequency Confining Drift Cell. *Analyst* **2016**, *141*, 884–891.

(39) Allen, S. J.; Schwartz, A. M.; Bush, M. F. Effects of Polarity on the Structures and Charge States of Native-Like Proteins and Protein Complexes in the Gas Phase. *Anal. Chem.* **2013**, *85* (24), 12055–12061.

(40) Silveira, J. A.; Jeon, J.; Gamage, C. M.; Pai, P.-J.; Fort, K. L.; Russell, D. H. Damping Factor Links Periodic Focusing and Uniform Field Ion Mobility for Accurate Determination of Collision Cross Sections. *Anal. Chem.* **2012**, *84* (6), 2818–2824.

(41) Silveira, J. A.; Gamage, C. M.; Blase, R. C.; Russell, D. H. Gas-Phase Ion Dynamics in a Periodic-Focusing DC Ion Guide. *Int. J. Mass Spectrom.* **2010**, *296* (1–3), 36–42.

(42) Blase, R. C.; Silveira, J. A.; Gillig, K. J.; Gamage, C. M.; Russell, D. H. Increased Ion Transmission in IMS: A High Resolution, Periodic-Focusing DC Ion Guide Ion Mobility Spectrometer. *Int. J. Mass Spectrom.* **2011**, *301* (1–3), 166–173.

(43) Gamage, C. M.; Silveira, J. A.; Blase, R. C.; Russell, D. H. Gas-Phase Ion Dynamics in a Periodic-Focusing DC Ion Guide (Part II): Discrete Transport Modes. *Int. J. Mass Spectrom.* **2011**, *303* (2–3), 154–163.

(44) Freeke, J.; Bush, M. F.; Robinson, C. V.; Ruotolo, B. T. Gas-Phase Protein Assemblies: Unfolding Landscapes and Preserving Native-like Structures Using Noncovalent Adducts. *Chem. Phys. Lett.* **2012**, *524*, 1–9.

(45) Hall, Z.; Politis, A.; Bush, M. F.; Smith, L. J.; Robinson, C. V. Charge-State Dependent Compaction and Dissociation of Protein Complexes: Insights from Ion Mobility and Molecular Dynamics. *J. Am. Chem. Soc.* **2012**, *134* (7), 3429–3438.

(46) Mason, E. A.; McDaniel, E. W. In *Transport Properties of Ions in Gases*; Wiley: New York, 1988; p 149.

(47) Mason, E. A.; McDaniel, E. W. In *Transport Properties of Ions in Gases*; Wiley: New York, 1988; p 154.

(48) Mason, E. A.; McDaniel, E. W. In *Transport Properties of Ions in Gases*; Wiley: New York, 1988; p 4.

(49) Shvartsburg, A. A.; Smith, R. D. Fundamentals of Traveling Wave Ion Mobility Spectrometry. *Anal. Chem.* **2008**, *80* (24), 9689–9699.

(50) Morsa, D.; Gabelica, V.; De Pauw, E. Effective Temperature of Ions in Traveling Wave Ion Mobility Spectrometry. *Anal. Chem.* **2011**, *83* (14), 5775–5782.

(51) Merenbloom, S. I.; Flick, T. G.; Williams, E. R. How Hot Are Your Ions in TWAVE Ion Mobility Spectrometry? *J. Am. Soc. Mass Spectrom.* **2011**, *23* (3), 553–562.

(52) Dahl, D. SIMION. *SIMION* version 8.0; Idaho National Engineering Laboratory: Idaho Falls, ID.

(53) Tolmachev, A. V.; Kim, T.; Udseth, H. R.; Smith, R. D.; Bailey, T. H.; Futrell, J. H. Simulation-Based Optimization of the Electrodynamic Ion Funnel for High Sensitivity Electrospray Ionization Mass Spectrometry. *Int. J. Mass Spectrom.* **2000**, *203* (1), 31–47.

(54) Shaffer, S. A.; Tolmachev, A.; Prior, D. C.; Anderson, G. A.; Udseth, H. R.; Smith, R. D. Characterization of an Improved Electrodynamic Ion Funnel Interface for Electrospray Ionization Mass Spectrometry. *Anal. Chem.* **1999**, *71* (15), 2957–2964.

(55) Tolmachev, A. V.; Chernushevich, I. V.; Dodonov, A. F.; Standing, K. G. A Collisional Focusing Ion Guide for Coupling an Atmospheric Pressure Ion Source to a Mass Spectrometer. *Nucl. Instrum. Methods Phys. Res. B* **1997**, *124* (1), 112–119.

(56) Schnier, P. D.; Price, W. D.; Jockusch, R. A.; Williams, E. R. Blackbody Infrared Radiative Dissociation of Bradykinin and Its Analogues: Energetics, Dynamics, and Evidence for Salt-Bridge Structures in the Gas Phase. *J. Am. Chem. Soc.* **1996**, *118* (30), 7178–7189.

(57) Marquardt, D. W. An Algorithm for Least-Squares Estimation of Nonlinear Parameters. *J. Appl. Math.* **1963**, *11* (2), 431–441.

CHAPTER 3

Ion Mobility Mass Spectrometry of Peptide, Protein, and Protein Complex Ions using a

Radio-Frequency Confining Drift Cell

This chapter is reproduced with permission from Allen, S. J.; Giles, K.; Gilbert, T.; Bush, M. F. "Ion Mobility Mass Spectrometry of Peptide, Protein, and Protein Complex Ions using a Radio-Frequency Confining Drift Cell" *Analyst* **2016**, *141*, 884–891. Copyright 2016 Royal Society of Chemistry.

3.1 Abstract

Ion mobility mass spectrometry experiments enable the characterization of mass, assembly, and shape of biological molecules and assemblies. Here, a new radio-frequency confining drift cell is characterized and used to measure the mobilities of peptide, protein, and protein complex ions. The new drift cell replaced the traveling-wave ion mobility cell in a Waters Synapt G2 HDMS. Methods for operating the drift cell and determining collision cross section values using this experimental set up are presented within the context of the original instrument control software. Collision cross sections for 349 cations and anions are reported, 155 of which are for ions that have not been characterized previously using ion mobility. The values for the remaining ions are similar to those determined using a previous radio-frequency confining drift cell and drift tubes without radial confinement. Using this device under 2 Torr of helium gas and an optimized drift voltage, denatured and native-like ions exhibited average apparent resolving powers of 14.2 and 16.5, respectively. For ions with high mobility, which are

also low in mass, the apparent resolving power is limited by contributions from ion gating. In contrast, the arrival-time distributions of low-mobility, native-like ions are not well explained using only contributions from ion gating and diffusion. For those species, the widths of arrival-time distributions are most consistent with the presence of multiple structures in the gas phase.

3.2 Introduction

Ion mobility has grown in popularity as a powerful gas-phase technique capable of rapid, efficient separation and structural characterization.[1] Ion mobility has been used for the analysis of explosives,[2] peptides,[3] proteins,[4] protein complexes,[5–10] and other biomolecules.[11] Many variations of this gas-phase technique exist (*e.g.*, differential mobility analysis,[12] trapped ion mobility spectrometry,[13] and traveling-wave ion mobility spectrometry[14]) that use different gas compositions, pressures, and electric fields, but are all ultimately designed to leverage differences in gas-phase ion transport that depend on shape and charge. Traditional ion mobility experiments measure the drift times of ions in a neutral background gas (typically helium, nitrogen, or air) under a weak electric field. These ion mobility experiments are usually operated in a low-field regime, in which the mobility of the ion (K, cm^2 V^{-1} s^{-1}) is independent of the applied drift field strength (V cm^{-1} Torr^{-1}).[15]

Traditional "direct-current-only" (DC-only) ion mobility drift tubes are composed of a series of ring electrodes with an applied DC voltage that changes linearly along the length of the drift tube.[16–20] The diffusion-limited resolving power depends on the thermal diffusion along the axis of transmission:[21,22]

$$\frac{t_D}{\Delta t_{diff}} = \frac{1}{4}\left(\frac{Vez}{k_B T \ln 2}\right)^{1/2}$$

(3.1)

where t_D is the ion drift time, Δt_{diff} is the full width at half maximum (FWHM) of the arrival-time distribution, V is the voltage change across the drift tube (drift voltage), e is the elementary charge, z is the charge state of the ion, k_B is the Boltzmann constant, and T is the drift-gas temperature. Maximizing the resolving power of ion mobility devices is critical for differentiating species with similar mobilities, and is thus an important parameter in the optimization and design of new ion mobility instrumentation. According to Equation 3.1, higher resolving power mobility measurements can be achieved by using higher drift voltages. Several implementations of linear, low-pressure, DC-only drift tubes have achieved very high resolving powers (73 to 150).[16–20] These instruments use pressures ranging from 1 to 15 Torr and low-field conditions, which can result in significant ion diffusion in the radial directions as ions traverse the drift tube. Often, ion funnels are placed at the end of the drift region to refocus ions. Ion funnels contain a constant DC potential gradient as well as alternating radio-frequency (RF) potentials that refocus ions to a narrow beam, to allow efficient transmission of ions for subsequent mass analysis.[23–26]

Here we characterize the performance of, and report methods for, a new RF-confining drift cell that has been integrated into a Waters Synapt G2 HDMS.[27] An RF-confining drift cell uses a constant DC potential gradient, similar to a DC-only drift tube, but also applies RF potentials to all electrodes (alternating phases applied to neighboring electrodes), similar to a stacked-ring ion guide. The applied RF potentials radially confine ions across the entire length of the drift cell. Collision cross section of 349 ions determined using this device are reported. These values can be used to calibrate traveling-wave ion mobility spectrometry experiments[28–32] and complement existing reference values available in the literature.[4,30,31,33–38] Mobility measurements of peptide, protein, and protein complex ions are compared to those from other

devices, demonstrating the accuracy of the values determined using this drift cell. The measured arrival-time distributions enable a critical evaluation of resolving power in these experiments. The apparent resolving powers observed here for peptide ions are significantly limited by contributions from ion gating. The low mobility and broad arrival-time distributions of native-like protein and protein complex ions are attributed to additional contributions to peak widths that are not accounted for by gating and diffusion alone. Overall, the new RF-confining drift cell was efficiently integrated into the commercial instrument and enables absolute mobility measurements for a broad range of analytes.

3.3 Experimental Methods

3.3.1 Ionization and Sample Preparation. Ions were formed by nanoelectrospray using borosilicate capillaries (0.78 mm inner diameter) with a tip at one end (1 to 3 µm inner diameter) pulled using a micropipette puller (Sutter Instruments model P–97, Novato, CA). A platinum wire placed in the open end of the capillary and in contact with the solution was used as the ionization electrode. Supporting Information Table S3.1 describes the sample preparation. Briefly, peptide and denatured protein analytes were electrosprayed from aqueous or aqueous/organic solutions containing either acid or base for positive or negative ion mode experiments, respectively. Most native-like proteins and protein complexes were electrosprayed from 200 mM ammonium acetate buffer solutions at pH = 7.0.

3.3.2 Instrumentation. All measurements were performed using a Synapt G2 HDMS (Waters Corporation, Wilmslow, UK) instrument in which the traveling-wave ion mobility cell was replaced by a new RF-confining drift cell. Voltages for most optics were minimized to reduce ion activation or unfolding. These voltages are reported in the ESI Example Waters

Synapt G2 HDMS Parameters File. Ions are introduced directly from the Trap Cell into the RF-confining drift cell (Supporting Information Figure S3.1). The new RF-confining drift cell is 25.2 cm long and consists of 168 gold-coated ring electrodes that are 0.5 mm thick, have center-to-center spacing of 1.5 mm, and an electrode inner diameter of 7 mm. Entrance and exit plates contain 2 mm apertures for ion transmission. The electrodes are connected to printed circuit boards that contain voltage divider networks consisting of 5 and 10 MΩ resistors that establish a uniform voltage drop (or drift voltage) across the drift cell (Supporting Information Figure S3.2). The circuitry of the printed circuit boards was designed such that the RF-confining drift cell uses the same electrical inputs as the original traveling-wave mobility cell, enabling the control of drift voltage from the original instrument software. The drift voltage is applied using four software parameters, as shown in Supporting Information Figure S3.2. The 25.05 cm drift region spans from the first electrode to the exit plate of the RF-confining drift cell. The peak-to-peak RF amplitude in the RF-confining drift cell was set at 100 V with a frequency of 2.8 MHz.

Ion gating and injection was controlled using a mobility trap height of 10 to 15 V and trapping release times ranging from 100 to 200 μs; longer times were used for larger protein and protein complex ions to improve sensitivity. Compared to the analogous traveling-wave ion mobility cell[27] the helium cell entrance plate was removed (Supporting Information Figure S3.1), which increases the conductance limit to the helium cell. Buffer gas was introduced using a new gas inlet system (Supporting Information Figure S3.3) that delivers gas to the center of the RF-confining drift cell, rather than the original mobility gas inlet located near the entrance of the drift region. These changes were made to minimize the net flow of gas along the longitudinal axis of the cell.

In this instrument, several factors contribute to obtaining optimal ion transmission and Gaussian-like arrival-time distributions. Ion transmission is improved for large (greater than 60 kDa) proteins and protein complexes when the source backing pressure is raised to 4 to 6 mbar, the Trap Cell flow rate is raised to 10 mL min^{-1}, and the Transfer Cell Exit is set to 0 V. Additionally, the Transfer Cell wave height is set at 2 to 4 V and the wave velocity is adjusted between 60 to 200 m s^{-1} to maximize transmission and retain the ion mobility separation.

3.3.3 Determining Collision Cross Sections. Methods for determining ion mobilities in an RF-confining drift cell are analogous to those for a DC-only drift tube. Ion velocities (v) are proportional to the mobility of an ion (K) and the applied electric field (E), which depends on the drift voltage (V) and the length (L) of the drift region:

$$v = KE = K\frac{V}{L} \tag{3.2}$$

Measured drift times in these experiments depend on the residence time in the drift cell (t_D) and the transport time of ions from the exit of the drift cell to the time-of-flight mass analyzer (t_0).

$$t_D = \frac{L^2}{K}\frac{1}{V} + t_0 \tag{3.3}$$

In this system, the drift voltage can be varied up to 354 V (Supporting Information Figure S3.2). The centroid of each arrival-time distribution is estimated by fitting the distribution to a Gaussian function using in-house software.[38] For most mobility experiments, drift times were measured at 10 drift voltages ranging from 104 to 354 V. Plotting drift time versus reciprocal drift voltage enables the determination of K from the slopes of the best-fit lines (Equation 3.3). Structural information can be obtained from ion mobility experiments by converting measured K into a collision cross section (Ω), which, to a first approximation, describes the orientationally-averaged projection of the ion-neutral interaction area.[39,40] Ω values were determined using the Mason-Schamp equation:[15]

$$\Omega = \frac{3ez}{16N} \left(\frac{2\pi}{\mu k_B T}\right)^{1/2} \frac{1}{K} \qquad (3.4)$$

where e is the elementary charge, z is the ion charge state, N is the drift-gas number density, μ is the reduced mass of the ion and drift gas, k_B is the Boltzmann constant, and T is the drift-gas temperature.

3.4 Results and Discussion

3.4.1 RF-Confining Drift Cells. Our objective was to develop a new ion mobility device that would enable absolute Ω measurements, while leveraging the broad range of ion selection, activation, and analysis capabilities of the Waters Synapt G2 HDMS. Modifying commercial instrumentation with ion mobility capabilities has been reported previously.[30,41–44] The first RF-confining drift cell[30] was implemented into a Waters Synapt G1 HDMS and has been used to measure mobilities for a broad range of biomolecules.[30,31,37,38,45] An RF-confining drift cell contains RF potentials that radially confine ions in addition to a DC voltage drop that is uniform across all electrodes. Other ion mobility devices that use RF-confinement include segmented quadrupole instruments[41,43] and a stacked-ring ion guide containing an axial DC field established by groups of four electrodes.[42] Compared to those devices that contain a "staircase-like" DC voltage drop, ions in an RF-confining drift cell experience a uniform voltage drop along the axis of transmission (Supporting Information Figure S3.4). The new RF-confining drift cell described here contains the same physical dimensions and electrical inputs as a Waters Synapt G2 HDMS traveling-wave ion mobility cell, but printed circuits boards now contain a voltage divider network that establishes a uniform voltage drop across the cell, in addition to a capacitor network to couple RF to all electrodes.

The main advantage of this device is that it enables direct and absolute Ω measurements with high sensitivity and without using external calibration, which is required for traveling-wave[28] and trapped[46] ion mobility spectrometry. Implementation using a Synapt G2 HDMS instrument, relative to a Synapt G1 HDMS instrument, takes advantage of access to higher drift voltages and an improved mass analyzer that has higher mass resolving power and dynamic range. Ion mobility measurements using this device can also be used in tandem with other manipulations that are possible on this platform, including collision-induced dissociation,[47] ion/ion chemistry,[48–50] and surface-induced dissociation.[51]

3.4.2 Collision Cross Sections. Representative ion mobility data acquired using the new RF-confining drift cell are shown in Figure 3.1A. This plot shows separation in drift time and m/z of different charge states (z) and chain lengths (n) of poly-DL-alanine anions, $(\text{Ala}_n - z\text{H})^{z-}$, in 2 Torr helium gas using a drift voltage of 104 V. Figure 3.1B shows drift times acquired for the $n = 11$ to 29 oligomers of $(\text{Ala}_n - 2\text{H})^{2-}$ measured at 10 drift voltages ranging from 104 to 354 V. This extremely linear response ($R^2 = 0.9998$) enables the determination of K from the slopes of the lines, which are then converted to Ω values. Ω values of singly and doubly charged poly-DL-alanine cations and anions measured in helium gas are shown in Figure 3.1C. Cations are significantly larger (up to 5%) than anions at lower n values, but at higher n values, Ω values between cations and anions are similar. $(\text{Ala}_n - \text{H})^{1-}$ and $(\text{Ala}_n - 2\text{H})^{2-}$ Ω values measured in helium and in nitrogen gas as well as $(\text{Ala}_n + \text{H})^{1+}$ measured in helium gas are reported in ESI Table S3.2; a subset of these values have been reported previously.[32,52]
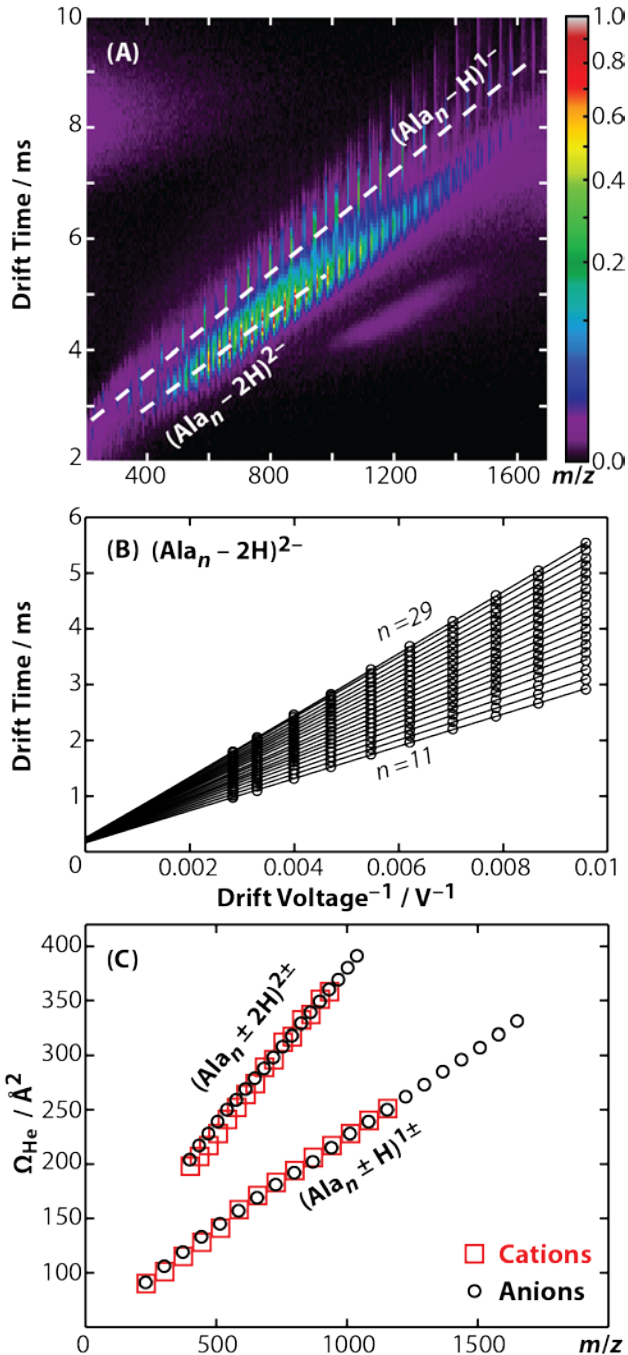
Figure 3.1. (A) Drift time versus m/z plot of poly-DL-alanine electrosprayed in

negative ion mode. The two-dimensional plot shows the separation of different

charge states and chain lengths (n); dashed lines represent the singly and doubly

charged series (($Ala_n - H)^{1-}$ and ($Ala_n - 2H)^{2-}$, respectively). (B) Drift time versus

reciprocal drift voltage plot of ($Ala_n - 2H)^{2-}$ for $n = 11$ to 29. (C) Collision cross

sections with helium gas (Ω_{He}) of singly and doubly charged cations (*red squares*) and anions (*black circles*) of poly-DL-alanine.

Ion mobility is also used to investigate the structures and assemblies of native-like proteins and protein complexes.[5–10] An example of a mobility separation of the 145 kDa protein complex glyceraldehyde-3-phosphate dehydrogenase using this RF-confining drift cell is shown in Figure 3.2A. Here we measured Ω values for cations and anions of 13 native-like proteins and protein complexes (Supporting Information Table S3.3), which complement values for 14 proteins and protein complexes that were measured using this drift cell and reported previously.[53] Consistent with earlier findings,[53] cations and anions had similar Ω values, but anions exhibited lower average charge states than cations. The Ω values for all protein and protein complex cations and anions measured using this cell are shown in Figure 3.2B. Values are the averages of Ω values of each observed charge state for a given sample. The data in Figure 3.2B show that native-like protein and protein complex mass and Ω values are correlated, suggesting that most of the proteins and protein complexes investigated here are relatively globular.

RF-confining drift cells enable the determination of absolute Ω values for a broad range of biomolecules. Supporting Information Tables S3.2 and S3.3 report 349 Ω values measured using this new RF-confining drift cell. Most values are the average of three technical replicate measurements made on separate days, which in all cases differed by less than 1%. These values include small molecules, peptides, denatured proteins, and native-like proteins and protein complexes. Supporting Information Figure S3.5 shows all Ω values measured using this device; the data include results for ions that span a wide range of *m/z* and Ω values. This data adds to a

growing body of evidence of the correlations between charge and protein mass[53–55] and provide a source of absolute Ω values that can be used for traveling-wave ion mobility calibration.
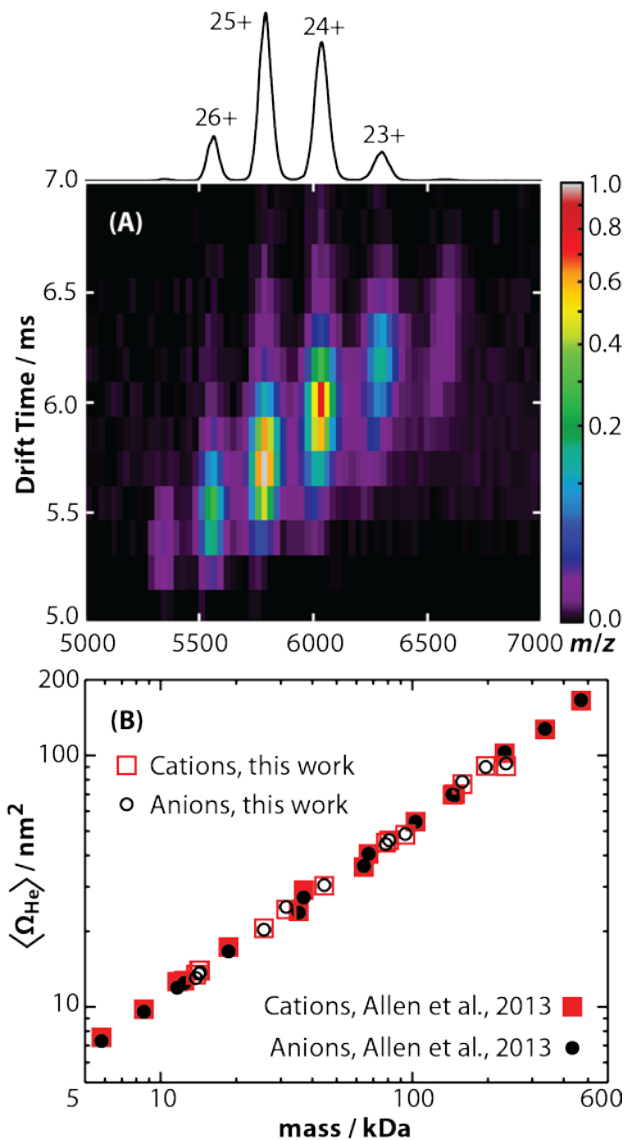
Figure 3.2. (A) Drift time versus *m/z* plot of native-like glyceraldehyde-3-phosphate dehydrogenase (145 kDa) electrosprayed in positive ion mode from a 200 mM ammonium acetate buffer solution. The projected mass spectrum is shown above and labeled with the assigned charge states. (B) Average collision cross sections with helium gas ($<\Omega_{He}>$) of native-like protein and protein complex

cations (*red squares*) and anions (*black circles*) ranging in mass from 5.8 to 468

kDa either reported here (*open symbols*) or previously (*closed symbols*).[53] Values

are plotted on log axes and are averages of all charge states for a given polarity of

a protein or protein complex (Supporting Information Table S3.3).

3.4.3 Comparisons to Other Ion Mobility Devices. Ω values for a wide mass range of

peptide, protein, and protein complex cations measured using this new RF-confining drift cell

(Supporting Information Tables S3.2 and S3.3) were compared to those measured using the

previous RF-confining drift cell that was implemented in a Waters Synapt G1 HDMS[30,31,38]

(Figure 3.3A). The relative differences between the two sets of data are shown in Figure 3.3B.

For the 102 ions measured using both cells, 61% have Ω values that are within ± 1% of one

another and 93% are within ± 2% of one another. For comparison, the absolute error in Ω values

determined using RF-confining drift cells have been estimated to be < 3%, based on propagation

of errors in drift times, pressure, and temperature.[30] On average, the Ω values measured here are

slightly less (0.3%) than those measured previously, but the systematic difference is small

relative to the standard deviation of the relative Ω values (1.1%). This comparison shows that

similar Ω values can be measured using both generations of RF-confining drift cells.

To further validate the Ω values determined using the RF-confining drift cell,

experimental Ω values of peptides and denatured proteins are compared to those measurements

made using DC-only drift tubes (Supporting Information Table S3.4).[4,19,33–36] Note, only ions

that have a single reported Ω value from each measurement are compared. Ω values of these

analytes measured in helium gas using the new RF-confining drift cell are on average slightly

smaller (–0.6% ± 1.5%) than those measured on other devices. In general, comparing Ω values

measured here to those measured on the previous RF-confining drift cell and other DC-only drift tubes indicate that Ω values determined using these approaches are statistically similar.
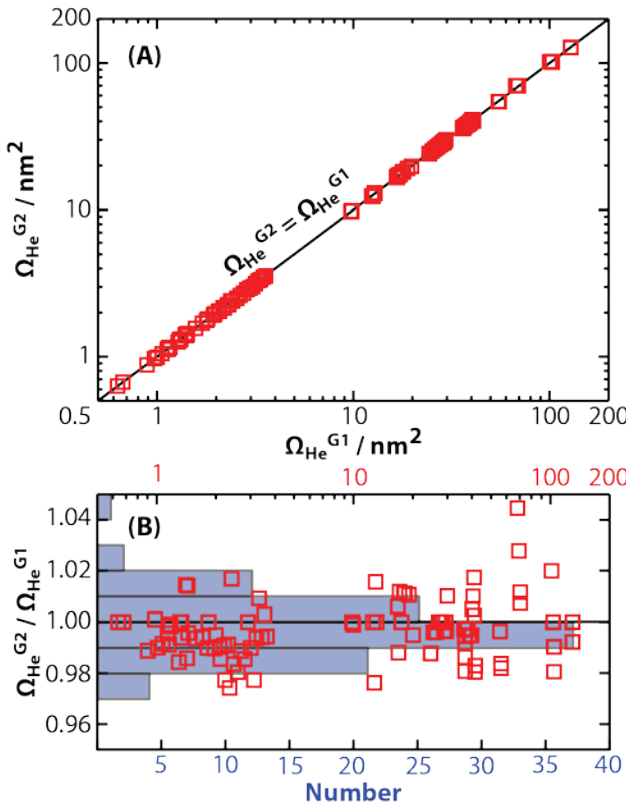
Figure 3.3. (A) Collision cross sections with helium gas measured using the 2nd generation RF-confining drift cell described here (Ω_{He}^{G2}) are compared to those measured using the 1st generation device (Ω_{He}^{G1}).[30,31,38] Values are plotted on log axes along with the line $\Omega_{He}^{G2} = \Omega_{He}^{G1}$. (B) The ratios of Ω_{He}^{G2} to Ω_{He}^{G1} (*red squares*) are plotted versus Ω_{He}^{G1} on a log scale (top axis). An overlayed histogram (*blue*, number of measurements) shows that the Ω_{He}^{G2} and Ω_{He}^{G1} are within ± 2% of each other for 93% of the analyte ions.

3.4.4 Peak Widths and Resolving Powers. The peptide GRGDS, which has been used previously to characterize the resolving power of several other mobility instruments,[19,27,56] was used to characterize the performance of this device. The highest apparent resolving power measured for GRGDS[1+] in 2 Torr helium gas was 16.0. This value was calculated by correcting t_D for t_0 and dividing by experimental full width at half maximum (Δt_{exp}) determined from fitting a Gaussian function to the arrival-time distribution. Interestingly, the highest apparent resolving power was measured for the lowest drift voltage of 104 V, whereas resolving power increases with drift voltage in Equation 3.1. To isolate only the contributions of peak widths to resolving power in these experiments, the subsequent analysis focuses on peak width as a function of reciprocal drift voltage. Experimentally measured Δt_{exp} values for GRGDS[1+] ranged from 126 to 237 μs for drift voltages from 354 to 104 V, respectively (Figure 3.4A). These values are larger than those predicted using diffusion-limited theory (Δt_{diff}, Equation 3.1). This suggests that there are additional contributions to the observed peak width, for example the temporal width of the initial ion population prior to the ion mobility separation (Δt_{gate}). The combined peak width ($\Delta t_{combined}$):[21,22]

$$\Delta t_{combined}^2 = \Delta t_{diff}^2 + \Delta t_{gate}^2 \tag{3.5}$$

therefore more completely describes the total peak width.

Figure 3.4A shows a least-squares minimization of the difference between Δt_{exp} and $\Delta t_{combined}$, which indicates that Δt_{gate} is 124 μs. This value is similar to the trapping release time of 150 μs used for GRGDS experiments. Differences between the two values may be attributable to the assumption in Equation 3.5 that the initial pulse of ions gated into the drift cell has a Gaussian shape, whereas contributions due to space-charge effects or distortions while gating are also possible. More generally, Δt_{gate} is similar to Δt_{exp} in these experiments, suggesting that the

resolving power is significantly limited by contributions from ion gating, but at longer drift times, *i.e.*, low drift voltages, contributions from Δt_{gate} are proportionally less significant. A recent study found that resolving powers that account for gating contributions to peak width compare well to experimental results of the peptide SDGRG (the inverse peptide of GRGDS) using a DC-only drift tube.[57]

A similar analysis was performed for the 25+ charge state of native-like glyceraldehyde-3-phosphate dehydrogenase, which is a 145 kDa homotetramer. Δt_{exp} values measured under 2 Torr of helium gas are shown in Figure 3.4B. Least-squares fitting of $\Delta t_{combined}$ to Δt_{exp} results in a Δt_{gate} of 269 μs that does not fit the data appropriately (Supporting Information Figure S3.6). Instead, an upper limit of 200 μs (the trapping release time used in these experiments) was used as Δt_{gate} to calculate $\Delta t_{combined}$. As shown in Figure 3.4B, plotting $\Delta t_{combined}$ by accounting for Δt_{gate} does not accurately model experimental results. This result suggests that additional contributions, such as an ensemble of conformers with different Ω values, may contribute to the broad peak widths measured in these experiments. This interpretation is consistent with reports that the peak widths for small monomeric protein ions are broader than expected based on diffusion-broadening alone.[4,58–60] For example, the arrival-time distributions for ubiquitin have been reported to be greater than that expected for a single conformer[60] and using tandem ion mobility methods, these arrival-time distributions have been shown to contain an ensemble of conformers.[59] Therefore, the peak widths in these current experiments may be better explained using a set of discrete conformers or using semi-empirical peak width theory.[61]
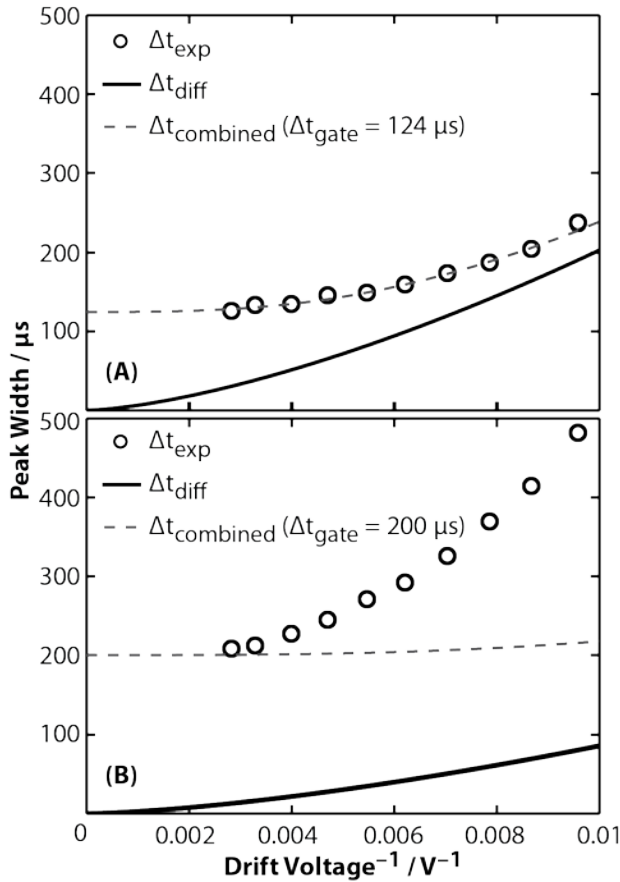
Figure 3.4. Analysis of full width at half maximum (peak width, Δt) as a function of reciprocal drift voltage. (A) Experimental peak widths (Δt_{exp}, *black circles*) of GRGDS[1+] are greater than those expected using diffusion-limited theory from Equation 3.1 (Δt_{diff}, *solid line*). Instead, the combined peak width ($\Delta t_{combined}$, *dashed line*) accurately models Δt_{exp} with a Δt_{gate} of 124 μs. (B) Similar to results for GRGDS[1+], experimental peaks widths (Δt_{exp}, *black circles*) of the 25+ charge state of glyceraldehyde-3-phosphate dehydrogenase are greater than those expected using diffusion-limited theory from Equation 3.1 (Δt_{diff}, *solid line*). Using a Δt_{gate} of 200 μs to model $\Delta t_{combined}$ (*dashed line*) in these experiments results in good agreement for the highest drift voltage. Significant deviations are

exhibited for lower drift voltages, suggesting additional contributions to Δt_{exp} that

are not accounted for in Equation 3.5.

To characterize the peak widths of biomolecular ions more generally, the apparent

resolving power was calculated for the cations listed in Supporting Information Tables S3.2 and

S3.3. These results were divided into two classes (1) peptides and denatured proteins and (2)

native-like proteins and protein complexes. Figure 3.5A shows histograms of apparent resolving

powers at each drift voltage for peptide and denatured protein ions. Similar to the observation for

GRGDS, the lowest drift voltage of 104 V results in the highest average apparent resolving

power of 14.2. Measured peak widths for these ions, which are highly mobile, are attributed

predominated by contributions from ion gating, rather than contributions from diffusion at high

drift voltages. The histograms of apparent resolving powers for native-like protein and protein

complex ions are shown in Figure 3.5B. In contrast to Figure 3.5A, native-like protein and

protein complex ions exhibit the highest apparent resolving powers (on average 16.5) at

intermediate drift voltages. This is attributable to a balance between contributions from diffusion,

gating, and coexisting structural isomers. Note, the apparent resolving power for cations and

anions measured using this device are similar. Apparent resolving powers at higher drift voltages

could likely be improved by changing ion gating conditions to reduce Δt_{gate}, increasing the drift

cell pressure, or using heavier buffer gas molecules in order to decrease the relative contribution

of Δt_{gate} to Δt_{exp}.
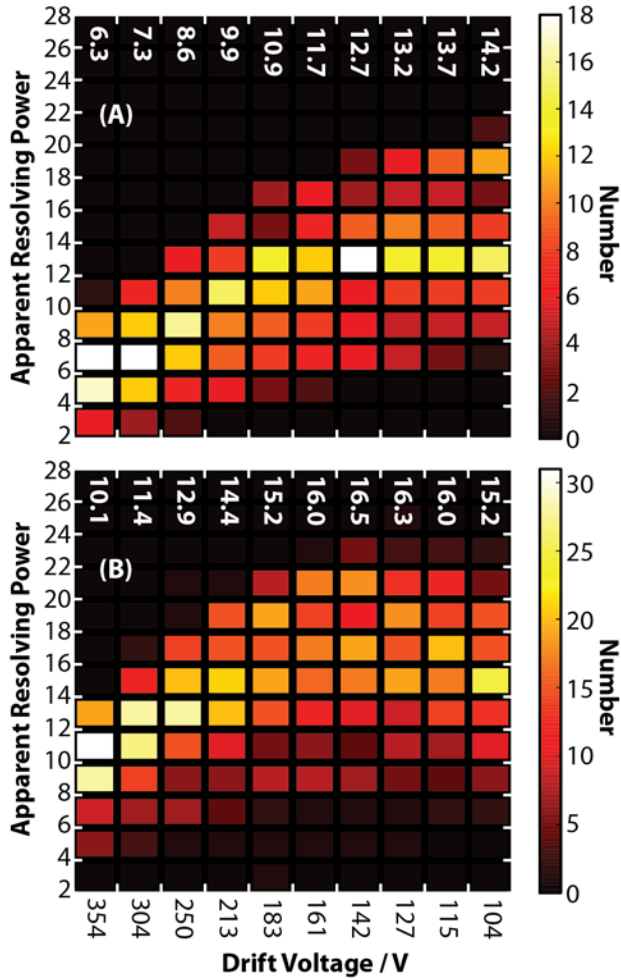
Figure 3.5. Apparent resolving power measured in 2 Torr helium gas at 10 drift voltages ranging from 104 to 354 V for (A) peptide and denatured protein ions and (B) native-like protein and protein complex ions. Each column, or drift voltage, represents a histogram consisting of the number of analytes that exhibited an apparent resolving power within a given bin. For example, for the highest drift voltage in panel (A), one analyte exhibits an apparent resolving power between 10 and 12, 11 analytes between 8 and 10, 18 analytes between 6 and 8, 17 analytes between 4 and 6, and six analytes between 2 and 4. Under these conditions, peptide and denatured protein ions exhibit the highest apparent resolving power at the lowest drift voltage (104 V), whereas protein and protein complex ions, on

average, have the highest apparent resolving power at an intermediate drift voltage of 142 V. The average apparent resolving power of each drift voltage is provided at the top of (A) and (B).

3.5 Conclusions

A new RF-confining drift cell was developed and implemented in a Waters Synapt G2 HDMS. This device has been shown to yield precise and accurate Ω values for a broad mass range of peptides, proteins, and protein complexes. On average, this device yields Ω values that are very similar to those measured using a previous RF-confining drift cell (0.3% average difference) or DC-only drift tubes (0.6% average difference). The apparent resolving power in these experiments is the result of contributions from ion gating, diffusion, and additional factors. For most high-mobility ions, the highest apparent resolving power is observed at the lowest drift voltages for which the relative contributions from ion gating are less prevalent. In contrast, low-mobility proteins and protein complexes yield the highest apparent resolving powers at intermediate drift voltages as a result of more significant contributions to peak widths from relatively broad structural distributions of native-like ions in the gas phase.

The broadscale evaluation of apparent resolving power for native-like protein and protein complex ions provides new insights the structural diversity of gas-phase ions. In particular, these results provide benchmarks for evaluating the peaks widths of analytes of unknown structure. Although improvement in ion mobility instrumentation that increase resolving powers (e.g. increased drift voltage and decreased trapping release times) may generate narrower peaks of some ions, this data suggests that limitations in high apparent resolving power measurements of

protein and protein complex ions may be a result of inherent structural diversity that will be difficult to overcome by incremental improvements in instrumentation.

3.6 Acknowledgements

3.7 Supporting Information Available

Supporting Information Figures S3.1 to S3.6, Tables S3.1 to S3.4, and Example Waters Synapt G2 HDMS Parameters File. This material is available free of charge via internet at http://dx.doi.org/10.1039/c5an02107c.

3.8 References

(1)   Lanucara, F.; Holman, S. W.; Gray, C. J.; Eyers, C. E. The Power of Ion Mobility-Mass Spectrometry for Structural Characterization and the Study of Conformational Dynamics. *Nat. Chem.* **2014**, *6* (4), 281–294.

(2)   Roscioli, K. M.; Davis, E.; Siems, W. F.; Mariano, A.; Su, W.; Guharay, S. K.; Hill, H. H. Modular Ion Mobility Spectrometer for Explosives Detection Using Corona Ionization. *Anal. Chem.* **2011**, *83* (15), 5965–5971.

(3)   Thalassinos, K.; Grabenauer, M.; Slade, S. E.; Hilton, G. R.; Bowers, M. T.; Scrivens, J. H. Characterization of Phosphorylated Peptides Using Traveling Wave-Based and Drift Cell Ion Mobility Mass Spectrometry. *Anal. Chem.* **2009**, *81* (1), 248–254.

(4)   Shelimov, K. B.; Clemmer, D. E.; Hudgins, R. R.; Jarrold, M. F. Protein Structure in Vacuo: Gas-Phase Conformations of BPTI and Cytochrome c. *J. Am. Chem. Soc.* **1997**, *119* (9), 2240–2248.

(5)   Ekeowa, U. I.; Freeke, J.; Miranda, E.; Gooptu, B.; Bush, M. F.; Perez, J.; Teckman, J.; Robinson, C. V.; Lomas, D. A. Defining the Mechanism of Polymerization in the Serpinopathies. *Proc. Natl. Acad. Sci. U. S. A.* **2010**, *107* (40), 17146–17151.

(6)   Uetrecht, C.; Barbu, I. M.; Shoemaker, G. K.; van Duijn, E.; Heck, A. J. R. Interrogating Viral Capsid Assembly with Ion Mobility–mass Spectrometry. *Nat. Chem.* **2011**, *3* (2), 126–132.

(7)   Zhou, M.; Politis, A.; Davies, R. B.; Liko, I.; Wu, K.-J.; Stewart, A. G.; Stock, D.; Robinson, C. V. Ion Mobility–mass Spectrometry of a Rotary ATPase Reveals ATP-Induced Reduction in Conformational Flexibility. *Nat. Chem.* **2014**, *6* (3), 208–215.

(8)   Scarff, C. A.; Almeida, B.; Fraga, J.; Macedo-Ribeiro, S.; Radford, S. E.; Ashcroft, A. E. Examination of Ataxin-3 (Atx-3) Aggregation by Structural Mass Spectrometry Techniques: A Rationale for Expedited Aggregation upon Polyglutamine (polyQ) Expansion. *Mol Cell Proteomics* **2015**, *14* (5), 1241–1253.

(9)   Scott, D.; Layfield, R.; Oldham, N. J. Structural Insights into Interactions between Ubiquitin Specific Protease 5 and Its Polyubiquitin Substrates by Mass Spectrometry and Ion Mobility Spectrometry. *Prot. Sci.* **2015**, *24* (8), 1257–1263.

(10)   Zhao, Y.; Singh, A.; Li, L.; Linhardt, R. J.; Xu, Y.; Liu, J.; Woods, R. J.; Amster, I. J. Investigating Changes in the Gas-Phase Conformation of Antithrombin III upon Binding of Arixtra Using Traveling Wave Ion Mobility Spectrometry (TWIMS). *Analyst* **2015**, *140* (20), 6980–6989.

(11)   Fenn, L. S.; Kliman, M.; Mahsut, A.; Zhao, S. R.; McLean, J. A. Characterizing Ion Mobility-Mass Spectrometry Conformation Space for the Analysis of Complex Biological Samples. *Anal. Bioanal. Chem.* **2009**, *394* (1), 235–244.

(12)   Hogan, C. J.; de la Mora, J. F. Ion Mobility Measurements of Non-Denatured 12-150 kDa Proteins and Protein Multimers by Tandem Differential Mobility Analysis – Mass Spectrometry (DMA-MS). *J. Am. Soc. Mass Spectrom.* **2011**, *22* (1), 158–172.

(13)   Silveira, J. A.; Ridgeway, M. E.; Park, M. A. High Resolution Trapped Ion Mobility Spectrometery of Peptides. *Anal. Chem.* **2014**, *86* (12), 5624–5627.

(14)   Zhong, Y.; Hyung, S.-J.; Ruotolo, B. T. Characterizing the Resolution and Accuracy of a Second-Generation Traveling-Wave Ion Mobility Separator for Biomolecular Ions. *Analyst* **2011**, *136* (17), 3534.

(15)   Mason, E. A.; McDaniel, E. W. *Transport Properties of Ions in Gases*; Wiley: New York, 1988.

(16)   Tang, K.; Shvartsburg, A. A.; Lee, H.-N.; Prior, D. C.; Buschbach, M. A.; Li, F.; Tolmachev, A. V.; Anderson, G. A.; Smith, R. D. High-Sensitivity Ion Mobility Spectrometry/Mass Spectrometry Using Electrodynamic Ion Funnel Interfaces. *Anal. Chem.* **2005**, *77* (10), 3330–3339.

(17)   Koeniger, S. L.; Merenbloom, S. I.; Valentine, S. J.; Jarrold, M. F.; Udseth, H. R.; Smith, R. D.; Clemmer, D. E. An IMS−IMS Analogue of MS−MS. *Anal. Chem.* **2006**, *78* (12), 4161–4174.

(18)   Baker, E. S.; Clowers, B. H.; Li, F.; Tang, K.; Tolmachev, A. V.; Prior, D. C.; Belov, M. E.; Smith, R. D. Ion Mobility Spectrometry—mass Spectrometry Performance Using Electrodynamic Ion Funnels and Elevated Drift Gas Pressures. *J. Am. Soc. Mass Spectrom.* **2007**, *18* (7), 1176–1187.

(19)   Kemper, P. R.; Dupuis, N. F.; Bowers, M. T. A New, Higher Resolution, Ion Mobility Mass Spectrometer. *Int. J. Mass Spectrom.* **2009**, *287* (1–3), 46–57.

(20)   Ibrahim, Y. M.; Baker, E. S.; Danielson III, W. F.; Norheim, R. V.; Prior, D. C.; Anderson, G. A.; Belov, M. E.; Smith, R. D. Development of a New Ion Mobility Time-of-Flight Mass Spectrometer. *Int. J. Mass Spectrom.* **2015**, *377*, 655–662.

(21)   Revercomb, H. E.; Mason, E. A. Theory of Plasma Chromatography/Gaseous Electrophoresis. Review. *Anal. Chem.* **1975**, *47* (7), 970–983.

(22)   Kanu, A. B.; Gribb, M. M.; Hill, H. H. Predicting Optimal Resolving Power for Ambient Pressure Ion Mobility Spectrometry. *Anal. Chem.* **2008**, *80* (17), 6610–6619.

(23)   Shaffer, S. A.; Tolmachev, A.; Prior, D. C.; Anderson, G. A.; Udseth, H. R.; Smith, R. D. Characterization of an Improved Electrodynamic Ion Funnel Interface for Electrospray Ionization Mass Spectrometry. *Anal. Chem.* **1999**, *71* (15), 2957–2964.

(24)   Kim, T.; Tolmachev, A. V.; Harkewicz, R.; Prior, D. C.; Anderson, G.; Udseth, H. R.; Smith, R. D.; Bailey, T. H.; Rakov, S.; Futrell, J. H. Design and Implementation of a New Electrodynamic Ion Funnel. *Anal. Chem.* **2000**, *72* (10), 2247–2255.

(25)   Lynn, E. C.; Chung, M. C.; Han, C. C. Characterizing the Transmission Properties of an Ion Funnel. *Rapid Commun. Mass Spectrom.* **2000**, *14* (22), 2129–2134.

(26)   Ibrahim, Y.; Tang, K.; Tolmachev, A. V.; Shvartsburg, A. A.; Smith, R. D. Improving Mass Spectrometer Sensitivity Using a High-Pressure Electrodynamic Ion Funnel Interface. *J. Am. Soc. Mass Spectrom.* **2006**, *17* (9), 1299–1305.

(27)   Giles, K.; Williams, J. P.; Campuzano, I. Enhancements in Travelling Wave Ion Mobility Resolution. *Rapid Commun. Mass Spectrom.* **2011**, *25* (11), 1559–1566.

(28)   Ruotolo, B. T.; Benesch, J. L. P.; Sandercock, A. M.; Hyung, S.-J.; Robinson, C. V. Ion Mobility–mass Spectrometry Analysis of Large Protein Complexes. *Nat. Protoc.* **2008**, *3* (7), 1139–1152.

(29)   Smith, D. P.; Knapman, T. W.; Campuzano, I.; Malham, R. W.; Berryman, J. T.; Radford, S. E.; Ashcroft, A. E. Deciphering Drift Time Measurements from Travelling Wave Ion Mobility Spectrometry-Mass Spectrometry Studies. *Eur. J. Mass Spectrom.* **2009**, *15* (2), 113–130.

(30)   Bush, M. F.; Hall, Z.; Giles, K.; Hoyes, J.; Robinson, C. V.; Ruotolo, B. T. Collision Cross Sections of Proteins and Their Complexes: A Calibration Framework and Database for Gas-Phase Structural Biology. *Anal. Chem.* **2010**, *82* (22), 9557–9565.

(31)   Salbo, R.; Bush, M. F.; Naver, H.; Campuzano, I.; Robinson, C. V.; Pettersson, I.; Jørgensen, T. J. D.; Haselmann, K. F. Traveling-Wave Ion Mobility Mass Spectrometry of Protein Complexes: Accurate Calibrated Collision Cross-Sections of Human Insulin Oligomers. *Rapid Commun. Mass Spectrom.* **2012**, *26* (10), 1181–1193.

(32)   Forsythe, J. G.; Petrov, A. S.; Walker, C. A.; Allen, S. J.; Pellissier, J. S.; Bush, M. F.; Hud, N. V.; Fernández, F. M. Collision Cross Section Calibrants for Negative Ion Mode Traveling Wave Ion Mobility-Mass Spectrometry. *Analyst* **2015**, *140* (20), 6853–6861.

(33)   Valentine, S. J.; Counterman, A. E.; Clemmer, D. E. Conformer-Dependent Proton-Transfer Reactions of Ubiquitin Ions. *J. Am. Soc. Mass Spectrom.* **1997**, *8*, 954–961.

(34)   Counterman, A. E.; Valentine, S. J.; Srebalus, C. A.; Henderson, S. C.; Hoaglund, C. S.; Clemmer, D. E. High-Order Structure and Dissociation of Gaseous Peptide Aggregates That Are Hidden in Mass Spectra. *J. Am. Soc. Mass Spectrom.* **1998**, *9* (8), 743–759.

(35)   Henderson, S. C.; Li, J.; Counterman, A. E.; Clemmer, D. E. Intrinsic Size Parameters for Val, Ile, Leu, Gln, Thr, Phe, and Trp Residues from Ion Mobility Measurements of Polyamino Acid Ions. *J. Phys. Chem. B* **1999**, *103* (41), 8780–8785.

(36)   Liu, Y.; Valentine, S. J.; Clemmer, D. E. *Unpublished Results* http://www.indiana.edu/~clemmer/Research/Cross%20Section%20Database/cs_database.php.

(37) Campuzano, I.; Bush, M. F.; Robinson, C. V.; Beaumont, C.; Richardson, K.; Kim, H.; Kim, H. I. Structural Characterization of Drug-like Compounds by Ion Mobility Mass Spectrometry: Comparison of Theoretical and Experimentally Derived Nitrogen Collision Cross Sections. *Anal. Chem.* **2012**, *84* (2), 1026–1033.

(38) Bush, M. F.; Campuzano, I. D. G.; Robinson, C. V. Ion Mobility Mass Spectrometry of Peptide Ions: Effects of Drift Gas and Calibration Strategies. *Anal. Chem.* **2012**, *84* (16), 7124–7130.

(39) Mesleh, M. F.; Hunter, J. M.; Shvartsburg, A. A.; Schatz, G. C.; Jarrold, M. F. Structural Information from Ion Mobility Measurements: Effects of the Long-Range Potential. *J. Phys. Chem.* **1996**, *100* (40), 16082–16086.

(40) Wyttenbach, T.; Bleiholder, C.; Bowers, M. T. Factors Contributing to the Collision Cross Section of Polyatomic Ions in the Kilodalton to Gigadalton Range: Application to Ion Mobility Measurements. *Anal. Chem.* **2013**, *85* (4), 2191–2199.

(41) Javahery, G.; Thomson, B. A Segmented Radiofrequency-Only Quadrupole Collision Cell for Measurements of Ion Collision Cross Section on a Triple Quadrupole Mass Spectrometer. *J. Am. Soc. Mass Spectrom.* **1997**, *8* (7), 697–702.

(42) Thalassinos, K.; Slade, S. E.; Jennings, K. R.; Scrivens, J. H.; Giles, K.; Wildgoose, J.; Hoyes, J.; Bateman, R. H.; Bowers, M. T. Ion Mobility Mass Spectrometry of Proteins in a Modified Commercial Mass Spectrometer. *Int. J. Mass Spectrom.* **2004**, *236* (1–3), 55–63.

(43) Guo, Y.; Wang, J.; Javahery, G.; Thomson, B. A.; Siu, K. W. M. Ion Mobility Spectrometer with Radial Collisional Focusing. *Anal. Chem.* **2005**, *77* (1), 266–275.

(44) McCullough, B. J.; Kalapothakis, J.; Eastwood, H.; Kemper, P.; MacMillan, D.; Taylor, K.; Dorin, J.; Barran, P. E. Development of an Ion Mobility Quadrupole Time of Flight Mass Spectrometer. *Anal. Chem.* **2008**, *80* (16), 6336–6344.

(45) Pagel, K.; Harvey, D. J. Ion Mobility–Mass Spectrometry of Complex Carbohydrates: Collision Cross Sections of Sodiated N-Linked Glycans. *Anal. Chem.* **2013**, *85* (10), 5138–5145.

(46) Hernandez, D. R.; DeBord, J. D.; Ridgeway, M. E.; Kaplan, D. A.; Park, M. A.; Fernandez-Lima, F. Ion Dynamics in a Trapped Ion Mobility Spectrometer. *Analyst* **2014**, *139* (8), 1913–1921.

(47) Rabuck, J. N.; Hyung, S.-J.; Ko, K. S.; Fox, C. C.; Soellner, M. B.; Ruotolo, B. T. Activation State-Selective Kinase Inhibitor Assay Based on Ion Mobility-Mass Spectrometry. *Anal. Chem.* **2013**, *85* (15), 6995–7002.

(48) Pepin, R.; Laszlo, K. J.; Peng, B.; Marek, A.; Bush, M. F.; Tureček, F. Comprehensive Analysis of Gly-Leu-Gly-Gly-Lys Peptide Dication Structures and Cation-Radical Dissociations Following Electron Transfer: From Electron Attachment to Backbone Cleavage, Ion–Molecule Complexes, and Fragment Separation. *J. Phys. Chem. A* **2014**, *118* (1), 308–324.

(49) Lermyte, F.; Konijnenberg, A.; Williams, J. P.; Brown, J. M.; Valkenborg, D.; Sobott, F. ETD Allows for Native Surface Mapping of a 150 kDa Noncovalent Complex on a Commercial Q-TWIMS-TOF Instrument. *J. Am. Soc. Mass Spectrom.* **2014**, *25* (3), 343–350.

(50) Laszlo, K. J.; Bush, M. F. Analysis of Native-Like Proteins and Protein Complexes Using Cation to Anion Proton Transfer Reactions (CAPTR). *J. Am. Soc. Mass Spectrom.* **2015**, *26* (12), 2152–2161.

(51) Zhou, M.; Jones, C. M.; Wysocki, V. H. Dissecting the Large Noncovalent Protein Complex GroEL with Surface-Induced Dissociation and Ion Mobility–Mass Spectrometry. *Anal. Chem.* **2013**, *85* (17), 8262–8267.

(52) Paglia, G.; Williams, J. P.; Menikarachchi, L.; Thompson, J. W.; Tyldesley-Worster, R.; Halldórsson, S.; Rolfsson, O.; Moseley, A.; Grant, D.; Langridge, J.; et al. Ion Mobility Derived Collision Cross Sections to Support Metabolomics Applications. *Anal. Chem.* **2014**, *86* (8), 3985–3993.

(53) Allen, S. J.; Schwartz, A. M.; Bush, M. F. Effects of Polarity on the Structures and Charge States of Native-Like Proteins and Protein Complexes in the Gas Phase. *Anal. Chem.* **2013**, *85* (24), 12055–12061.

(54) Fernandez de la Mora, J. Electrospray Ionization of Large Mutliply Charged Species Proceeds via Dole's Charged Residue Mechanism. *Anal. Chim. Acta* **2000**, *406* (1), 93–104.

(55) Heck, A. J. R.; van den Heuvel, R. H. H. Investigation of Intact Protein Complexes by Mass Spectrometry. *Mass Spectrom. Rev.* **2004**, *23* (5), 368–389.

(56) Wu, C.; Siems, W. F.; Klasmeier, J.; Hill, H. H. Separation of Isomeric Peptides Using Electrospray Ionization/High-Resolution Ion Mobility Spectrometry. *Anal. Chem.* **2000**, *72* (2), 391–395.

(57) May, J. C.; Dodds, J. N.; Kurulugama, R. T.; Stafford, G. C.; Fjeldsted, J. C.; McLean, J. A. Broadscale Resolving Power Performance of a High Precision Uniform Field Ion Mobility-Mass Spectrometer. *Analyst* **2015**, *140* (20), 6824–6833.

(58) Wyttenbach, T.; Kemper, P. R.; Bowers, M. T. Design of a New Electrospray Ion Mobility Mass Spectrometer. *International Journal of Mass Spectrometry* **2001**, *212* (1–3), 13–23.

(59) Koeniger, S. L.; Merenbloom, S. I.; Clemmer, D. E. Evidence for Many Resolvable Structures within Conformation Types of Electrosprayed Ubiquitin Ions. *J. Phys. Chem. B* **2006**, *110* (13), 7017–7021.

(60) Wyttenbach, T.; Bowers, M. T. Structural Stability from Solution to the Gas Phase: Native Solution Structure of Ubiquitin Survives Analysis in a Solvent-Free Ion Mobility–Mass Spectrometry Environment. *J. Phys. Chem. B* **2011**, *115* (42), 12266–12275.

(61) Siems, W. F.; Wu, C.; Tarver, E. E.; Hill, H. H. J.; Larsen, P. R.; McMinn, D. G. Measuring the Resolving Power of Ion Mobility Spectrometers. *Anal. Chem.* **1994**, *66* (23), 4195–4201.

CHAPTER 4

Analysis of Native-like Ions using Structures for Lossless Ion Manipulations

This chapter is reproduced with permission from Allen, S. J.; Eaton, R. M.; Bush, M. F. "Analysis of Native-like Ions using Structures for Lossless Ion Manipulations" *Analytical Chemistry* **2016**, *88*, 9118–9126. Copyright 2016, American Chemical Society.

4.1 Abstract

Ion mobility separation of native-like protein and protein complex ions expands the structural information available through native mass spectrometry analysis. Here, we implement Structures for Lossless Ion Manipulations (SLIM) for the analysis of native-like ions. SLIM has been shown previously to operate with near lossless transmission of ions up to 3000 Da in mass. Here for the first time, SLIM was used to separate native-like protein and protein complex ions ranging in mass from 12 to 145 kDa. The resulting arrival-time distributions were monomodal and were used to determine collision cross section values that are within 3% of those determined from radio-frequency confining drift cell measurements. These results are consistent with the retention of native-like ion structures throughout these experiments. The apparent resolving powers of native-like ions measured using SLIM are as high as 42, which is the highest value reported directly from experimental data for the native-like ion of a protein complex. Interestingly, the apparent resolving power depends strongly on the identity of the analyte, suggesting that the arrival-time distributions of these ions may have contributions from an ensemble of structures in the gas phase that is unique to each analyte. These results suggest that

the broad range of emerging SLIM technologies may all be adaptable to the analysis of native-like ions, which will enable future applications in the areas of structural biology, biophysics, and biopharmaceutical characterization.

4.2 Introduction

Native ion mobility mass spectrometry (IMMS) is a powerful gas-phase technique used to probe the structures of proteins and their non-covalent complexes.[1] IM separates ions based on their shape and charge. Low-resolution shape information of native-like ions can be quantified by determining a collision cross section (Ω), which to a first approximation, depends on the orientationally-averaged projected area of the ion-neutral pair.[2,3] Ω and mass are complementary, and results from hybrid IMMS measurements are used to characterize the structures and assembly pathways of noncovalent complexes in solution. For example, IMMS spectra of norovirus capsid proteins under high pH conditions show evidence for coexisting assemblies that contain 18, 40, 60, and 80 copies of the capsid protein and have Ω values that are consistent with sheet-like structures.[4] These assemblies are consistent with intermediates that are capable of forming capsids (rather than assembly-incompetent aggregates).[4] In another report, IMMS showed that with increasing oligomer size, complexes of Aβ(25-32) peptide transition from isotropic growth to β-sheet structures, which are associated with oligomer toxicity.[5] Interestingly, interactions with either epigallocatechin gallate or scyllo-inositol, which inhibit the formation of fibrils of Aβ42,[6] suppressed the formation of Aβ(25-32) peptide oligomers with β-sheet structures,[5] suggesting a molecular basis for fibril inhibition. These and other studies suggest that IMMS is a fast and sensitive technique for characterizing the structures, assemblies, and stability of proteins in solution.[7–10]

Instrumentation for conventional IMMS has improved greatly in recent years. The simplest device for determining the Ω of an ion is an electrostatic drift tube, which consists of a series of ring electrodes that are connected to a voltage divider network to create a constant DC-potential gradient along the length of the drift region.[11–17] To refocus radially diffuse ions, an ion funnel may be positioned at the end of the drift region.[12] Ion funnels are composed of incrementally-decreasing internal diameter electrodes that contain a constant DC gradient in addition to alternating RF potentials that radially confine ions.[18–20] Additionally, the use of RF potentials to mitigate radial diffusion during IM has been implemented in segmented quadrupoles,[21,22] traveling-wave IM cells,[23] a gridless overtone drift tube,[24] RF-confining drift cells,[25–27] and trapped IM cells.[28] For native IMMS, the vast majority of measurements have used traveling-wave IM or RF-confining drift cells.[25,29]

Structures for Lossless Ion Manipulations (SLIM) is an emerging technology for IMMS that uses a parallel pair of printed circuit boards to deliver potentials to electrodes that are deposited directly onto the boards.[30] Depending on the design of the boards and potentials applied, SLIM devices can be used to separate ions along a linear path, analogous to conventional IM, but also redirect, select, accumulate, trap, and activate ions.[30–38] SLIM boards use DC potentials to establish electric fields for IM separations and a combination of DC and RF potentials to confine ions. In the initial designs,[30–35,37] a series of planar "rung" electrodes are used to establish a constant DC gradient along the axis of transmission and limit ion diffusion towards the boards using RF potentials. Two series of "guard" electrodes are placed on both sides of the rung electrodes and establish DC potentials that limit ion diffusion in the transversal direction. More recently, SLIM boards with dynamic DC potentials (traveling waves) were also used to separate ions.[36,39] Current implementations of SLIM devices have demonstrated lossless

transmission of Agilent Tuning Mix ions and low molecular weight peptide ions (all with masses

less than 3000 Da)[31] and lossless trapping for alkylammonium ions (with masses of 466 and 690

Da).[34] Other benefits of SLIM include the low cost of printed circuit board fabrication and the

modularity of individual SLIM designs, which offer exciting prospects for future

multidimensional IM experiments.

Here, a new SLIM instrument was developed using a linear path of SLIM boards to

measure the mobilities of native-like protein and protein complex ions. In this implementation of

SLIM, ion transport is controlled by a constant DC gradient along the axis of transmission, rather

than dynamic DC potentials (traveling waves).[36,39,40] Native-like ions were generated by

nanoelectrospray ionization from buffered solutions at biologically relevant pHs to generate

desolvated ions that contain folded structures and retain non-covalent interactions.[41] An ion

funnel trap was used to accumulate and inject ions into a drift region that contains six pairs of

SLIM boards and two focusing ion funnels. A rectangular ion funnel[42] facilitated ion

transmission from the ion funnel trap into the region between top-bottom SLIM board pairs, and

a rear circular ion funnel transferred ions to a quadrupole/time-of-flight mass spectrometer. Ω

values of native-like protein and protein complex ions with nitrogen determined using this

instrument are similar to those determined using an RF-confining drift cell.[25] The monomodal

arrival-time distributions Ω values of these ions suggest that there is minimal ion activation

through SLIM devices under these conditions. Ion trajectory simulations and statistical

arguments are used to estimate the effective temperatures of the native-like ions of avidin (64

kDa homotetramer) in SLIM, and those values are only slightly elevated (298.6 to 299.3 K)

relative to standard ambient temperature. Additionally, the highest apparent resolving power

measured using this device (42) is also the highest value reported directly from experimental data

for a native-like ion of a protein complex. More generally, this work shows that native-like ion

structures can be preserved through SLIM analysis and that future native IMMS experiments will

be able to leverage the broad range of SLIM technologies that are being developed for the

analysis of comparatively small ions.

4.3 Methods

4.3.1 Sample Preparation and Ionization. The electrokinetic, nanoelectrospray

ionization source[43] and the preparation for all samples[27] have been reported previously. Briefly,

all native-like protein and protein complex samples were prepared to 10 μM protein in 200 mM

ammonium acetate at a pH of 7.0.

4.3.2 Instrumentation. The new SLIM system was implemented on the front-end of an

existing Waters Q-Tof Premier mass spectrometer (Figure 4.1). The atmospheric pressure

interface consists of a 0.25 mm inner diameter stainless steel capillary inlet that is 76.2 mm long

and was heated to 80 ℃ to assist with droplet desolvation. Desolvated ions pass into a chamber

that contains an ion funnel trap[16,44] and then a second vacuum chamber that contains the

rectangular ion funnel,[42] SLIM boards, and circular ion funnel.[16,18] For each of the funnels,

individual electrode boards were fabricated by depositing a thin layer of gold-coated copper

along the inner edge of the aperture of the printed circuit board.[16] Resistors and capacitors were

soldered directly to individual boards; board-to-board connections are made using miniature

spring-loaded connectors. Additional details of the ion funnel trap, rectangular ion funnel, and

circular ion funnel are described in the Supporting Information.
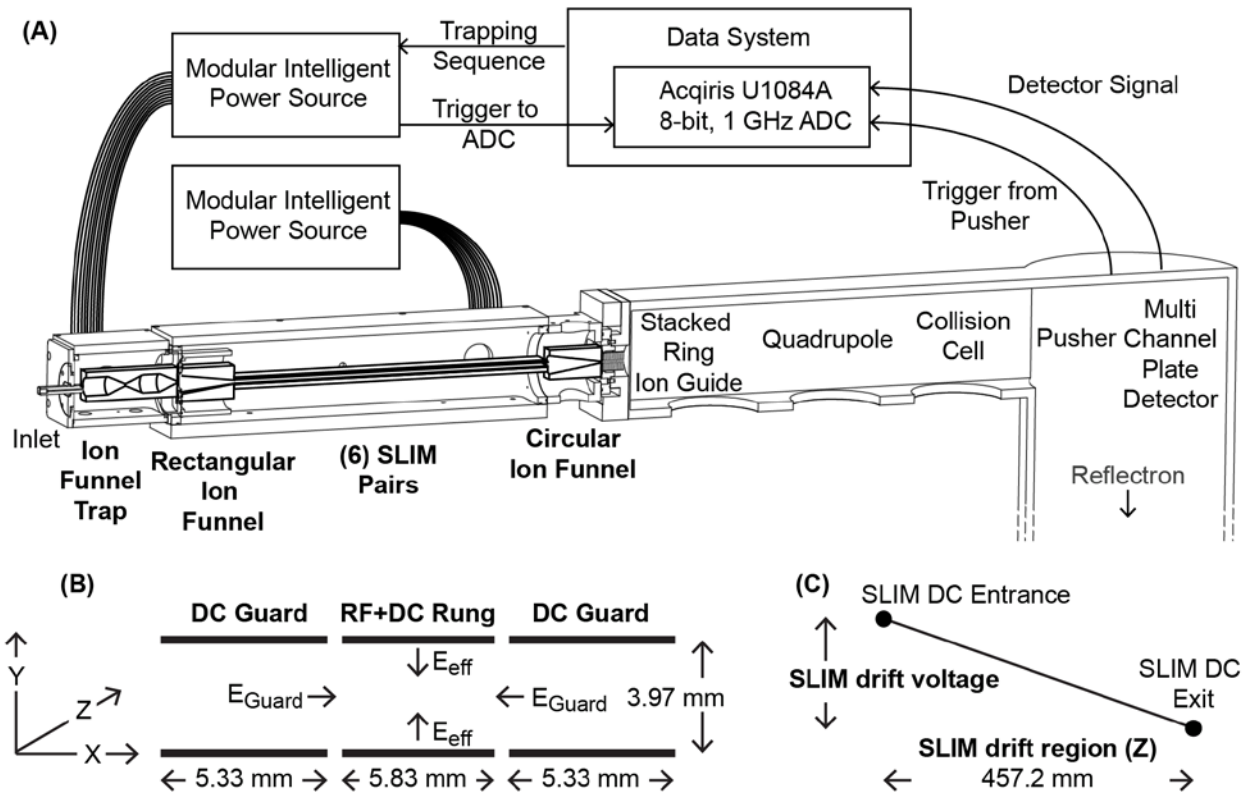
Figure 4.1. (A) Schematic diagram of the instrument used for these experiments. An ion funnel trap,[16,44] rectangular ion funnel,[42] six SLIM board pairs, and circular ion funnel[16,18] were positioned in front of the stacked-ring ion guide of a Waters Q-Tof Premier mass spectrometer. Each SLIM board was 7.62 cm by 7.62 cm and the gap between each top-bottom pair was 3.97 mm. All voltages in the Waters Q-Tof Premier are controlled using the original electronics and MassLynx. Most other DC voltages and RF waveforms are supplied by two Modular Intelligent Power Sources (MIPS), which are controlled by a data acquisition system that also houses a fast analog-to-digital convertor (ADC). During mobility experiments, one of the MIPS boxes produces time-dependent DC voltages that are used to control the potentials of the grids in the ion funnel trap and trigger the ADC to initiate data acquisition. (B) Dimensions of SLIM and

the DC (E_{guard}) and effective potential[20,30] (E_{eff}) fields experienced by ions. (C) The SLIM drift voltage is the difference between the DC voltages at the entrance and exit of the SLIM region. The DC voltage applied to each rung electrode is incremented monotonically, which creates a constant DC gradient along the axis of transmission.

Each SLIM board is a 7.62 cm by 7.62 cm printed circuit board that contains 50 RF and DC rung electrodes and 26 DC guard electrodes bordering either side of the rungs. The rung electrodes are 0.76 mm by 5.33 mm, with an electrode center-to-center spacing of 1.52 mm. Guard electrodes 2 through 25 are 2.81 mm by 5.83 mm and guard electrodes 1 and 26 are 1.28 mm by 5.83 mm, with a spacing of 0.25 mm between adjacent electrodes. Six, top-bottom pairs of boards (twelve total) were assembled using fiberglass braces to form a 45.72 cm drift region (Supporting Information Figure S4.1). Bridging boards with long, gold-coated pins were used to establish electrical connections between both adjacent and top-bottom pairs of SLIM boards. Stainless steel spacers were placed between the top-bottom board pairs to separate those boards by 3.97 mm.

Ions exiting the SLIM region are transferred into a circular ion funnel,[16,18] through a conductance limit, and then into the stacked-ring ion guide of the original Waters Q-Tof Premier. The stacked ring ion guide and collision cell of the original Waters Q-Tof Premier use traveling waves; the velocities and heights of those waves were selected to transport ions at the velocity of the traveling waves in a mobility independent fashion.[40]

4.3.3 Pressures. Pressures in the ion funnel trap chamber and the SLIM chamber were monitored independently using two absolute capacitance manometers (Baratron Type 626B,

MKS Instruments, Andover, MA). Nitrogen gas, from liquid nitrogen vapor, was introduced into the SLIM chamber using a mass flow controller (EL-Flow 500 mL minute^{-1}, Bronkhorst, Bethlehem, PA). Operating pressures of 4.00 and 4.05 Torr in the ion funnel trap and SLIM chamber, respectively, were achieved by supplying ~ 60 mL minute^{-1} nitrogen to the SLIM chamber and adjusting the conductance limit between the ion funnel trap chamber and an oil-free pump (XDS35i, Edwards, Crawley, United Kingdom) using a diaphragm valve (Edwards Speedivalve SP25).

4.3.4 Voltages and Data Acquisition. A voltage divider network is used to monotonically increment the DC voltage applied to each rung electrode, therefore creating a constant DC gradient along the axis of transmission in between the entrance and exit of the SLIM region (Figure 4.1C). Drift times were measured at SLIM drift voltages, which is the difference between the DC voltages at the entrance and exit of the SLIM region, of 234, 259, 291, 331, and 385 V. Most voltages for the new SLIM system were supplied using two Modular Intelligent Power Sources (MIPS, GAA Custom Engineering, Benton City, WA). The voltage for SLIM guard DC-out was biased relative to the rung DC-out voltage using a Keysight Technologies U8001A power supply (Santa Rosa, CA). All optics in the original Waters Q-Tof Premier were controlled using MassLynx. Typical field strengths for ion transmission are provided in Supporting Information Figure S4.2. The ion funnel trap RF was operated at a peak-to-peak amplitude (V_{PP}) of 110 V and a frequency of 955 kHz. To minimize any phase difference between the rectangular ion funnel and the SLIM boards, the capacitor networks of both were connected to the same high-power RF Q-head (GAA Custom Engineering), which supplied RF potentials with a V_{PP} of 200 V and a frequency of 980 kHz. The circular ion funnel contained RF potentials operated at V_{PP} of 100 V and a frequency of 979 kHz.

Mobility experiments were conducted using data acquisition software (Falkor) developed by Pacific Northwest National Laboratory that communicated with an 8-bit, 1 GHz analog-to-digital converter (ADC, Keysight Technologies Acqiris U1084A, Santa Rosa, CA) and the MIPS boxes. During mobility experiments, one of the MIPS boxes produces time-dependent DC voltages that are used to trigger the ADC to initiate data acquisition and control the potentials of the grids in the ion funnel trap. For all experiments described here, the exit grid in the ion funnel trap was increased by 15 V to accumulate and trap ions. This potential was reduced for a 600 μs trapping release time to inject a packet of ions for mobility separation.

4.3.5 RF-Confining Drift Cell Measurements. RF-confining drift cell measurements reported here were conducted using methods described previously.[27] Briefly, drift times were acquired at 8 drift voltages ranging from 180 to 385 V. The RF-confining drift cell contained 1.5 Torr nitrogen gas for measurements of all analytes except cytochrome *c*, which was analyzed under 1.0 Torr nitrogen gas to reduce ion activation during injection into the drift region. All measurements used a trapping release time of 100 μs to inject a packet of ions for mobility separation. The RF-confining drift cell contained RF potentials with V_{PP} of 100 V at a frequency of 2.8 MHz.

4.3.6 Ion Simulations and Effective Temperatures. A recently introduced statistical approach was then used to estimate the effective temperature of these ions.[45] Briefly, ion trajectories were simulated in SIMION 8.1 using the HS1 hard-sphere approximation for elastic ion-neutral collisions.[46] Mean free paths of the 16+ charge state of avidin were estimated using Ω values reported here. Computational models of a RF-confining drift cell with a 7 mm inner diameter were constructed using the dimensions reported previously.[45] SLIM models were constructed using the dimensions outlined above. Laboratory-frame ion velocities (v_i, where $i =$

x, *y*, and *z*) were recorded immediately prior to ion-neutral collisions in the trajectory simulations. Neutral gas velocities (V_i) sampled from a Maxwell-Boltzmann distribution at standard ambient temperature (T = 298.15 K) and v_i were used to calculate relative ion-neutral speeds:

$$s = \sqrt{\sum_{i=x,y,z}(v_i - V_i)^2} \qquad (4.1)$$

Using a Levenberg–Marquardt least-squares minimization algorithm,[47] the difference between histograms of relative ion-neutral speeds and the Maxwell-Boltzmann speed distribution was minimized by optimizing the temperature (*T*). The Maxwell-Boltzmann speed distribution is defined as:

$$f(s) = \left(\frac{\mu}{2\pi k_B T}\right)^{3/2} 4\pi s^2 e^{\frac{-\mu s^2}{2k_B T}} \qquad (4.2)$$

where μ is the ion-neutral reduced mass and k_B is the Boltzmann constant. *T* values determined using this approach represent effective temperatures estimated by fitting the Maxwell-Boltzmann speed distribution to relative ion-neutral speed distributions calculated from ion trajectory simulations.

4.4 Results and Discussion

4.4.1 Separation of Protein and Protein Complex Ions Using SLIM. Figure 4.2 shows an IMMS separation of concanavalin A in 4 Torr nitrogen gas at a SLIM field strength of 6.43 V cm^{-1} using the new SLIM instrument. This plot shows *m/z* and drift time separation of the monomer (25.7 kDa), dimer (51.5 kDa), and tetramer (103 kDa) of concanavalin A (CONA), which coexist in solution under equilibrium conditions.[48,49] Notably, this example shows transmission and separation of ions ranging from *m/z* ~2500 to 6000 through SLIM devices. Native-like ions of cytochrome *c* (CYTC), avidin (AVD), and glyceraldehyde-3-phosphate

dehydrogenase (G3PD) were also analyzed using the same methods. These ions span a range of masses (12 to 145 kDa), oligomeric states, and sizes.[25,27] These results, for the first time, demonstrate the use of SLIM devices to separate native-like ions of proteins and protein complexes. Previously, SLIM had only been demonstrated for analytes with masses less than 3000 Da.[31,32,36]
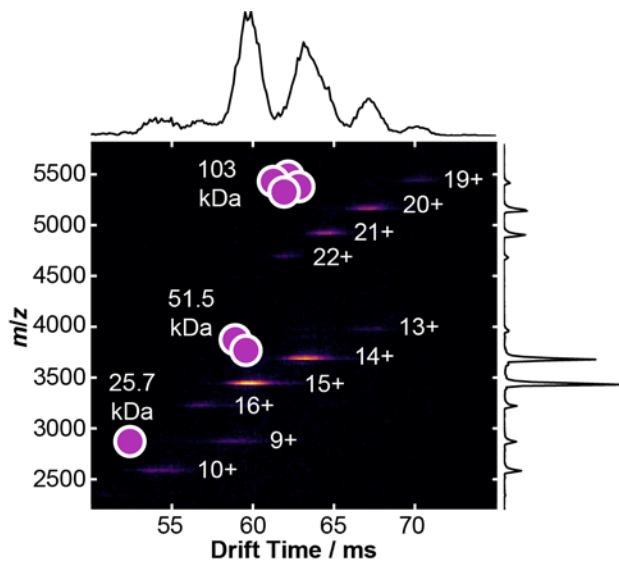
Figure 4.2. *m/z* versus drift time plot of concanavalin A electrosprayed from an aqueous solution containing 200 mM ammonium acetate at pH 7.0. The DC potentials used for this experiment are shown in Supporting Information Figure S4.2. These results demonstrate simultaneous analysis of the monomer, dimer, and tetramer of this protein.

Transmission of native-like ions of proteins and protein complexes depends most strongly on the peak-to-peak amplitude (V_{PP}) of the RF waveform applied to the rung electrodes; transmission of higher *m/z* ions increases with V_{PP} over the range investigated (150 to 200 V). For example, Supporting Information Figure S4.3 shows transmission of monomer, dimer, and

tetramer oligomers of CONA over a range of V_{PP}. At V_{PP} values less than 180 V, tetramer ions are not transmitted efficiently and the overall ion transmission is biased towards lower m/z values. For all mobility experiments reported here, the DC potential of the guard electrodes were biased by +1 V relative to that of the corresponding rung electrodes. Arrival-time distributions acquired using bias voltages greater than +2 V had trailing edges and centroided drift times that were shifted to longer drift times.

4.4.2 Mobilities of Native-Like Ions. Figure 4.3A shows arrival-time distributions of the 21+ charge state of CONA tetramer using SLIM drift voltages ranging from 234 to 385 V in 4 Torr nitrogen gas. The arrival-time distributions contain some structure that may be attributable to synchronization[29] of the frequencies of the traveling waves used to transport ions through the Waters Q-Tof Premier collision cell and the pusher of the time-of-flight mass analyzer. Similar experiments for native-like ions of selected charge states of CYTC, AVD, CONA, and G3PD are shown in Figure 4.3B, represented as drift time (t_D) versus reciprocal SLIM drift voltage. There is a clear linear relationship between t_D and reciprocal SLIM drift voltage for each ion, with correlation coefficients ranging from 0.9979 to 0.9999 for each ion.

For electrostatic drift tubes, the drift velocity of an ion (v_D) depends on the applied electric field (E) and the mobility of the ion (K):

$$v_D = KE = K\frac{V}{L} \tag{4.3}$$

where E is equal to the applied drift voltage (V) divided by the length of the drift region (L). For this study, V will refer to the DC voltage difference across the SLIM region, which we will refer to as the SLIM drift voltage. DC potentials in the rectangular ion funnel, circular ion funnel, and Waters Q-Tof Premier were held constant. t_D values are inversely proportional to K and V and also depend on ion transport times outside of the drift region (t_0):

$$t_D = \frac{L^2}{K}\frac{1}{V} + t_0 \tag{4.4}$$

t_0 in this analysis includes ion transport times through the post-trapping region in the ion funnel trap, rectangular ion funnel, circular ion funnel, and Waters Q-Tof Premier. This approach has been used previously to determine K values based on measurements made using both electrostatic drift tubes and other IM devices that use RF-confining potentials[22,25,27] that agree well with each other. The linearity of the data in Figure 4.3B suggests that it is also appropriate to use this approach to determine K for ions based on SLIM experiments, despite the differences between this instrument and electrostatic drift tubes.

Figure 4.3C shows the residuals between the experimental t_D and the best-fit lines shown in Figure 4.3B. The data show that there are systematic deviations, but that the differences between the experimental t_D and the best-fit lines are less than $\pm$ 0.5 ms, which is small relative to the overall t_D of those analytes (40 to 85 ms). These non-linear trends may have contributions from mobility dampening from high RF-potentials[45] or from the trajectories of ions that are localized close to electrodes on the SLIM boards[30] (thus experience a more staircase-like drift field). These effects can likely be further mitigated by varying the board spacing relative to rung-to-rung spacing, analogous to approaches to improve transmission for ion funnels[20] and reduce mobility dampening for RF confining drift cells.[45] Alternatively, contributions from mobility dampening may be accounted for empirically, analogous to the dampening factor that has been used to improve the accuracy of Ω values determined using periodic-focusing IM.[50]
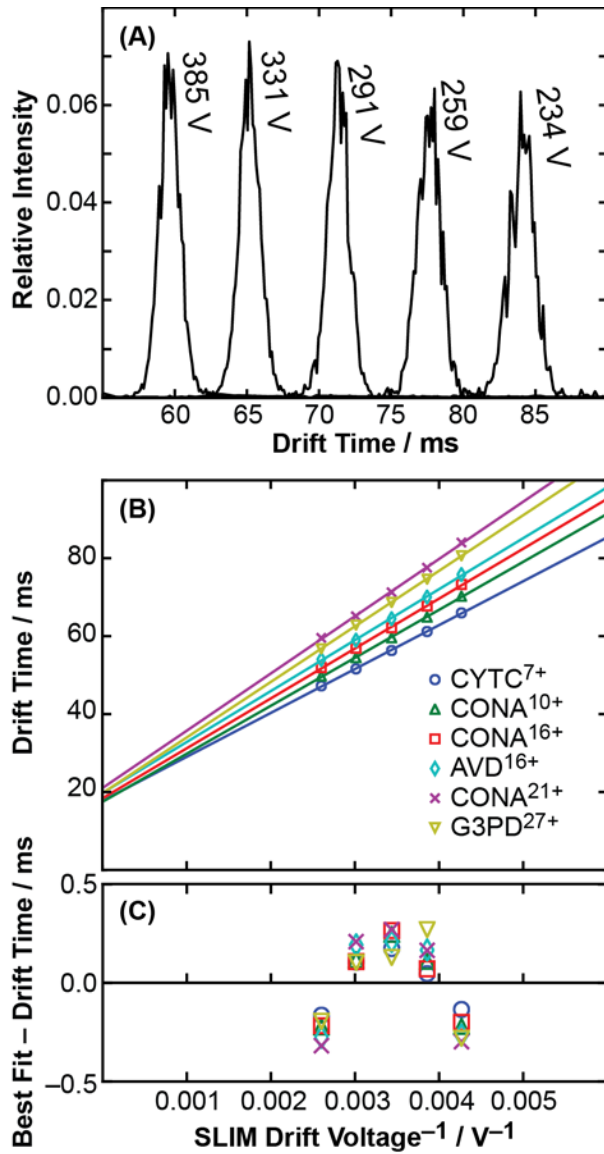
Figure 4.3. (A) Arrival-time distributions of the 21+ charge state of concanavalin

A tetramer measured at five SLIM drift voltages ranging from 234 to 385 V in 4

Torr nitrogen gas. Each arrival-time distribution is normalized such that the

integral of each is one. (B) Centroided drift time versus reciprocal SLIM drift

voltage plot of selected native-like ions of cytochrome *c* monomer (CYTC^{7+}),

concanavalin A monomer (CONA^{10+}), concanavalin A dimer (CONA^{16+}), avidin

tetramer (AVD^{16+}), concanavalin A tetramer (CONA^{21+}), and glyceraldehyde-3-

phosphate dehydrogenase tetramer (G3PD[27+]). The best-fit lines of each data set are included. (C) Residual plots (best fit minus experimental drift time) of the results in panel B.

4.4.3 Collision Cross Sections. Ω values were calculated using the K values determined experimentally in the preceding section and the Mason-Schamp equation:[2]

$$\Omega = \frac{3ez}{16N}\left(\frac{2\pi}{\mu k_B T}\right)^{1/2}\frac{1}{K} \tag{4.5}$$

where e is the elementary charge, z is the ion charge state, N is the drift-gas number density, μ is the reduced mass of the ion and drift gas, k_B is the Boltzmann constant, and T is the drift-gas temperature (300 K).

For the first time using SLIM, Ω values for native-like ions were determined. SLIM Ω values (Ω_{SLIM}) of CYTC, CONA monomer, CONA dimer, AVD, CONA tetramer, and G3PD are reported in Table 4.1. To evaluate their accuracy, Ω_{SLIM} values were compared with those determined using a first-generation RF-confining drift cell (Ω_{RFG1})[25] and Ω values with nitrogen determined in this study using a second-generation RF-confining drift cell (Ω_{RFG2}),[27] which are also reported in Table 4.1. The absolute error of the RF-confining drift cell derived Ω values are estimated to be less than 3%.[25,27] Ω_{SLIM} plotted versus Ω_{RFG1} and Ω_{RFG2} is shown in Figure 4.4. The average percentage difference between Ω_{SLIM} and Ω_{RFG1} is 1.0%, with Ω_{SLIM}, on average, being slightly less than Ω_{RFG1}. Similarly, the average percentage difference between Ω_{SLIM} and Ω_{RFG2} is 2.0%, with Ω_{SLIM}, on average, being slightly less than Ω_{RFG2}. However, the percentage difference between Ω_{SLIM} and Ω_{RFG2} is biased due to Ω_{RFG2} values of CYTC, which appear to probe activated structures. For CYTC analysis in the second-generation RF-confining drift cell, significant evidence for ion structural isomerization was observed even at reduced nitrogen

pressures (1.0 Torr) and drift cell injection voltages. Ions in those experiments are likely

activated as they are injected from the low-pressured trapping region (9 x 10^{-3} Torr) to the

nitrogen-filled RF-confining drift cell. Excluding Ω values of CYTC yields an average

percentage difference between Ω_{SLIM} and Ω_{RFG2} of the remaining analytes of 0.3%, with Ω_{SLIM}, on

average, being slightly less than Ω_{RFG2}. In general, Figure 4.4 shows that Ω values measured

using SLIM are similar to those measured using RF-confining drift cells and thus can also be

used for structural applications.

Table 4.1. Collision cross sections with nitrogen.

Analyte	n^a	mass / Da	z	Ω_{SLIM} / nm^2	$\Omega_{RFG2}{}^b$ / nm^2	$\Omega_{RFG1}{}^c$ / nm^2
cytochrome c	1	12.4k	6	14.5	15.9	14.9
			7	15.6	19.7	15.9
concanavalin A	1	25.7k	9	23.3	23.6	-
			10	24.1	24.3	-
concanavalin A	2	51.5k	14	39.5	39.6	-
			15	39.9	39.9	-
			16	40.4	40.5	-
avidin	4	64.3k	15	41.2	40.6	41.5
			16	41.5	40.8	41.5
			17	41.7	41.0	41.6
concanavalin A	4	103k	19	59.2	60.6	60.6
			20	60.2	60.6	60.8
			21	60.7	60.6	60.9
			22	60.3	60.7	60.5
glyceraldehyde-3-phosphate dehydrogenase	4	145k	24	73.3	74.9	-
			25	74.5	75.3	-
			26	75.8	75.7	-
			27	75.7	75.6	-

[a] Oligomeric state.

[b] Values determined here using the second-generation RF-confining drift cell.[27]

[c] Values reported previously using the first-generation RF-confining drift cell.[25]

To further validate this approach, Ω_{SLIM} were measured for native-like ions of ubiquitin. Ω_{SLIM} for native-like ubiquitin 5+, which is the most intense peak in the mass spectrum, is 1204 Å^2. This value is very similar to the Ω with nitrogen calculated for the N-state of ubiquitin using the projection superposition approximation (1209 Å^2)[51] and those determined experimentally for the compact structure of ubiquitin 6+ determined using electrostatic drift tube (1200 Å^2)[51] and trapped ion mobility spectrometry (1217 Å^2)[52] experiments. Note ions in those experiments were generated from acetonitrile/water[51] or acidified water[52] solutions and 6+ was the lowest charge state observed in those experiments. The ions in the present experiments were generated from 200 mM aqueous ammonium acetate at pH 7.0, which will yield ions with comparatively lower charge states due to competition with ion evaporation.[26,53] Ω_{SLIM} for native-like ubiquitin 6+, which was the only other charge state observed, is 1258 Å^2 and slightly smaller than the values for the compact conformer of ubiquitin 7+ determined using electrostatic drift tube (1270 Å^2)[51] and trapped ion mobility spectrometry (1283 Å^2)[52] experiments. These comparisons provide further support that native-like structures are preserved in the SLIM experiments.
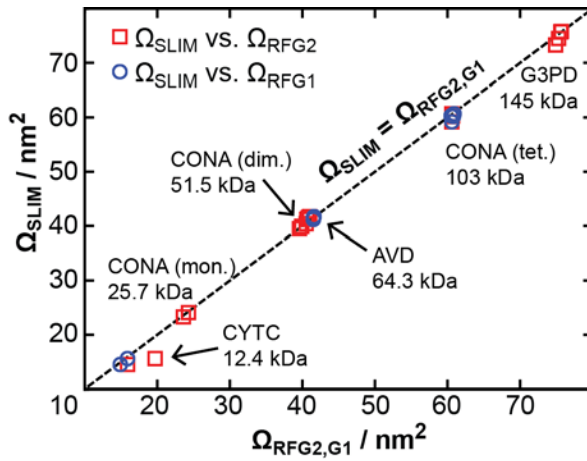
Figure 4.4. Collision cross sections with nitrogen determined here (Ω_{SLIM}) versus those reported using a first-generation RF-confining drift cell (Ω_{RFG1}, *blue circles*)[25] or determined here using a second-generation RF-confining drift cell (Ω_{RFG2}, *red squares*).[27] The dashed line represents a one-to-one relationship between values determined using the two devices ($\Omega_{SLIM} = \Omega_{RFG2/G1}$).

4.4.4 Resolving Powers of Native-Like Ions in SLIM. Resolving power is a useful figure of merit for evaluating the performance of IM instrumentation.[13,15,54–56] The apparent resolving power is calculated by dividing the drift time by the full width at half maximum of the arrival-time distribution ($t_D \Delta t_D^{-1}$); t_D and Δt_D were determined from the Gaussian function that has the smallest residual sum of squares with the experimental distribution. The apparent resolving powers of the arrival-time distributions underlying Figure 4.3B are shown in Figure 4.5 and ranged from 13 to 42, depending on the SLIM drift voltage and analyte. For example, $CYTC^{7+}$ has the lowest apparent resolving power (13) compared to the other analytes studied here, and the apparent resolving power remains constant over the entire SLIM drift voltage range. The 21+ charge state of $CONA^{21+}$ exhibits the highest apparent resolving power (42) of the analytes investigated here, which was observed when using the lowest SLIM drift voltage.

Apparent resolving powers of these native-like ions in nitrogen determined using analogous RF-confining drift cell measurements were calculated by dividing the corrected drift time ($t_D - t_0$) by Δt_D;[27] see the Supporting Information for a discussion of the use of corrected drift time for the RF-confining drift cell measurements. The relatively large standard deviations of the resolving powers for AVD and G3PD may be a result of low signal-to-noise for some replicates and the challenges of using Gaussian functions to estimate Δt_D for structured arrival-time distributions (discussed at the beginning of the *Mobilities of Native-Like Ions* section). Figure 4.5 shows that for these native-like ions, the apparent resolving powers determined using the SLIM instrument are systematically higher than those for the RF-confining drift cell instrument. The origins of those differences are discussed below.
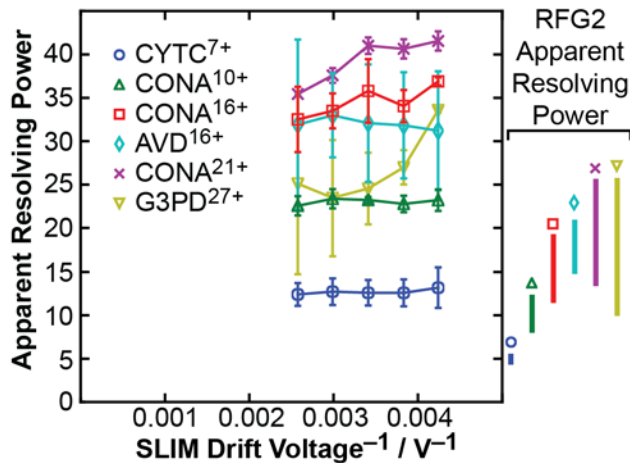
Figure 4.5. Apparent resolving power versus reciprocal SLIM drift voltage plot of selected native-like ions. Values are averages of replicate measurements with error bars representing the standard deviations of those measurements. To the right, the range of apparent resolving powers measured for the same ions using the second-generation RF-confining drift cell (RFG2).

The peak widths of native-like ions measured in SLIM range from 1.5 to 5.0 ms, which are notably broad relative to those expected from diffusion-limited theory:[57]

$$\frac{t_D}{\Delta t_{diff}} = \frac{1}{4} \left(\frac{Vez}{k_B T \ln 2} \right)^{1/2}$$

(4.6)

where Δt_{diff} is the full width at half maximum of the diffusion-limited peak. For example, Equation 4.6 predicts a peak width of ~0.3 ms for G3PD[27+] in 4 Torr nitrogen at a drift voltage of 291 V, whereas experimental peak widths of that ion are ~2.4 ms. Peak widths here contain additional contributions from ion gating (trapping release time of 0.6 ms) and diffusion during transport through the other regions of the instrument, but these factors do not entirely account for the difference observed between Equation 4.6 and experiment. For a given analyte, the lowest apparent resolving powers were most-often measured at the highest drift voltage (385 V); this same trend was seen in measurements made using an RF-confining drift cell and was attributed to contributions to peak widths beyond diffusion.[27] This result is consistent with contributions from ion gating and the presence of an ensemble of conformers, which has been reported previously for protein ions.[27,58–60] The range of apparent resolving powers observed for different native-like ions suggests the presence of ensembles of structures that are unique to each analyte.

The higher apparent resolving powers observed using SLIM relative to those using an RF-confining drift cell are attributed primarily to the longer path length and higher pressure used in the SLIM measurements. The SLIM measurements therefore yield longer t_D that decrease the relative contribution of the trapping release time to the apparent resolving powers. For the SLIM experiments, the trapping release times, total peak widths (Δt_D), and t_D, were 0.6 ms, 1.5 to 5 ms, and 40 to 85 ms, respectively. For the RF-confining drift cell experiments, the trapping release times, Δt_D, and corrected drift times ($t_D - t_0$, see discussion in the Supporting Information), were 0.1 ms, 0.2 to 1.2 ms, and 2.7 to 9.9 ms, respectively. The peak widths of arrival-time

distributions measured using RF-confining drift cells and SLIM both have contributions from trapping release times, but the higher pressures and longer length in the SLIM instrument reduce the relative contribution of trapping release times relative to other sources of broadening, which increase at a lower rate than t_D.

The highest apparent resolving power determined from these experiments (42) is considerably higher than values reported for other native like ions of protein complexes that have been determined directly from experimental data. For example, the highest apparent resolving powers, in terms of the independent variable of the experiment, reported for a native-like ion of a protein or protein complex from traveling-wave ion mobility spectrometry ($t_D \Delta t_D^{-1}$),[55] differential mobility analysis ($V V^{-1}$),[61] and RF-confining drift cells (($t_D - t_0$) Δt_D^{-1})[27] are all around 25. It has been proposed that the resolving powers of traveling-wave ion mobility spectrometry experiments can be evaluated in terms of their Ω distribution after calibration,[9,55] which can yield $\Omega \Delta \Omega^{-1}$ values of up to ~40.[55] However parameters that affect $\Omega \Delta \Omega^{-1}$ also affect the calibrated Ω,[55] which make it challenging to directly compare $\Omega \Delta \Omega^{-1}$ with apparent resolving powers expressed in terms of the independent variable of the experiment.

4.4.5 Retention of Native-Like Ion Structures in SLIM. The similarity between the Ω values determined using these SLIM measurements and analogous measurements made using RF-confining drift cells, which are widely used as standards for native IMMS,[25,27,62,63] suggests that similar ion structures exist in both experiments. Furthermore, all arrival-time distributions are monomodal. In contrast, when the temperature of the stainless steel capillary inlet is raised from 81 °C to 179 °C, the arrival-time distributions of AVD[16+] separated using SLIM broaden and new features appear at longer drift times, which indicates unfolding to non-native conformations (Supporting Information Figure S4.4). This observation is consistent with

collision-induced unfolding of native-like tetramer ions of AVD and CONA, which shows that activation of these ions results in broader arrival-time distributions and the formation of additional structures that have significantly larger Ω values.[64]

The retention of native-like structures suggests that these ions are not significantly activated by SLIM in these experiments. To quantify this, a recently introduced statistical approach,[45] which is described in the *Methods*, was used to estimate the effective temperatures of ions in these experiments. The effective temperatures of AVD[16+] in SLIM containing 4 Torr nitrogen gas at standard ambient temperature (298.15 K) and RF potentials with V_{PP} of 200 V at a frequency of 0.98 MHz were estimated for the five drift field strengths used for the SLIM experiments in this study (1.29 to 2.11 V cm^{-1} Torr^{-1}). Effective temperatures, with a 95% confidence interval, range from 298.6 ± 0.7 to 299.3 ± 0.6 K with increasing drift field strengths. For comparison, analogous estimates for an electrostatic drift cell containing 1.5 Torr of nitrogen gas at standard ambient temperature range from 298.0 ± 0.7 to 298.3 ± 0.6 K over these drift field strengths. The effective temperatures estimated for SLIM, an electrostatic drift cell, and an RF-confining drift cell at each of the five drift field strengths used for the SLIM experiments are reported in Supporting Information Table S4.1. The similarity of all of the effective temperature values suggests the internal energy of the ions in these experiments are only slightly greater than that for ions that are thermalized at ambient temperature.

In addition to the near-ambient effective temperatures suggested by the previous analysis, the presence of nonspecific adducts from the electrospray ionization process may further contribute to the preservation of native-like structures in these experiments. This explanation is consistent with the "freeze-drying" effect of evaporative cooling reported by Beauchamp and

coworkers[65] and with results from collision-induced unfolding indicating the nonspecific adducts preferentially stabilize the native-like structures of protein ions.[64]

4.5 Conclusions

A new hybrid IMMS instrument was used to demonstrate the separation and determination of Ω values for native-like ions of proteins and protein complexes using SLIM with a constant DC gradient along the axis of transmission. The monomodal arrival-time distributions, the magnitude of the Ω values, and near-ambient effective temperatures all suggest that native-like structures are retained in these SLIM experiments. Apparent resolving powers as large as 42 were observed for native-like ions, which is an improvement relative to values determined directly from experimental measurements made using other IM devices (~25).[27,55,61] However, all of these values are lower than expected from diffusion of a single conformer. The differences in the apparent resolving powers observed for different native-like ions is consistent with the arrival-time distributions of those ions have contributions from an ensemble of structures in the gas phase that is unique to each analyte. More broadly, these results suggest that other SLIM technologies, *e.g.* switches[31–33,37] and traps,[34] are adaptable to the analysis of native-like ions. Future experiments will leverage additional SLIM technologies to interrogate the structural diversity and stability of native-like ions of proteins and protein complexes.

4.6 Acknowledgements

4.7 Supporting Information Available

This material is available free of charge via the Internet at http://pubs.acs.org.

Additional instrument details, discussion of corrected drift times, Table S4.1, and Figures S4.1 to S4.4.

4.8 References

(1)   Maurer, M. M.; Donohoe, G. C.; Valentine, S. J. Advances in Ion Mobility-Mass Spectrometry Instrumentation and Techniques for Characterizing Structural Heterogeneity. *Analyst* **2015**, *140* (20), 6782–6798.

(2)   Mason, E. A.; McDaniel, E. W. *Transport Properties of Ions in Gases*, pg. 276.; Wiley: New York, 1988.

(3)   Wyttenbach, T.; Bleiholder, C.; Bowers, M. T. Factors Contributing to the Collision Cross Section of Polyatomic Ions in the Kilodalton to Gigadalton Range: Application to Ion Mobility Measurements. *Anal. Chem.* **2013**, *85* (4), 2191–2199.

(4)   Uetrecht, C.; Barbu, I. M.; Shoemaker, G. K.; van Duijn, E.; Heck, A. J. R. Interrogating Viral Capsid Assembly with Ion Mobility–mass Spectrometry. *Nat. Chem.* **2011**, *3* (2), 126–132.

(5)   Bleiholder, C.; Do, T. D.; Wu, C.; Economou, N. J.; Bernstein, S. S.; Buratto, S. K.; Shea, J.-E.; Bowers, M. T. Ion Mobility Spectrometry Reveals the Mechanism of Amyloid Formation of Aβ(25–35) and Its Modulation by Inhibitors at the Molecular Level: Epigallocatechin Gallate and Scyllo-Inositol. *J. Am. Chem. Soc.* **2013**, *135* (45), 16926–16937.

(6)   Sinha, S.; Du, Z.; Maiti, P.; Klärner, F.-G.; Schrader, T.; Wang, C.; Bitan, G. Comparison of Three Amyloid Assembly Inhibitors: The Sugar Scyllo-Inositol, the Polyphenol Epigallocatechin Gallate, and the Molecular Tweezer CLR01. *ACS Chem. Neurosci.* **2012**, *3* (6), 451–458.

(7)   Hyung, S.-J.; Robinson, C. V.; Ruotolo, B. T. Gas-Phase Unfolding and Disassembly Reveals Stability Differences in Ligand-Bound Multiprotein Complexes. *Chem. Biol.* **2009**, *16* (4), 382–390.

(8)   Ekeowa, U. I.; Freeke, J.; Miranda, E.; Gooptu, B.; Bush, M. F.; Perez, J.; Teckman, J.; Robinson, C. V.; Lomas, D. A. Defining the Mechanism of Polymerization in the Serpinopathies. *Proc. Natl. Acad. Sci. U. S. A.* **2010**, *107* (40), 17146–17151.

(9)   Zhou, M.; Politis, A.; Davies, R. B.; Liko, I.; Wu, K.-J.; Stewart, A. G.; Stock, D.; Robinson, C. V. Ion Mobility–mass Spectrometry of a Rotary ATPase Reveals ATP-Induced Reduction in Conformational Flexibility. *Nat. Chem.* **2014**, *6* (3), 208–215.

(10) Nyon, M. P.; Prentice, T.; Day, J.; Kirkpatrick, J.; Sivalingam, G. N.; Levy, G.; Haq, I.; Irving, J. A.; Lomas, D. A.; Christodoulou, J.; et al. An Integrative Approach Combining Ion Mobility Mass Spectrometry, X-Ray Crystallography, and Nuclear Magnetic Resonance Spectroscopy to Study the Conformational Dynamics of α1-Antitrypsin upon Ligand Binding. *Protein Sci.* **2015**, *24* (8), 1301–1312.

(11) Dugourd, P.; Hudgins, R. R.; Clemmer, D. E.; Jarrold, M. F. High-Resolution Ion Mobility Measurements. *Rev. Sci. Instrum.* **1997**, *68* (2), 1122–1129.

(12) Tang, K.; Shvartsburg, A. A.; Lee, H.-N.; Prior, D. C.; Buschbach, M. A.; Li, F.; Tolmachev, A. V.; Anderson, G. A.; Smith, R. D. High-Sensitivity Ion Mobility Spectrometry/Mass Spectrometry Using Electrodynamic Ion Funnel Interfaces. *Anal. Chem.* **2005**, *77* (10), 3330–3339.

(13) Baker, E. S.; Clowers, B. H.; Li, F.; Tang, K.; Tolmachev, A. V.; Prior, D. C.; Belov, M. E.; Smith, R. D. Ion Mobility Spectrometry–Mass Spectrometry Performance Using Electrodynamic Ion Funnels and Elevated Drift Gas Pressures. *J. Am. Soc. Mass Spectrom.* **2007**, *18* (7), 1176–1187.

(14) McCullough, B. J.; Kalapothakis, J.; Eastwood, H.; Kemper, P.; MacMillan, D.; Taylor, K.; Dorin, J.; Barran, P. E. Development of an Ion Mobility Quadrupole Time of Flight Mass Spectrometer. *Anal. Chem.* **2008**, *80* (16), 6336–6344.

(15) Kemper, P. R.; Dupuis, N. F.; Bowers, M. T. A New, Higher Resolution, Ion Mobility Mass Spectrometer. *Int. J. Mass Spectrom.* **2009**, *287* (1–3), 46–57.

(16) Ibrahim, Y. M.; Baker, E. S.; Danielson III, W. F.; Norheim, R. V.; Prior, D. C.; Anderson, G. A.; Belov, M. E.; Smith, R. D. Development of a New Ion Mobility Time-of-Flight Mass Spectrometer. *Int. J. Mass Spectrom.* **2015**, *377*, 655–662.

(17) Kurulugama, R. T.; Darland, E.; Kuhlmann, F.; Stafford, G.; Fjeldsted, J. Evaluation of Drift Gas Selection in Complex Sample Analyses Using a High Performance Drift Tube Ion Mobility-QTOF Mass Spectrometer. *Analyst* **2015**, *140* (20), 6834–6844.

(18) Shaffer, S. A.; Tolmachev, A.; Prior, D. C.; Anderson, G. A.; Udseth, H. R.; Smith, R. D. Characterization of an Improved Electrodynamic Ion Funnel Interface for Electrospray Ionization Mass Spectrometry. *Anal. Chem.* **1999**, *71* (15), 2957–2964.

(19) Kim, T.; Tolmachev, A. V.; Harkewicz, R.; Prior, D. C.; Anderson, G.; Udseth, H. R.; Smith, R. D.; Bailey, T. H.; Rakov, S.; Futrell, J. H. Design and Implementation of a New Electrodynamic Ion Funnel. *Anal. Chem.* **2000**, *72* (10), 2247–2255.

(20) Tolmachev, A. V.; Kim, T.; Udseth, H. R.; Smith, R. D.; Bailey, T. H.; Futrell, J. H. Simulation-Based Optimization of the Electrodynamic Ion Funnel for High Sensitivity Electrospray Ionization Mass Spectrometry. *Int. J. Mass Spectrom.* **2000**, *203* (1), 31–47.

(21) Javahery, G.; Thomson, B. A Segmented Radiofrequency-Only Quadrupole Collision Cell for Measurements of Ion Collision Cross Section on a Triple Quadrupole Mass Spectrometer. *J. Am. Soc. Mass Spectrom.* **1997**, *8* (7), 697–702.

(22) Guo, Y.; Wang, J.; Javahery, G.; Thomson, B. A.; Siu, K. W. M. Ion Mobility Spectrometer with Radial Collisional Focusing. *Anal. Chem.* **2005**, *77* (1), 266–275.

(23) Giles, K.; Williams, J. P.; Campuzano, I. Enhancements in Travelling Wave Ion Mobility Resolution. *Rapid Commun. Mass Spectrom.* **2011**, *25* (11), 1559–1566.

(24) Zucker, S. M.; Ewing, M. A.; Clemmer, D. E. Gridless Overtone Mobility Spectrometry. *Anal. Chem.* **2013**, *85* (21), 10174–10179.

(25) Bush, M. F.; Hall, Z.; Giles, K.; Hoyes, J.; Robinson, C. V.; Ruotolo, B. T. Collision Cross Sections of Proteins and Their Complexes: A Calibration Framework and Database for Gas-Phase Structural Biology. *Anal. Chem.* **2010**, *82*, 9557–9565.

(26) Allen, S. J.; Schwartz, A. M.; Bush, M. F. Effects of Polarity on the Structures and Charge States of Native-Like Proteins and Protein Complexes in the Gas Phase. *Anal. Chem.* **2013**, *85* (24), 12055–12061.

(27) Allen, S. J.; Giles, K.; Gilbert, T.; Bush, M. F. Ion Mobility Mass Spectrometry of Peptide, Protein, and Protein Complex Ions Using a Radio-Frequency Confining Drift Cell. *Analyst* **2016**, *141*, 884–891.

(28) Silveira, J. A.; Ridgeway, M. E.; Park, M. A. High Resolution Trapped Ion Mobility Spectrometery of Peptides. *Anal. Chem.* **2014**, *86* (12), 5624–5627.

(29) Ruotolo, B. T.; Benesch, J. L. P.; Sandercock, A. M.; Hyung, S.-J.; Robinson, C. V. Ion Mobility–mass Spectrometry Analysis of Large Protein Complexes. *Nat. Protoc.* **2008**, *3* (7), 1139–1152.

(30) Tolmachev, A. V.; Webb, I. K.; Ibrahim, Y. M.; Garimella, S. V. B.; Zhang, X.; Anderson, G. A.; Smith, R. D. Characterization of Ion Dynamics in Structures for Lossless Ion Manipulations. *Anal. Chem.* **2014**, *86* (18), 9162–9168.

(31) Webb, I. K.; Garimella, S. V. B.; Tolmachev, A. V.; Chen, T.-C.; Zhang, X.; Norheim, R. V.; Prost, S. A.; LaMarche, B.; Anderson, G. A.; Ibrahim, Y. M.; et al. Experimental Evaluation and Optimization of Structures for Lossless Ion Manipulations for Ion Mobility Spectrometry with Time-of-Flight Mass Spectrometry. *Anal. Chem.* **2014**, *86* (18), 9169–9176.

(32) Webb, I. K.; Garimella, S. V. B.; Tolmachev, A. V.; Chen, T.-C.; Zhang, X.; Cox, J. T.; Norheim, R. V.; Prost, S. A.; LaMarche, B.; Anderson, G. A.; et al. Mobility-Resolved Ion Selection in Uniform Drift Field Ion Mobility Spectrometry/Mass Spectrometry: Dynamic Switching in Structures for Lossless Ion Manipulations. *Anal. Chem.* **2014**, *86* (19), 9632–9637.

(33) Garimella, S. V. B.; Ibrahim, Y. M.; Webb, I. K.; Tolmachev, A. V.; Zhang, X.; Prost, S. A.; Anderson, G. A.; Smith, R. D. Simulation of Electric Potentials and Ion Motion in Planar Electrode Structures for Lossless Ion Manipulations (SLIM). *J. Am. Soc. Mass Spectrom.* **2014**, *25* (11), 1890–1896.

(34) Zhang, X.; Garimella, S. V. B.; Prost, S. A.; Webb, I. K.; Chen, T.-C.; Tang, K.; Tolmachev, A. V.; Norheim, R. V.; Baker, E. S.; Anderson, G. A.; et al. Ion Trapping, Storage, and Ejection in Structures for Lossless Ion Manipulations. *Anal. Chem.* **2015**, *87* (12), 6010–6016.

(35) Garimella, S. V. B.; Ibrahim, Y. M.; Webb, I. K.; Ipsen, A. B.; Chen, T.-C.; Tolmachev, A. V.; Baker, E. S.; Anderson, G. A.; Smith, R. D. Ion Manipulations in Structures for

Lossless Ion Manipulations (SLIM): Computational Evaluation of a 90° Turn and a Switch. *Analyst* **2015**, *140* (20), 6845–6852.

(36) Hamid, A. M.; Ibrahim, Y. M.; Garimella, S. V. B.; Webb, I. K.; Deng, L.; Chen, T.-C.; Anderson, G. A.; Prost, S. A.; Norheim, R. V.; Tolmachev, A. V.; et al. Characterization of Traveling Wave Ion Mobility Separations in Structures for Lossless Ion Manipulations. *Anal. Chem.* **2015**, *87* (22), 11301–11308.

(37) Chen, T.-C.; Ibrahim, Y. M.; Webb, I. K.; Garimella, S. V. B.; Zhang, X.; Hamid, A. M.; Deng, L.; Karnesky, W. E.; Prost, S. A.; Sandoval, J. A.; et al. Mobility-Selected Ion Trapping and Enrichment Using Structures for Lossless Ion Manipulations. *Anal. Chem.* **2016**, *88* (3), 1728–1733.

(38) Webb, I. K.; Garimella, S. V. B.; Norheim, R. V.; Baker, E. S.; Ibrahim, Y. M.; Smith, R. D. A Structures for Lossless Ion Manipulations (SLIM) Module for Collision Induced Dissociation. *J. Am. Soc. Mass Spectrom.* **2016**, 1–4.

(39) Deng, L.; Ibrahim, Y. M.; Baker, E. S.; Aly, N. A.; Hamid, A. M.; Zhang, X.; Zheng, X.; Garimella, S. V. B.; Webb, I. K.; Prost, S. A.; et al. Ion Mobility Separations of Isomers Based upon Long Path Length Structures for Lossless Ion Manipulations Combined with Mass Spectrometry. *ChemistrySelect* **2016**, *1* (10), 2396–2399.

(40) Giles, K.; Pringle, S. D.; Worthington, K. R.; Little, D.; Wildgoose, J. L.; Bateman, R. H. Applications of a Travelling Wave-Based Radio-Frequency-Only Stacked Ring Ion Guide. *Rapid Commun. Mass Spectrom.* **2004**, *18* (20), 2401–2414.

(41) Hernández, H.; Robinson, C. V. Determining the Stoichiometry and Interactions of Macromolecular Assemblies from Mass Spectrometry. *Nat. Protoc.* **2007**, *2* (3), 715–726.

(42) Chen, T.-C.; Webb, I. K.; Prost, S. A.; Harrer, M. B.; Norheim, R. V.; Tang, K.; Ibrahim, Y. M.; Smith, R. D. Rectangular Ion Funnel: A New Ion Funnel Interface for Structures for Lossless Ion Manipulations. *Anal. Chem.* **2015**, *87* (1), 716–722.

(43) Davidson, K. L.; Oberreit, D. R.; Hogan, C. J.; Bush, M. F. Droplet Sizes, Ionization Currents, and Nonspecific Aggregation in Native Electrokinetic Electrospray Ionization. *Int. J. Mass Spectrom.* **2017**, DOI: 10.1016/j.ijms.2016.09.013.

(44) Clowers, B. H.; Ibrahim, Y. M.; Prior, D. C.; Danielson, W. F.; Belov, M. E.; Smith, R. D. Enhanced Ion Utilization Efficiency Using an Electrodynamic Ion Funnel Trap as an Injection Mechanism for Ion Mobility Spectrometry. *Anal. Chem.* **2008**, *80* (3), 612–623.

(45) Allen, S. J.; Bush, M. F. Radio-Frequency (RF) Confinement in Ion Mobility Mass Spectrometry: Apparent Mobilities and Effective Temperatures. *J. Am. Soc. Mass Spectrom.* **2016**, *27*, 2054–2063.

(46) Dahl, D. SIMION. *SIMION* version 8.1; Idaho National Engineering Laboratory: Idaho Falls, ID.

(47) Marquardt, D. W. An Algorithm for Least-Squares Estimation of Nonlinear Parameters. *J. Appl. Math.* **1963**, *11* (2), 431–441.

(48) van Dongen, W. D.; Heck, A. J. R. Binding of Selected Carbohydrates to Apo-Concanavalin A Studied by Electrospray Ionization Mass Spectrometry. *Analyst* **2000**, *125* (4), 583–589.

(49) Boeri Erba, E.; Barylyuk, K.; Yang, Y.; Zenobi, R. Quantifying Protein–Protein Interactions Within Noncovalent Complexes Using Electrospray Ionization Mass Spectrometry. *Anal. Chem.* **2011**, *83* (24), 9251–9259.

(50) Silveira, J. A.; Jeon, J.; Gamage, C. M.; Pai, P.-J.; Fort, K. L.; Russell, D. H. Damping Factor Links Periodic Focusing and Uniform Field Ion Mobility for Accurate Determination of Collision Cross Sections. *Anal. Chem.* **2012**, *84* (6), 2818–2824.

(51) Bleiholder, C.; Johnson, N. R.; Contreras, S.; Wyttenbach, T.; Bowers, M. T. Molecular Structures and Ion Mobility Cross Sections: Analysis of the Effects of He and N2 Buffer Gas. *Anal. Chem.* **2015**, *87* (14), 7196–7203.

(52) Liu, F. C.; Kirk, S. R.; Bleiholder, C. On the Structural Denaturation of Biological Analytes in Trapped Ion Mobility Spectrometry – Mass Spectrometry. *Analyst* **2016**, *141* (12), 3722–3730.

(53) Hogan, C. J.; Carroll, J. A.; Rohrs, H. W.; Biswas, P.; Gross, M. L. Combined Charged Residue-Field Emission Model of Macromolecular Electrospray Ionization. *Anal. Chem.* **2009**, *81* (1), 369–377.

(54) Merenbloom, S. I.; Glaskin, R. S.; Henson, Z. B.; Clemmer, D. E. High-Resolution Ion Cyclotron Mobility Spectrometry. *Anal. Chem.* **2009**, *81* (4), 1482–1487.

(55) Zhong, Y.; Hyung, S.-J.; Ruotolo, B. T. Characterizing the Resolution and Accuracy of a Second-Generation Traveling-Wave Ion Mobility Separator for Biomolecular Ions. *Analyst* **2011**, *136* (17), 3534–3541.

(56) Davis, E. J.; Grows, K. F.; Siems, W. F.; Hill, H. H. Improved Ion Mobility Resolving Power with Increased Buffer Gas Pressure. *Anal. Chem.* **2012**, *84* (11), 4858–4865.

(57) Revercomb, H. E.; Mason, E. A. Theory of Plasma Chromatography/Gaseous Electrophoresis. Review. *Anal. Chem.* **1975**, *47* (7), 970–983.

(58) Counterman, A. E.; Valentine, S. J.; Srebalus, C. A.; Henderson, S. C.; Hoaglund, C. S.; Clemmer, D. E. High-Order Structure and Dissociation of Gaseous Peptide Aggregates That Are Hidden in Mass Spectra. *J. Am. Soc. Mass Spectrom.* **1998**, *9* (8), 743–759.

(59) Koeniger, S. L.; Merenbloom, S. I.; Clemmer, D. E. Evidence for Many Resolvable Structures within Conformation Types of Electrosprayed Ubiquitin Ions. *J. Phys. Chem. B* **2006**, *110* (13), 7017–7021.

(60) Wyttenbach, T.; Bowers, M. T. Structural Stability from Solution to the Gas Phase: Native Solution Structure of Ubiquitin Survives Analysis in a Solvent-Free Ion Mobility–Mass Spectrometry Environment. *J. Phys. Chem. B* **2011**, *115* (42), 12266–12275.

(61) Fernandez de la Mora, J. High-Resolution Mobility Analysis of Charge-Reduced Electrosprayed Protein Ions. *Anal. Chem.* **2015**, *87* (7), 3729–3735.

(62) Salbo, R.; Bush, M. F.; Naver, H.; Campuzano, I.; Robinson, C. V.; Pettersson, I.; Jørgensen, T. J. D.; Haselmann, K. F. Travelling Wave Ion Mobility Mass Spectrometry: Calibrants and Instrumental Conditions Are Crucial for Correct Collision Cross-Section Measurements. *Rapid Commun. Mass Spectrom.* **2012**, *26*, 1181–1193.

(63) Allison, T. M.; Landreh, M.; Benesch, J. L. P.; Robinson, C. V. Low Charge and Reduced Mobility of Membrane Protein Complexes Has Implications for Calibration of Collision Cross Section Measurements. *Anal. Chem.* **2016**, *88*, 5879–5884.

(64) Freeke, J.; Bush, M. F.; Robinson, C. V.; Ruotolo, B. T. Gas-Phase Protein Assemblies: Unfolding Landscapes and Preserving Native-like Structures Using Noncovalent Adducts. *Chem. Phys. Lett.* **2012**, *524*, 1–9.

(65) Lee, S.-W.; Freivogel, P.; Schindler, T.; Beauchamp, J. L. Freeze-Dried Biomolecules: FT-ICR Studies of the Specific Solvation of Functional Groups and Clathrate Formation Observed by the Slow Evaporation of Water from Hydrated Peptides and Model Compounds in the Gas Phase. *J. Am. Chem. Soc.* **1998**, *120* (45), 11758–11765.

CHAPTER 5

Structural Dynamics of Native-Like Cytochrome *c* Ions in the Gas Phase: Results from

Tandem Ion Mobility

This chapter is reproduced with permission from Allen, S. J.; Eaton, R. M.; Bush, M. F.

"Structural Dynamics of Native-Like Cytochrome *c* Ions in the Gas Phase: Results from Tandem

Ion Mobility" **2017**, manuscript in preparation.

5.1 Abstract

Ion mobility (IM) is a gas-phase separation technique that is widely used to characterize

the shapes and assemblies of protein and protein complex ions. The collision cross sections of

these ions are used in native mass spectrometry to infer structural information and as restraints

for modeling the structures of proteins in solution. Here, we evaluate the stability of native-like

protein ions in the gas phase using tandem IM experiments implemented using Structures for

Lossless Ion Manipulations (SLIM). In this implementation of tandem IM, ions undergo a first

dimension of IM separation up to a switch that is used to selectively transmit ions of a desired

mobility. Selected ions are accumulated in a trap and then released after a delay to initiate the

second dimension of IM separation. Results from tandem IM of native-like, 7+ cytochrome *c*

ions show up to an 8.9% increase in collision cross section for delay times ranging from 16 to

4111 ms, demonstrating that structural isomerization occurs at near-ambient temperatures over

these extended timescales. Subtle increases in collision cross section are observed for

intermediate delay times (81 to 211 ms), which may have implications for other IM experiments

on these timescales. Two subpopulations of the initial, native-like population were each mobility selected and analyzed as a function of delay time. Interestingly, the two subpopulations evolve at different rates to structures that have larger collision cross sections, which suggests that native-like ions retain some memory of their initial gas-phase structures for seconds at ambient temperatures.

5.2 Introduction

The interactions and structures of proteins and protein complexes define the complex biological functions of cells.[1] Whereas the high-resolution structures of proteins can be determined using x-ray crystallography, successful structural determination can be interrupted at each step between purifying the sample and solving the diffraction data.[2] Ion mobility mass spectrometry (IM-MS) has emerged as a powerful, complementary technique for characterizing the structures and assemblies of biological systems. Electrospray ionization of proteins from buffered solutions at biologically relevant pH results in gas-phase ions that retain noncovalent interactions similar to those in solution,[3,4] and are often referred to as "native-like". IM separates ions based on their electrical mobility in a neutral gas (typically 1 to 10 Torr) and is sensitive to the sizes and shapes of ions. The mobility of an ion depends on its charge state and collision cross section (Ω) value which, to the first approximation, depends on the orientationally-averaged projected area of the ion-neutral gas pair.[5,6] IM-MS analysis has been used to characterize numerous biomolecules and bimolecular assemblies, including those that are membrane bound[7–9] and intrinsically disordered.[10,11]

Clemmer and coworkers pioneered the use of IM-IM-MS, which is also called tandem IM, to evaluate the stability and structural diversity of gas-phase ions. Tandem IM measurements

were performed by joining two ~1 m long stacked-ring drift tubes.[12] In this design, a first dimension of IM separation is performed in the first drift tube. The end of the first drift tube contains an ion funnel,[13] which selectively transmits or omits ions depending on their drift time, or mobility. Mobility-selected ions are then transmitted into the second drift tube for a second dimension of IM separation. Seminal work using this instrument showed that the selection of narrow drift time ranges from the broad arrival-time distribution of 7+ ubiquitin yields discrete structures that are stable on the millisecond timescale of the separation.[14] That work and other examples of multidimensional IM,[15–18] IM filtering,[19,20] and high IM resolution[21] provide a growing body of evidence supporting that broad IM distributions are the consequence of ensembles of structures.

The ability to select specific structural subpopulations from broad IM distributions enables other elegant gas-phase structural biology approaches. For example, an IM and infrared spectroscopy approach was used recently to follow the structures of pre-fibrillar assemblies associated with amyloid diseases.[22] Determination of precise structural information for heterogeneous biomolecular assemblies is often limited in traditional condensed-phase techniques that characterize ensemble averages of structures. Mobility selection after IM separation was used to isolate narrow subpopulations of early soluble oligomers of the insulin β-chain fragment, which were subsequently irradiated.[22] The resulting infrared spectra were used to identify specific oligomeric states involved in the transition from unordered to β-sheet structures.

The stability of native-like ion structures within the timescale of most IM-MS experiments remains uncertain. Breuker and McLafferty proposed a timeline for the structural changes of a protein ion after transference from the solution to gas phase, based on meta-analysis of experimental and theoretical results.[23] Following the complete desolvation of a protein ion

after ionization, new ionic bonds form between the desolvated charged residues on the picosecond timescale, according to molecular dynamics simulations.[24] These ionic bonds are capable of holding the native-like structure intact for milliseconds. However, as hydrophobic interactions within the protein are lost, regions of the protein will unfold. Within seconds to minutes, sufficient protein unfolding may occur such that the protein can refold to a more stable gas-phase structure. Evidence of partial unfolding and refolding has been observed for a number of proteins and protein complexes, including ubiquitin[16,25,26] and cytochrome c.[27–29] A detailed understanding of the stability of native-like ions under the conditions and timescales of IM separations is lacking and crucial for advancing native IM-MS.

Here, we investigate the stability of native-like, cytochrome c ions at near-ambient temperature using a recently introduced IM technology, Structures for Lossless Ion Manipulations (SLIM).[30,31] The goal of this work is to characterize the structures of native-like ions in terms of (1) their stability over typical (16 to 211 ms) and extended (4 s) IM timescales and (2) the dynamics of distinct structural subpopulations from the initial ensemble of ions. These investigations are enabled by tandem IM, which is used to select populations of native-like ions and to monitor their structures as a function of residence time under near-ambient temperatures. Results show that the gas-phase conformations of 7+ cytochrome c are not static, but rather, evolve continuously over the millisecond to second timescale. Interestingly, subpopulations of ions with distinct initial mobilities exhibit different rates of isomerization to different Ω distributions, which suggests that the ions retain some memory of their initial gas-phase structures, even after being trapped for over 4 s. More generally, this work provides insights into the dynamics of native-like ions in IM experiments, which is crucial for accurately interpreting the results of native IM-MS experiments.

5.3 Methods

5.3.1 Sample Preparation and Ionization. Cytochrome *c* from equine heart was purchased from Sigma-Aldrich (P/N C2506). Ions were generated using electrokinetic, nanoelectrospray ionization[32] from solutions containing 10 μM cytochrome *c* in 200 mM ammonium acetate at pH 7.0.

5.3.2 Instrumentation. The instrument used for these experiments is similar to that reported previously,[33] but with modifications to enable tandem IM prior to MS as described below. This instrument uses Structures for Lossless Ion Manipulations (SLIM) technology (Figure 5.1a), in which planar electrodes are deposited directly onto printed circuit boards that deliver DC and RF potentials.[30,31,34] Pairs of 7.62 x 7.62 cm SLIM boards, with a 3.97 mm board-to-board distance, form modules that were combined into different arrays to enable additional experiments. Ions from electrospray were introduced into the first vacuum chamber, where they were accumulated in an ion funnel trap.[35] The ion funnel trap injects a packet of ions into the second vacuum chamber, which contains a rectangular ion funnel,[36] six SLIM modules, and a circular ion funnel.[37,38] The first and second chambers were operated at pressures of ~3.99 and ~4.04 Torr nitrogen gas, respectively. The DC electric fields in the post-trapping region of the ion funnel trap, the rectangular ion funnel, the SLIM modules (excluding the orthogonal path described below), and the circular ion funnel were 14, 4, 4, and 8 V cm^{-1}, respectively. IM separated ions were detected using a Waters Q-Tof Premier mass spectrometer and an independent analog-to-digital converter.[33] Additional details of the instrument control and data acquisition are described in the Supporting Information.

5.3.3 Determining Ω Values using SLIM. No traveling waves are used in this implementation of SLIM. Instead, ions are separated using a constant DC gradient, which is analogous to electrostatic drift tubes and RF-confining drift cells.[39] The drift velocity (v_D) of these ions depends on their mobility (K) under an applied electric field (E):

$$v_D = KE \tag{5.1}$$

Voltage-dependent measurements were conducted to determine K values and the transport times outside the SLIM drift region. These results were used to determine Ω values, described by the Mason-Schamp Equation:[5]

$$\Omega = \frac{3ez}{16N} \left(\frac{2\pi}{\mu k_B T} \right)^{1/2} \frac{1}{K} \tag{5.2}$$

where e is the elementary charge, z is the ion charge state, N is the drift-gas number density, μ is the reduced mass of the ion and drift gas, k_B is the Boltzmann constant, and T is the drift-gas temperature (300 K).

5.3.4 Tandem IM. Initially, ions were accumulated and ejected from an ion funnel trap (see Supporting Information for details). Packets of ions pass through three linear modules prior to entering the tee module (position 4, Figure 5.1a), which selects ions with desired drift times, or mobilities. Tee boards contain a linear array of electrodes to transmit ions along a straight path, and an orthogonal array of electrodes to transmit ions that have been diverted from the straight path.[40–43] Mobility filtering is performed by applying DC potentials to two "switch guard" electrodes near the "switch" to the orthogonal path, which were programmed to selectively transmit or divert ions of selected drift times. The straight and orthogonal paths were held at 4 and 8.4 V cm^{-1}, respectively. For all mobility selection experiments, the switch guard voltages were increased by +30 V to divert ions toward the orthogonal path. The time during which the switch guard voltages were held low to transmit ions will be referred to as the

"transmission window". Experiments in which the selected ions were immediately analyzed in the second dimension of IM will be referred to as "selection-only" experiments (Figure 5.1b).
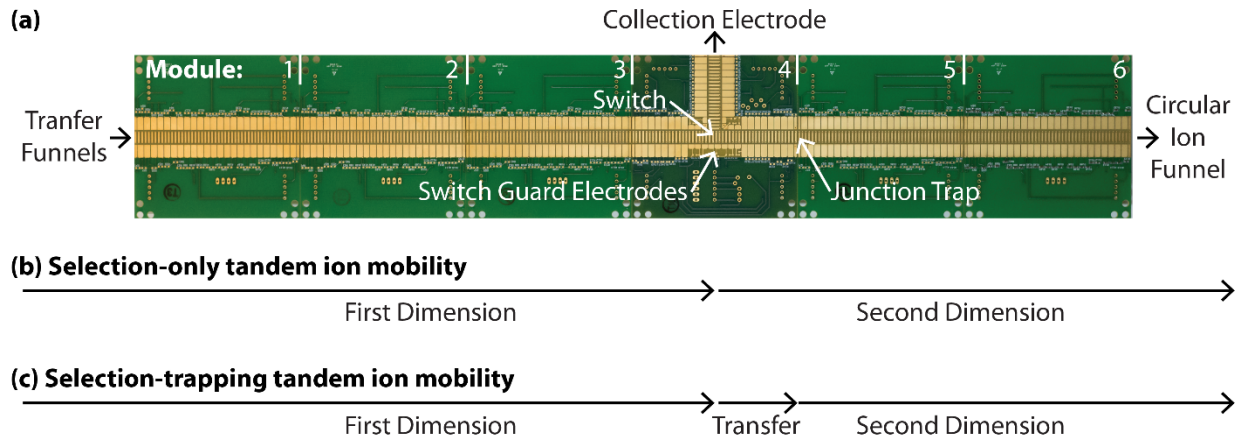
Figure 5.1. (a) Picture of the array of SLIM modules used in these experiments. Ions exiting the transfer funnels (post-trapping region of the ion funnel trap and the rectangular ion funnel) pass through three linear modules (numbered 1 to 3) and a tee module (4). Time-dependent voltages applied to the switch guard electrodes are used to transmit ions entering the switch along the collinear path to the second dimension or divert those ions down the orthogonal path to a collection electrode. A junction trap between modules 4 and 5 is generated by biasing module 5 by +10 V relative to module 4. Ions next pass through two linear modules (5 and 6) and a circular ion funnel before transfer to a Waters Q-Tof Premier mass spectrometer. (b) Selection-only tandem IM experiments consist of a first IM dimension containing the components up to the switch, and a second IM dimension containing the components after the switch. (c) Selection-trapping tandem IM experiments consist of the same first IM dimension, but then

transfer ions to the junction trap. The second IM dimension consists of the

components after the junction trap.

In addition to the selection of specific drift times, packets of transmitted ions can also be

accumulated in the "junction trap" between modules 4 and 5 (Figure 5.1a). Trapping was

performed by biasing the DC voltage of the first electrodes of module 5 by +10 V relative to the

DC voltage of the final electrodes on module 4 (Supporting Information Figure S5.1). The bias

voltage was decreased to release the ion packet from the junction trap and then raised by +10 V

just prior to the next ion packet arriving at the switch. A summary of the trapping parameters and

times are shown in Supporting Information Figure S5.2. Experiments in which selection and

junction trapping were performed will be referred to as "selection-trapping" experiments (Figure

5.1c).

5.3.5 Ion Trajectory Simulations and Effective Temperatures. Ion trajectories of 7+

cytochrome *c* were simulated in SIMION[44] 8.1 using the HS1 hard-sphere approximation for

elastic ion-neutral collisions. The mean free path of 7+ cytochrome *c* was estimated using the Ω

value reported previously.[33] Models of SLIM used 4 Torr nitrogen gas and electrode dimensions

reported previously.[33] The effective translational temperatures of ions were estimated using

results from ion trajectory simulations and a recently introduced statistical approach[39] that is

described in the Supporting Information.

5.3.6 Collision-Induced Unfolding Experiments. Collision-induced unfolding

experiments were performed on a Waters Synapt G2 HDMS in which the traveling-wave ion

mobility cell was replaced with an RF-confining drift cell.[45] Ions were accelerated into the Trap

Cell containing argon gas (3.51×10^{-2} mbar) using varying injection voltages. Drift times were

measured post-activation using the RF-confining drift cell operated at a drift voltage of 138 V in 0.502 Torr nitrogen gas. Drift times were converted to Ω values using results from voltage-dependent measurements[45] and Equation 6.2.

5.4 Results and Discussion

A detailed understanding of the stability and dynamics of native-like ions during IM-MS experiments it critical for advancing native IM-MS and maximizing the information content of those experiments. Towards that end, energy-dependent, single-dimensional IM experiments are used to probe conformational landscape of native-like, 7+ cytochrome c. Time-dependent, tandem IM experiments are then used to probe the dynamics of those ions and isolated subpopulations.

5.4.1 IM-MS of Cytochrome c. Native-like cytochrome c ions were produced from aqueous solutions containing 200 mM ammonium acetate at pH = 7.0 and analyzed using an RF-confining drift cell with a low pressure of nitrogen (0.5 Torr) and injection voltages near the limit of ion transmission. The resulting distribution of Ω with nitrogen of the 7+ ion is shown in Figure 5.2a (4 V trace). The average Ω value of this distribution is 15.3 nm^2, which is similar to a previously reported value (15.9 nm^2) determined using a previous RF-confining drift cell.[46] All Ω values determined in this work were measured with nitrogen gas and, therefore, are systematically larger than those measured with helium gas due to differences in ion-neutral collision integrals and other factors.[46,47] Note that a previous measurement using the current RF-confining drift cell yielded a value of 19.7 nm^2, which was attributed to activation during injection into the drift cell containing a higher pressure of nitrogen gas (1.0 Torr).[33] These results indicate that the current experiments probe compact conformations. Compact Ω values such as

this are representative of "native-like" structures, which can correlate well with Ω values calculated from crystal structures.[48–51]
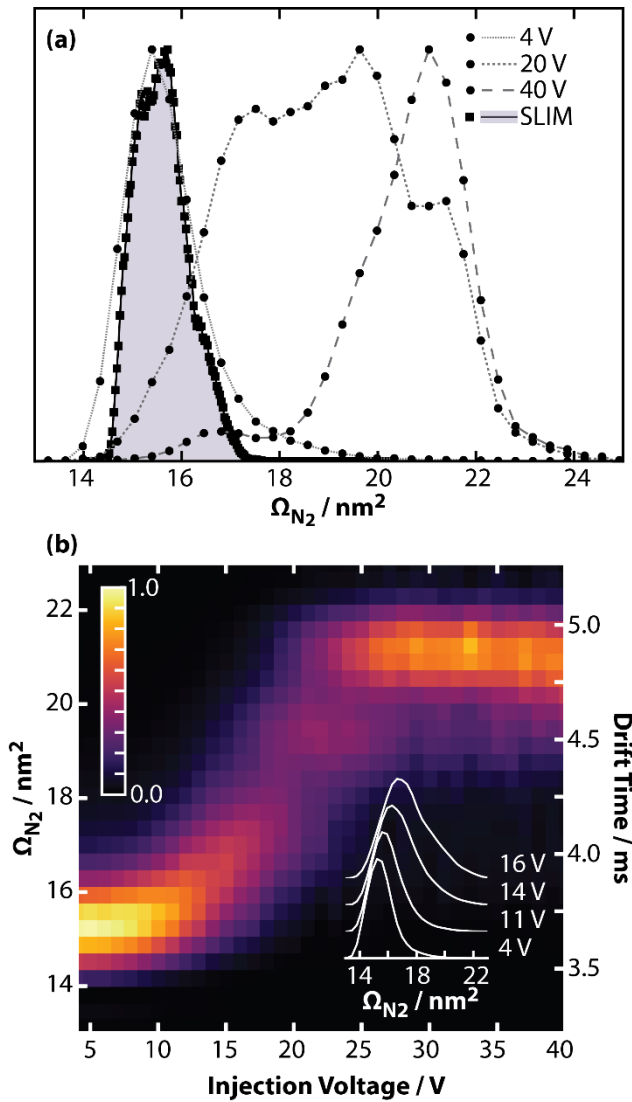
Figure 5.2. Ω distributions of 7+ cytochrome *c* acquired on a Waters Synapt G2 HDMS containing an RF-confining drift cell (circles, grey dashed lines). Three different Ω distributions were acquired at injection voltages of 4, 20, and 40 V into the Trap Cell; the extent of collision-induced unfolding increases with the injection voltage. The Ω distribution acquired using SLIM (squares, shaded

distribution) is also plotted. (b) Heat map of Ω versus injection voltage acquired using the RF-confining drift cell. The inset shows the Ω distributions at injection voltages of 4, 11, 14, and 16 V.

The potential-energy surface of protein ions in the gas phase can be probed using collision-induced unfolding, in which the internal energies of ions are increased through collisional activation with neutral, inert gases prior to re-thermalization. Results from collision-induced unfolding experiments show that it is possible to form stable, unfolded conformations at increasing injection voltages into a collision cell.[52,53] Collision-induced unfolding of 7+ cytochrome c is shown in Figure 5.2b, plotted as a heat map of Ω versus injection voltage. The initial, compact Ω distribution is stable up to an injection voltage of 10 V and then gradually unfolds with increasing injection voltage. At injection voltages of at least 25 V, a distribution centered near ~21 nm^2 remains the dominant feature. The persistence of Ω distributions with increasing energy is consistent with the formation of gas-phase-annealed structures that have reached a quasi-equilibrium.[54] For comparison, the Ω distributions measured at injection voltages of 4, 20, and 40 V are plotted in Figure 5.2a. These distributions show the changes in Ω values resulting from collision-induced unfolding experiments, and serve as a point-of-reference for the tandem IM data discussed later.

An IM separation of 7+ cytochrome c measured here using SLIM is shown in Figure 5.2a (shaded distribution). Recently, SLIM was used to determine the Ω values of native-like protein and protein complex ions.[33] The Ω values determined using SLIM were similar to those determined from other ion mobility devices, but with larger apparent resolving powers. This implementation of SLIM does not use traveling waves; a constant DC gradient is used to

separate ions longitudinally based on Equation 6.1. The apparent Ω distribution measured in

SLIM is similar to that measured in an RF-confining drift cell under low-energy conditions. This

suggests that the native-like ions probed in SLIM and RF-confining drift cells are similar, despite

different electrode geometries, *i.e.*, planar electrodes in SLIM with 3.97 mm gap versus ring

electrodes in an RF-confining drift cell with 7 mm internal diameter. Differences in the widths of

the Ω distributions are primarily due to the longer drift times in SLIM (~80 ms in SLIM versus ~

4 ms in an RF-confining drift cell), which reduces the relative contributions of gating and results

in the higher apparent resolving powers for this SLIM instrument.[33]

5.4.2 IM-IM-MS of Cytochrome *c*. Here, we expand the capabilities of our SLIM

instrument by implementing a module to perform IM-IM-MS (tandem IM) of native-like, 7+

cytochrome *c*. In these tandem IM experiments, native-like ions were selected and trapped as a

function of time to investigate their stability at near-ambient temperature. In the first dimension

of IM, ions were separated as they were transported from the initial trapping region to the switch

(Figure 5.1a). Time-dependent potentials were used to selectively transmit or divert ions, as a

function of their drift times, as they entered the switch. For the initial experiments, a 7.125 ms

transmission window was used to select 7+ cytochrome *c*, and, consequently, divert all other ions

down the orthogonal path to a collection electrode. Next, the transmitted packet of ions was

accumulated in the junction trap between modules 4 and 5 using a bias potential of +10 V

(Supporting Information Figure S5.1). After a delay, ions released from the junction trap undergo

a second dimension of IM separation through two linear modules and a circular ion funnel. These

experiments are representative of selection-trapping tandem IM (Figure 5.1c).

Figure 5.3 (bottom trace) shows tandem IM of 7+ cytochrome *c* using a 16 ms delay

between selection and the second dimension of IM analysis. This is the first demonstration of

tandem IM of a native-like protein ion using SLIM. The exact trapping time of these ions in the junction trap depends on (1) the delay time, which is defined in Supporting Information Figure S5.2a, and (2) the transport time from the switch to the junction trap. The average transport time of 7+ cytochrome c between the switch and the junction trap is ~4.6 ms, which is smaller than the delay times used. For comparison, the Ω distribution determined using a selection-only experiment, in which selected ions undergo separation in the second dimension without junction trapping (Figure 5.1b), is plotted in Figure 5.3 (shaded distribution). The Ω distributions acquired in selection-only experiments and selection-trapping experiments with short delays are similar. That is, ions trapped during short delay times do not undergo resolvable structural changes. The delay time was varied up to 4111 ms, and the resulting Ω distributions determined using selection-trapping experiments are shown in Figure 5.3. The traces in Figure 5.3 show that there is a monotonic increase in the average Ω for delay times from 16 to 4111 ms, with an increase of 8.9% over the entire range of delay times.
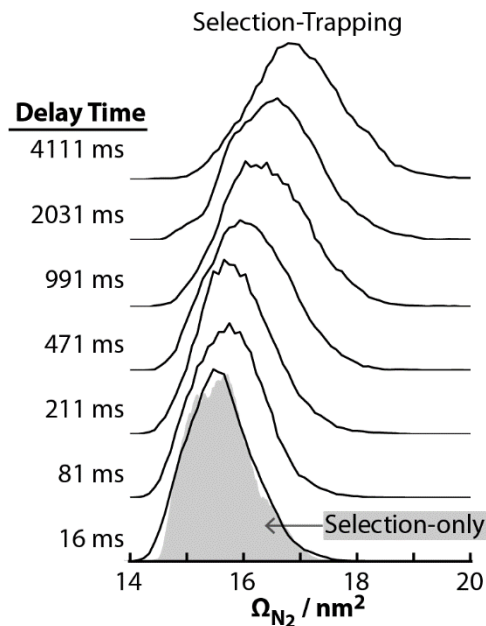
Figure 5.3. Ω distributions of native-like, 7+ cytochrome c determined using selection-trapping experiments with delay times ranging from 16 to 4111 ms. The Ω distribution determined using a selection-only experiment (shaded distribution) is also shown.

Compared to the collision-induced unfolding data shown in Figure 5.2, the change in Ω values in tandem IM experiments (Figure 5.3) is smaller. Interestingly, the results from collision-induced unfolding show a gradual increase in Ω for injection voltages from 10 to 16 V (Figure 5.2b, inset), which is similar in magnitude to the gradual increase in Ω over the full range of delay times. It is difficult though to quantitatively compare the Ω distributions between collision-induced unfolding and tandem IM experiments because of the different independent variables (injection voltage versus delay time). Ions in collision-induced unfolding experiments will achieve far higher internal energies than ions trapped at near-ambient temperature. Therefore, the isomerization pathways accessed in the two methods may be different.

To investigate the internal energy of the ions in these tandem IM experiments, a recently introduced statistical approach[39] and ion trajectory simulations were used to evaluate the effective translational temperatures of ions. Using this method, the effective translational temperature of 7+ cytochrome c in SLIM operated at 4 V cm^{-1} and 4 Torr nitrogen, without junction trapping, is 299.9 K. This temperature is similar to that estimated previously for native-like avidin ions in SLIM (~299 K) using this method,[33] and that calculated for 7+ cytochrome c in an electrostatic drift tube (300.4 K) based on the drift-gas temperature and drift velocity of the ion.[55] Using the statistical approach, the effective translational temperature was estimated for 7+ cytochrome c held in the junction trap with a bias of +10 V and a pre-switch field strength of 4 V

cm^{-1} (Supporting Information Figure S5.3). The effective temperature under those conditions is 308.4 K, which is a subtle increase compared to that for ions not held in the junction trap. Note, the internal energy of the ions also depends on how efficiently energy is converted between the translational and internal degrees of freedom. Therefore, temperatures estimated here are the upper limit of the effective vibrational temperatures of these ions.[39] These results all suggest that the internal energies of the ions in the tandem IM experiments are similar to those expected at ambient temperature.

Charge stripping from 7+ cytochrome *c* was observed at longer delay times, which has also been observed for native-like ions during other long-timescale experiments.[56] Supporting Information Figures S5.4a and S5.4b show mass spectra of 7+ and 6+ charge states, respectively, at the shortest and longest delay times. At the shortest delay time, some 6+ (~1% relative abundance) is detected due to charge stripping that occurs after the second dimension of IM. At the longest delay time, the 7+ ion abundance decreases as 6+ ions are formed by charge stripping during junction trapping (~5% relative abundance). A summary of the 7+, 6+, and combined ion abundance are shown in Supporting Information Figure S5.4c. The combined ion abundance stays constant for delay times up to 211 ms, showing that there are minimal ion losses over those timescales. At longer delay times, a decrease in the combined ion abundance is observed, which may be due to inefficient electrodynamic trapping or secondary consequences of charge stripping; the charge-reduced products will be trapped[57] and detected[58] with lower efficiency than the precursors.

5.4.3 Comparisons to Other Experiments. Clemmer and coworkers previously observed increases in Ω for ions that were held in a Paul Trap (10^{-3} to 10^{-4} Torr He) as a function of time prior to IM-MS analysis.[25,29,59] Most relevant to the results from this work, the arrival-

time distributions of 7+ cytochrome *c* (produced from 49/49/2 water/methanol/acetic acid solutions) were measured for trapping times up to 71 ms.[59] At trapping times greater than ~31 ms, the abundance of the compact distribution decreases and unresolved features at longer drift times increase in abundance up to a 71 ms trapping time. The subtle increase in Ω observed in Clemmer and coworkers' study appears to be consistent with the shift in Ω distribution observed between delay times of 16 to 81 ms shown in Figure 5.3. Later, the Paul Trap/IM technique was used to measure arrival-time distributions of 7+ cytochrome *c* up to 10 s, but the distributions were not reported and the authors only note that unfolding transitions were observed over those longer trapping times.[29] Nonetheless, the similarity between the results of both experiments are striking, especially considering the different solution conditions (denaturing versus native-like) and trapping conditions (trapping in a Paul Trap versus in SLIM). This comparison may further corroborate the absolute timescales and corresponding structural dynamics outlined by Breuker and McLafferty.[23]

5.4.4 Structural Evolution of Selected Subpopulations. The apparent Ω distribution of native-like, 7+ cytochrome *c* ions determined using a selection-only experiment (no junction trapping) is shown in Figure 5.4a. This distribution (population I) is broad compared to the diffusion-limited[60] width at base expected for a single structure under these conditions (0.45 nm^2), which is consistent with population I containing of an ensemble of structures.[14,45,61] Two subpopulations from the initial population were individually selected at the switch using transmission windows of 1.125 ms that differed in absolute time by 2.25 ms (Figure 5.4a). Subpopulation II spans a range of more compact Ω values than subpopulation III. The traces in Figure 5.4a show that subpopulations of native-like ions with different Ω distributions are stable on the timescale of the second IM dimension (~28 ms). Clemmer and coworkers used selection-

only experiments, which were implemented using a very different instrument geometry that is described in the *Introduction*, to probe subpopulations of protein ions generated from denaturing solutions. Those foundational experiments demonstrated that the structural subpopulations from the full ensemble were each stable on the timescale of those separations (8 to 12 ms),[14] which established that structural differences within the initial ensembles contributed greatly to the observed Ω distributions. Results from the experiments in this work, which probe native-like ions, are consistent with that interpretation.

In addition to selection-only experiments, the instrument used in this work enables tandem IM experiments that can trap ions for an arbitrary period of at least 4 s. The ability to select, trap, and analyze subpopulations (selection-trapping, Figure 5.1b), without transferring ions between instrument components operated at different pressures, enables a novel approach to evaluate the time-dependent dynamics of different structural subpopulations at near-ambient temperatures. Using the same transmission windows used to acquire the data in Figure 5.4a, the apparent Ω distributions resulting from selection-trapping experiments with a delay time of 16 ms are shown in Figure 5.4b. Note that there is a 64.5 ms delay between the beginning of the first dimension and the beginning of the second dimension for the analysis of the initial population (I) and both subpopulations (II and III), as depicted in Supporting Information Figure S5.2. The actual time differences between ion selection and the beginning of the second dimension are slightly different (up to 2 ms) in the three experiments and depend on the mobilities of the ions that are selected. For simplicity, a common delay time (Supporting Information Figure S5.2) is reported for experiments probing the three populations. Also note that the distributions resulting from selection-trapping experiments (Figure 5.4b) are broader than those from selection-only

experiments (Figure 5.4a); the origin of this difference will be the subject of a future investigation.
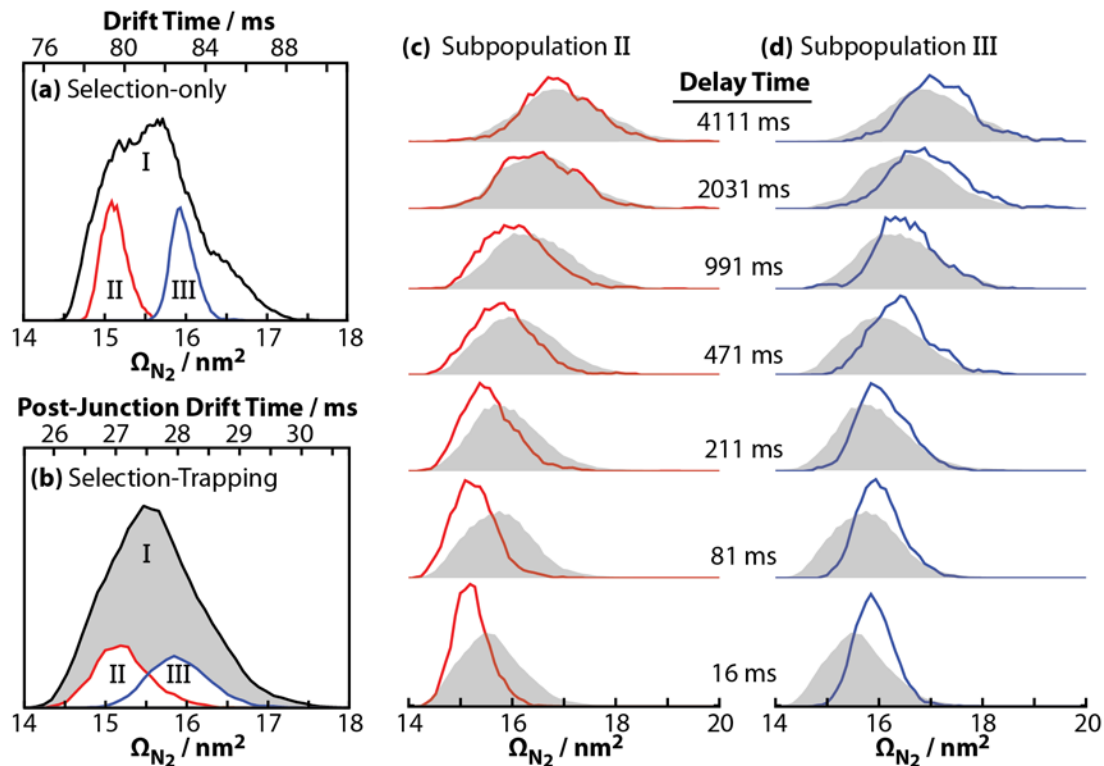
Figure 5.4. (a) Ω distributions of native-like, 7+ cytochrome c plotted using the absolute intensity determined from selection-only experiments. Transmission windows of 7.125 and 1.125 ms were used to select the entire population (I) or subpopulations (II and III), respectively. (b) Ω distributions using the absolute intensity determined from selection-trapping experiments (16 ms delay time) and

the same transmission windows used in part a. The drift time after release of ions from the junction trap is provided on the top axis. (c) Ω distributions determined using selection-trapping experiments of subpopulation II (red trace) for delay times ranging from 16 to 4111 ms. (d) Ω distributions determined using selection-trapping experiments of subpopulation III (blue trace) for delay times ranging from 16 to 4111 ms. For each delay time in parts c and d, the corresponding distribution resulting from population I is also plotted (shaded distribution). All distributions in c and d are normalized to an integral of one.

Figures 5.4c and 5.4d show results from selection-trapping analysis of subpopulations II and III, respectively, as a function of the delay time between the first and second IM dimension. Similar to the results for population I, subpopulations II and III exhibit a gradual increase in apparent Ω values with increasing delay times. Interestingly, even after a delay time of 4111 ms, subpopulations II and III exhibit different Ω distributions from each other and from the original, broad population. Figure 5.5 shows a summary of the three populations (I, II, and III) as a function of delay time between the first and second IM dimension. Because not all Ω distributions are Gaussian-like in shape, critical values from the cumulative distribution functions (CDF) were used to represent the distributions, as illustrated in Supporting Information Figure S5.5. Briefly, the CDF is the probability of the distribution's density, *e.g.*, the Ω at which the CDF has a value of 50% corresponds to the center of the density of the Ω distribution. The markers in Figure 5.5 correspond to that critical value for each Ω distribution. The width of each Ω distribution is represented by a bar that extends from 5% to 95% of the corresponding CDF. Figure 5.5 shows that the three distributions all increase to larger Ω values with increasing delay

time, but that even after 4 s, the Ω distributions of I, II, and III are still different. Specifically, at the longest delay time, the more compact initial subpopulation (II) still spans a more compact range of apparent Ω values than that originating from the less compact initial subpopulation (III). Supporting Information Figure S5.6 shows the Ω distributions for all three distributions at the shortest (16 ms) and longest (4111 ms) delay times to emphasize their differences.
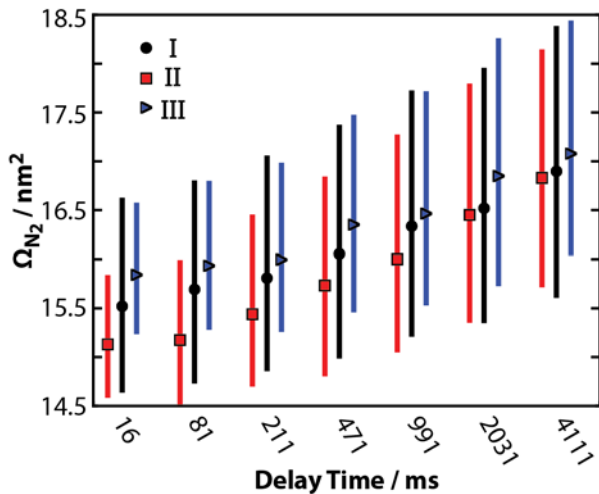
Figure 5.5. (a) Summary of critical Ω values of distributions I, II, and III for delay times ranging from 16 to 4111 ms. Using a CDF analysis (Supporting Information Figure S5.5), the 50% critical Ω values of distributions I (black circles), II (red squares), and III (blue triangles) are plotted with bars that span from 5% to 95% of the CDF.

More generally, Figure 5.5 shows that 7+ cytochrome *c* ions undergo structural isomerization on the millisecond to seconds timescale, and that the rate of isomerization and the population of structural isomers depend on the initial selections of mobilities. At longer delay times, the Ω distributions of the subpopulations broaden and become increasingly similar to that

originating from the original, full population, but even after 4 s, the two subpopulations exhibit different Ω distributions. This suggests that native-like ions can retain some memory of their initial gas-phase structures for seconds at a near-ambient temperature.

5.5 Conclusions

Using tandem IM, the stability of native-like, 7+ cytochrome c held at near-ambient temperature was monitored as a function of time. The Ω distributions of these ions evolve and increase by 8.9% for delay times ranging from 16 to 4111 ms (Figure 5.3). The isolation of ions of selected mobilities from broad, native-like distributions enables experiments that probe the isomerization of structural subpopulations. The Ω distributions for two subpopulations of native-like, 7+ cytochrome c were analyzed as a function of delay time (Figure 5.4c and 5.4d). Comparison of those distributions (Figure 5.5) shows that the structures of different subpopulations evolve at different rates. Remarkably, even after being held for 4111 ms at near-ambient temperature, the subpopulations exhibit different ranges of apparent Ω values, which suggests that these ions still retain some memory of differences in their initial gas-phase structures.

The structural transitions and range of apparent Ω values observed in tandem IM experiments are different than those observed in collision-induced unfolding experiments (Figure 5.2). Specifically, the average Ω value of 7+ cytochrome c ions in tandem IM experiments is ~17 nm^2 after 4111 ms, which is smaller than that for the gas-phase annealed structures observed at high injection voltages in collision-induced unfolding experiments (~21 nm^2). The data in Figure 5.5 also show that native-like ions evolve on the tens of milliseconds timescale, which is

comparable to the timescale of many IM separations.[21,62,63] Although the increase in Ω value between delay times of 16 to 211 ms is only ~2%, this increase is comparable to the uncertainties reported for several IM instruments used for structural applications.[45,62,64] Thus, these structural transitions likely occur during other IM experiments, but would be very difficult to isolate in a single-dimensional IM analysis. More generally, the results presented her provide evidence for the structural evolution of gas-phase ions on the milliseconds to seconds timescale, which complements other examples of gas-phase ions showing structural dynamics on the picoseconds,[24,65] seconds,[25,29] or minutes to hours[66,67] timescale. Understanding the dynamics of gas-phase ions will enable future gas-phase structural biology approaches to further characterize the structures of biomolecules in solution.

5.6 Acknowledgements

5.7 Supporting Information Available

This material is available free of charge via the Internet at http://pubs.acs.org.

Additional instrument details, effective temperature statistical analysis, and Figures S5.1 to S5.6.

5.8 References

(1)   Marsh, J. A.; Teichmann, S. A. Structure, Dynamics, Assembly, and Evolution of Protein Complexes. *Annu. Rev. Biochem.* **2015**, *84* (1), 551–575.

(2)   Stacy, R.; Begley, D. W.; Phan, I.; Staker, B. L.; Van Voorhis, W. C.; Varani, G.; Buchko, G. W.; Stewart, L. J.; Myler, P. J. Structural Genomics of Infectious Disease Drug Targets: The SSGCID. *Acta Cryst. Sect. F* **2011**, *67* (9), 979–984.

(3)   Benesch, J. L. P.; Ruotolo, B. T.; Simmons, D. A.; Robinson, C. V. Protein Complexes in the Gas Phase: Technology for Structural Genomics and Proteomics. *Chem. Rev.* **2007**, *107* (8), 3544–3567.

(4)   Leney, A. C.; Heck, A. J. R. Native Mass Spectrometry: What Is in the Name? *J. Am. Soc. Mass Spectrom.* **2017**, *28* (1), 5–13.

(5)   Mason, E. A.; McDaniel, E. W. *Transport Properties of Ions in Gases*, pg. 276.; Wiley: New York, 1988.

(6)   Wyttenbach, T.; Bleiholder, C.; Bowers, M. T. Factors Contributing to the Collision Cross Section of Polyatomic Ions in the Kilodalton to Gigadalton Range: Application to Ion Mobility Measurements. *Anal. Chem.* **2013**, *85* (4), 2191–2199.

(7)   Zhou, M.; Morgner, N.; Barrera, N. P.; Politis, A.; Isaacson, S. C.; Matak-Vinković, D.; Murata, T.; Bernal, R. A.; Stock, D.; Robinson, C. V. Mass Spectrometry of Intact V-Type ATPases Reveals Bound Lipids and the Effects of Nucleotide Binding. *Science* **2011**, *334* (6054), 380–385.

(8)   Zhou, M.; Politis, A.; Davies, R. B.; Liko, I.; Wu, K.-J.; Stewart, A. G.; Stock, D.; Robinson, C. V. Ion Mobility–mass Spectrometry of a Rotary ATPase Reveals ATP-Induced Reduction in Conformational Flexibility. *Nat. Chem.* **2014**, *6* (3), 208–215.

(9)   Laganowsky, A.; Reading, E.; Allison, T. M.; Ulmschneider, M. B.; Degiacomi, M. T.; Baldwin, A. J.; Robinson, C. V. Membrane Proteins Bind Lipids Selectively to Modulate Their Structure and Function. *Nature* **2014**, *510* (7503), 172–175.

(10)   Pagel, K.; Natan, E.; Hall, Z.; Fersht, A. R.; Robinson, C. V. Intrinsically Disordered p53 and Its Complexes Populate Compact Conformations in the Gas Phase. *Angew. Chem. Int. Ed.* **2013**, *52* (1), 361–365.

(11)   Jurneczko, E.; Cruickshank, F.; Porrini, M.; Clarke, D. J.; Campuzano, I. D. G.; Morris, M.; Nikolova, P. V.; Barran, P. E. Probing the Conformational Diversity of Cancer-Associated Mutations in p53 with Ion-Mobility Mass Spectrometry. *Angew. Chem. Int. Ed.* **2013**, *52* (16), 4370–4374.

(12)   Koeniger, S. L.; Merenbloom, S. I.; Valentine, S. J.; Jarrold, M. F.; Udseth, H. R.; Smith, R. D.; Clemmer, D. E. An IMS−IMS Analogue of MS−MS. *Anal. Chem.* **2006**, *78* (12), 4161–4174.

(13)   Tang, K.; Shvartsburg, A. A.; Lee, H.-N.; Prior, D. C.; Buschbach, M. A.; Li, F.; Tolmachev, A. V.; Anderson, G. A.; Smith, R. D. High-Sensitivity Ion Mobility Spectrometry/Mass Spectrometry Using Electrodynamic Ion Funnel Interfaces. *Anal. Chem.* **2005**, *77* (10), 3330–3339.

(14)   Koeniger, S. L.; Merenbloom, S. I.; Clemmer, D. E. Evidence for Many Resolvable Structures within Conformation Types of Electrosprayed Ubiquitin Ions. *J. Phys. Chem. B* **2006**, *110* (13), 7017–7021.

(15) Merenbloom, S. I.; Koeniger, S. L.; Valentine, S. J.; Plasencia, M. D.; Clemmer, D. E. IMS−IMS and IMS−IMS−IMS/MS for Separating Peptide and Protein Fragment Ions. *Anal. Chem.* **2006**, *78* (8), 2802–2809.

(16) Koeniger, S. L.; Clemmer, D. E. Resolution and Structural Transitions of Elongated States of Ubiquitin. *J. Am. Soc. Mass Spectrom.* **2007**, *18* (2), 322–331.

(17) Simon, A.-L.; Chirot, F.; Choi, C. M.; Clavier, C.; Barbaire, M.; Maurelli, J.; Dagany, X.; MacAleese, L.; Dugourd, P. Tandem Ion Mobility Spectrometry Coupled to Laser Excitation. *Rev. Sci. Instrum.* **2015**, *86* (9), 094101.

(18) Jacobs, A. D.; Eschweiler, J. D.; Dixit, S.; Ruotolo, B. T.; Clemmer, D. E. Structural Transitions of Bovine Serum Albumin Studied by IMS-IMS-MS. *64th Conference on Mass Spectrometry and Allied Topics* **2016**, *San Antonio*, *TX*, TP 495.

(19) Kurulugama, R. T.; Nachtigall, F. M.; Lee, S.; Valentine, S. J.; Clemmer, D. E. Overtone Mobility Spectrometry: Part 1. Experimental Observations. *J. Am. Soc. Mass Spectrom.* **2009**, *20* (5), 729–737.

(20) Zucker, S. M.; Ewing, M. A.; Clemmer, D. E. Gridless Overtone Mobility Spectrometry. *Anal. Chem.* **2013**, *85* (21), 10174–10179.

(21) Merenbloom, S. I.; Glaskin, R. S.; Henson, Z. B.; Clemmer, D. E. High-Resolution Ion Cyclotron Mobility Spectrometry. *Anal. Chem.* **2009**, *81* (4), 1482–1487.

(22) Seo, J.; Hoffmann, W.; Warnke, S.; Huang, X.; Gewinner, S.; Schöllkopf, W.; Bowers, M. T.; von Helden, G.; Pagel, K. An Infrared Spectroscopy Approach to Follow β-Sheet Formation in Peptide Amyloid Assemblies. *Nat Chem* **2017**, *9* (1), 39–44.

(23) Breuker, K.; McLafferty, F. W. Stepwise Evolution of Protein Native Structure with Electrospray into the Gas Phase, 10−12 to 102 S. *Proc. Natl. Acad. Sci. U. S. A.* **2008**, *105* (47), 18145–18152.

(24) Steinberg, M. Z.; Elber, R.; McLafferty, F. W.; Gerber, R. B.; Breuker, K. Early Structural Evolution of Native Cytochrome c after Solvent Removal. *ChemBioChem* **2008**, *9* (15), 2417–2423.

(25) Myung, S.; Badman, E. R.; Lee, Y. J.; Clemmer, D. E. Structural Transitions of Electrosprayed Ubiquitin Ions Stored in an Ion Trap over ~10 Ms to 30 S. *J. Phys. Chem. A* **2002**, *106* (42), 9976–9982.

(26) Skinner, O. S.; McLafferty, F. W.; Breuker, K. How Ubiquitin Unfolds after Transfer into the Gas Phase. *J. Am. Soc. Mass Spectrom.* **2012**, *23* (6), 1011–1014.

(27) Breuker, K.; McLafferty, F. W. Native Electron Capture Dissociation for the Structural Characterization of Noncovalent Interactions in Native Cytochrome c. *Angew. Chem. Int. Ed.* **2003**, *42* (40), 4900–4904.

(28) Breuker, K.; McLafferty, F. W. The Thermal Unfolding of Native Cytochrome c in the Transition from Solution to Gas Phase Probed by Native Electron Capture Dissociation. *Angew. Chem. Int. Ed.* **2005**, *44* (31), 4911–4914.

(29) Badman, E. R.; Myung, S.; Clemmer, D. E. Evidence for Unfolding and Refolding of Gas-Phase Cytochrome c Ions in a Paul Trap. *J. Am. Soc. Mass Spectrom.* **2005**, *16* (9), 1493–1497.

(30) Tolmachev, A. V.; Webb, I. K.; Ibrahim, Y. M.; Garimella, S. V. B.; Zhang, X.; Anderson, G. A.; Smith, R. D. Characterization of Ion Dynamics in Structures for Lossless Ion Manipulations. *Anal. Chem.* **2014**, *86* (18), 9162–9168.

(31) Webb, I. K.; Garimella, S. V. B.; Tolmachev, A. V.; Chen, T.-C.; Zhang, X.; Norheim, R. V.; Prost, S. A.; LaMarche, B.; Anderson, G. A.; Ibrahim, Y. M.; et al. Experimental

Evaluation and Optimization of Structures for Lossless Ion Manipulations for Ion Mobility Spectrometry with Time-of-Flight Mass Spectrometry. *Anal. Chem.* **2014**, *86* (18), 9169–9176.

(32)   Davidson, K. L.; Oberreit, D. R.; Hogan, C. J.; Bush, M. F. Droplet Sizes, Ionization Currents, and Nonspecific Aggregation in Native Electrokinetic Electrospray Ionization. *Int. J. Mass Spectrom.* **2017**, DOI: 10.1016/j.ijms.2016.09.013.

(33)   Allen, S. J.; Eaton, R. M.; Bush, M. F. Analysis of Native-Like Ions Using Structures for Lossless Ion Manipulations. *Anal. Chem.* **2016**, *88* (18), 9118–9126.

(34)   Garimella, S. V. B.; Ibrahim, Y. M.; Webb, I. K.; Tolmachev, A. V.; Zhang, X.; Prost, S. A.; Anderson, G. A.; Smith, R. D. Simulation of Electric Potentials and Ion Motion in Planar Electrode Structures for Lossless Ion Manipulations (SLIM). *J. Am. Soc. Mass Spectrom.* **2014**, *25* (11), 1890–1896.

(35)   Clowers, B. H.; Ibrahim, Y. M.; Prior, D. C.; Danielson, W. F.; Belov, M. E.; Smith, R. D. Enhanced Ion Utilization Efficiency Using an Electrodynamic Ion Funnel Trap as an Injection Mechanism for Ion Mobility Spectrometry. *Anal. Chem.* **2008**, *80* (3), 612–623.

(36)   Chen, T.-C.; Webb, I. K.; Prost, S. A.; Harrer, M. B.; Norheim, R. V.; Tang, K.; Ibrahim, Y. M.; Smith, R. D. Rectangular Ion Funnel: A New Ion Funnel Interface for Structures for Lossless Ion Manipulations. *Anal. Chem.* **2015**, *87* (1), 716–722.

(37)   Shaffer, S. A.; Tolmachev, A.; Prior, D. C.; Anderson, G. A.; Udseth, H. R.; Smith, R. D. Characterization of an Improved Electrodynamic Ion Funnel Interface for Electrospray Ionization Mass Spectrometry. *Anal. Chem.* **1999**, *71* (15), 2957–2964.

(38)   Ibrahim, Y. M.; Baker, E. S.; Danielson III, W. F.; Norheim, R. V.; Prior, D. C.; Anderson, G. A.; Belov, M. E.; Smith, R. D. Development of a New Ion Mobility Time-of-Flight Mass Spectrometer. *Int. J. Mass Spectrom.* **2015**, *377*, 655–662.

(39)   Allen, S. J.; Bush, M. F. Radio-Frequency (RF) Confinement in Ion Mobility Mass Spectrometry: Apparent Mobilities and Effective Temperatures. *J. Am. Soc. Mass Spectrom.* **2016**, *27*, 2054–2063.

(40)   Webb, I. K.; Garimella, S. V. B.; Tolmachev, A. V.; Chen, T.-C.; Zhang, X.; Cox, J. T.; Norheim, R. V.; Prost, S. A.; LaMarche, B.; Anderson, G. A.; et al. Mobility-Resolved Ion Selection in Uniform Drift Field Ion Mobility Spectrometry/Mass Spectrometry: Dynamic Switching in Structures for Lossless Ion Manipulations. *Anal. Chem.* **2014**, *86* (19), 9632–9637.

(41)   Garimella, S. V. B.; Ibrahim, Y. M.; Webb, I. K.; Ipsen, A. B.; Chen, T.-C.; Tolmachev, A. V.; Baker, E. S.; Anderson, G. A.; Smith, R. D. Ion Manipulations in Structures for Lossless Ion Manipulations (SLIM): Computational Evaluation of a 90° Turn and a Switch. *Analyst* **2015**, *140* (20), 6845–6852.

(42)   Zhang, X.; Garimella, S. V. B.; Prost, S. A.; Webb, I. K.; Chen, T.-C.; Tang, K.; Tolmachev, A. V.; Norheim, R. V.; Baker, E. S.; Anderson, G. A.; et al. Ion Trapping, Storage, and Ejection in Structures for Lossless Ion Manipulations. *Anal. Chem.* **2015**, *87* (12), 6010–6016.

(43)   Chen, T.-C.; Ibrahim, Y. M.; Webb, I. K.; Garimella, S. V. B.; Zhang, X.; Hamid, A. M.; Deng, L.; Karnesky, W. E.; Prost, S. A.; Sandoval, J. A.; et al. Mobility-Selected Ion Trapping and Enrichment Using Structures for Lossless Ion Manipulations. *Anal. Chem.* **2016**, *88* (3), 1728–1733.

(44)   Dahl, D. SIMION. *SIMION* version 8.1; Idaho National Engineering Laboratory: Idaho Falls, ID.

(45) Allen, S. J.; Giles, K.; Gilbert, T.; Bush, M. F. Ion Mobility Mass Spectrometry of Peptide, Protein, and Protein Complex Ions Using a Radio-Frequency Confining Drift Cell. *Analyst* **2016**, *141*, 884–891.

(46) Bush, M. F.; Hall, Z.; Giles, K.; Hoyes, J.; Robinson, C. V.; Ruotolo, B. T. Collision Cross Sections of Proteins and Their Complexes: A Calibration Framework and Database for Gas-Phase Structural Biology. *Anal. Chem.* **2010**, *82*, 9557–9565.

(47) Bleiholder, C.; Johnson, N. R.; Contreras, S.; Wyttenbach, T.; Bowers, M. T. Molecular Structures and Ion Mobility Cross Sections: Analysis of the Effects of He and N2 Buffer Gas. *Anal. Chem.* **2015**, *87* (14), 7196–7203.

(48) Ruotolo, B. T.; Giles, K.; Campuzano, I.; Sandercock, A. M.; Bateman, R. H.; Robinson, C. V. Evidence for Macromolecular Protein Rings in the Absence of Bulk Water. *Science* **2005**, *310* (5754), 1658–1661.

(49) Jurneczko, E.; Barran, P. E. How Useful Is Ion Mobility Mass Spectrometry for Structural Biology? The Relationship between Protein Crystal Structures and Their Collision Cross Sections in the Gas Phase. *Analyst* **2010**, *136* (1), 20–28.

(50) Bereszczak, J. Z.; Barbu, I. M.; Tan, M.; Xia, M.; Jiang, X.; van Duijn, E.; Heck, A. J. R. Structure, Stability and Dynamics of Norovirus P Domain Derived Protein Complexes Studied by Native Mass Spectrometry. *J. Struct. Biol.* **2012**, *177* (2), 273–282.

(51) Hall, Z.; Politis, A.; Robinson, C. V. Structural Modeling of Heteromeric Protein Complexes from Disassembly Pathways and Ion Mobility-Mass Spectrometry. *Structure* **2012**, *20* (9), 1596–1609.

(52) Ruotolo, B. T.; Hyung, S.-J.; Robinson, P. M.; Giles, K.; Bateman, R. H.; Robinson, C. V. Ion Mobility–Mass Spectrometry Reveals Long-Lived, Unfolded Intermediates in the Dissociation of Protein Complexes. *Angew. Chem. Int. Ed.* **2007**, *46* (42), 8001–8004.

(53) Freeke, J.; Bush, M. F.; Robinson, C. V.; Ruotolo, B. T. Gas-Phase Protein Assemblies: Unfolding Landscapes and Preserving Native-like Structures Using Noncovalent Adducts. *Chem. Phys. Lett.* **2012**, *524*, 1–9.

(54) Pierson, N. A.; Valentine, S. J.; Clemmer, D. E. Evidence for a Quasi-Equilibrium Distribution of States for Bradykinin [M + 3H]3+ Ions in the Gas Phase. *J. Phys. Chem. B* **2010**, *114* (23), 7777–7783.

(55) Mason, E. A.; McDaniel, E. W. *Transport Properties of Ions in Gases*, pg. 149.; Wiley: New York, 1988.

(56) Harvey, S. R.; Yan, J.; Brown, J. M.; Hoyes, E.; Wysocki, V. H. Extended Gas-Phase Trapping Followed by Surface-Induced Dissociation of Noncovalent Protein Complexes. *Anal. Chem.* **2016**, *88* (2), 1218–1221.

(57) Tolmachev, A. V.; Chernushevich, I. V.; Dodonov, A. F.; Standing, K. G. A Collisional Focusing Ion Guide for Coupling an Atmospheric Pressure Ion Source to a Mass Spectrometer. *Nucl. Instrum. Methods Phys. Res. B* **1997**, *124* (1), 112–119.

(58) Chen, X.; Westphall, M. S.; Smith, L. M. Mass Spectrometric Analysis of DNA Mixtures: Instrumental Effects Responsible for Decreased Sensitivity with Increasing Mass. *Anal. Chem.* **2003**, *75* (21), 5944–5952.

(59) Badman, E. R.; Hoaglund-Hyzer, C. S.; Clemmer, D. E. Monitoring Structural Changes of Proteins in an Ion Trap over ∼10−200 Ms: Unfolding Transitions in Cytochrome c Ions. *Anal. Chem.* **2001**, *73* (24), 6000–6007.

(60) Revercomb, H. E.; Mason, E. A. Theory of Plasma Chromatography/Gaseous Electrophoresis. Review. *Anal. Chem.* **1975**, *47* (7), 970–983.

(61)   Wyttenbach, T.; Bowers, M. T. Structural Stability from Solution to the Gas Phase: Native Solution Structure of Ubiquitin Survives Analysis in a Solvent-Free Ion Mobility–Mass Spectrometry Environment. *J. Phys. Chem. B* **2011**, *115* (42), 12266–12275.

(62)   Kemper, P. R.; Dupuis, N. F.; Bowers, M. T. A New, Higher Resolution, Ion Mobility Mass Spectrometer. *Int. J. Mass Spectrom.* **2009**, *287* (1–3), 46–57.

(63)   Deng, L.; Ibrahim, Y. M.; Baker, E. S.; Aly, N. A.; Hamid, A. M.; Zhang, X.; Zheng, X.; Garimella, S. V. B.; Webb, I. K.; Prost, S. A.; et al. Ion Mobility Separations of Isomers Based upon Long Path Length Structures for Lossless Ion Manipulations Combined with Mass Spectrometry. *ChemistrySelect* **2016**, *1* (10), 2396–2399.

(64)   Dugourd, P.; Hudgins, R. R.; Clemmer, D. E.; Jarrold, M. F. High-Resolution Ion Mobility Measurements. *Rev. Sci. Instrum.* **1997**, *68* (2), 1122–1129.

(65)   Pepin, R.; Petrone, A.; Laszlo, K. J.; Bush, M. F.; Li, X.; Tureček, F. Does Thermal Breathing Affect Collision Cross Sections of Gas-Phase Peptide Ions? An Ab Initio Molecular Dynamics Study. *J. Phys. Chem. Lett.* **2016**, *7* (14), 2765–2771.

(66)   Freitas, M. A.; Hendrickson, C. L.; Emmett, M. R.; Marshall, A. G. Gas-Phase Bovine Ubiquitin Cation Conformations Resolved by Gas-Phase Hydrogen/Deuterium Exchange Rate and extent1. *Int. J. Mass Spectrom.* **1999**, *185–187*, 565–575.

(67)   Breuker, K.; Oh, H.; Horn, D. M.; Cerda, B. A.; McLafferty, F. W. Detailed Unfolding and Folding of Gaseous Ubiquitin Ions Characterized by Electron Capture Dissociation. *J. Am. Chem. Soc.* **2002**, *124* (22), 6407–6420.

CHAPTER 6

Effects of Polarity on the Structures and Charge States of Native-like Proteins and Protein Complexes in the Gas-Phase

This chapter is reproduced with permission from Allen, S. J.; Schwartz, A. M.; Bush, M. F. "Effects of Polarity on the Structures and Charge States of Native-like Proteins and Protein Complexes in the Gas-Phase" *Analytical Chemistry* **2013**, *84*, 12055–12061. Copyright 2013, American Chemical Society.

6.1 Abstract

Native mass spectrometry and ion mobility spectrometry were used to investigate the gas-phase structures of selected cations and anions of proteins and protein complexes with masses ranging from 6–468 kDa. Under the same solution conditions, the average charge states observed for all native-like anions were less than those for the corresponding cations. Using an RF-confining drift cell, similar collision cross sections were measured in positive and negative ion mode suggesting that anions and cations have very similar structures. This result suggests that for protein and protein complex ions within this mass range, there is no inherent benefit to selecting a specific polarity for capturing a more native-like structure. For peptides and low-mass proteins, polarity and charge-state dependent structural changes may be more significant. The charged-residue model is most often used to explain the ionization of large macromolecules based on the Rayleigh limit, which defines the upper limit of charge that a droplet can hold. Because ions of both polarities have similar structures and the Rayleigh limit does not depend on

polarity, these results cannot be explained by the charged-residue model alone. Rather, the observed charge-state distributions are most consistent with charge-carrier emissions during the final stages of analyte desolvation, with lower charge-carrier emission energies for anions than the corresponding cations. These results suggest that the observed charge-state distributions in most native mass spectrometry experiments are determined by charge-carrier emission processes; although the Rayleigh limit may determine the gas-phase charge states of larger species, *e.g.*, virus capsids.

6.2 Introduction

Native ion mobility mass spectrometry has emerged as a powerful technique for characterizing the stoichiometry, shape, and other aspects of condensed-phase protein and protein complex structure.[62–69] In native mass spectrometry, native-like ions are generated using nanoelectrospray ionization of protein complexes from aqueous solutions that typically contain $\sim 10^{-1}$ M ammonium acetate and are near physiological pH. Hallmarks of native mass spectra are charge-state distributions that are both narrower and lower than those observed for analogous protein ions generated from electrospray ionization using far more common solvent systems, *i.e.*, acidified mixtures of aqueous and organic solvents.

The average charge states of native-like protein and protein complex cations have previously been shown to be strongly correlated with mass[70,71] and solvent-accessible surface area.[72] The origins of those relationships are attributed to the charged-residue model (CRM) for electrospray ionization.[70,73,74] In the CRM, initial charged droplets formed by electrospray evaporate and undergo Coulomb fission when the charge repulsion exceeds the surface tension of the droplet (the Rayleigh limit):[75]

$$z \cdot e = \pi(8\varepsilon_0\gamma)^{1/2}D^{3/2} \tag{6.1}$$

where z is the number of charges, e is the elementary charge, ε_0 is the permittivity of free space, γ is the surface tension (72 mN/m for water at 25 °C), and D is the droplet diameter (often calculated from the mass and an estimated density). This ultimately results in a progeny droplet containing ideally a single analyte. After the evaporation of the final solvent molecules, a multiply charged analyte is left behind. Note that none of the terms in Equation 6.1 depend on polarity; therefore, the CRM would predict the same charge for cations and anions of the same species.

Based on the observation that selected native-like protein cations with masses ranging from 6–80 kDa adopt average charge states below the Rayleigh limit, Hogan *et al.* recently proposed a new electrospray mechanism in which both Rayleigh fission and the emission of small charge carriers contribute to the final charge of native-like ions (Combined Charged Residue Field Emission Model).[76] This charge-carrier emission is analogous to the ionization of analytes in the ion evaporation model (IEM), in which charged species are ejected directly from the surface of electrospray ionization droplets.[74,77] Using a protein density of 1.0 g cm^{-3}, the observed average charge states in the experiments of Hogan *et al.* are consistent with charge-carrier emission energies of 3.53 and 2.95 V nm^{-1}.[76] Under those conditions, native-like ions with masses exceeding ~100 kDa that are charged at the Rayleigh limit would have surface field strengths less than 2.95 V nm^{-1}, which would suppress any contributions from charge-carrier emission to the final charge-state distribution.[76]

The vast majority of native mass spectrometry experiments investigate cations of proteins and protein complexes and there have been relatively few direct comparisons with the properties of the corresponding anions.[71,78] For example, the average charge states observed for non-native

and native-like anions are lower than those for the corresponding cations;[71,78] it was speculated that this difference may be attributed to polarity-dependent ion evaporation kinetics.[70] The structure of these ions can be probed using ion mobility, which measures the drift times of ions through a neutral buffer gas. These drift times can be converted to a collision cross section (Ω), which depends on ion size, shape, and other factors.[79–81] Ion mobility measurements of the ±6 and ±7 charge states of ubiquitin generated from either water or water/organic solutions showed that the Ω values of anions were slightly smaller (2–3%) than the corresponding cations.[65]

The objective of this study is to understand the effects that polarity have on the structures and charge-state distributions of native-like ions. Native mass spectra and Ω values were measured for the native-like cations and anions of 14 species ranging in mass from 6–468 kDa. The average charges states of the native-like cations were 60–90% of that predicted by the Rayleigh limit, whereas those for the native-like anions were only 60–75%. Interestingly, the Ω values of ions generated in both polarities were similar. Because ions of both polarities have very similar structures and the Rayleigh limit is independent of polarity, these results cannot be explained by the CRM alone. We find that charge-carrier emission during the final stages of solvent evaporation from the analyte continue to contribute to the observed charge states of native-like cations exceeding 100 kDa due to an additional charge-carrier emission process not identified previously. Additionally, we find that the average charge states of native-like anions can be predicted using multiple charge-carrier emission processes that have systematically lower critical field strengths than those for the corresponding cations. More generally, these results indicate that the charge states of native-like ions depend most strongly on charge-carrier emission processes during the final stages of electrospray ionization and that ion mobility

spectrometry measurements of native-like ions with different numbers of charges can have very similar Ω.

6.3 Experimental Section

Ions were formed by nanoelectrospray using borosilicate capillaries with inner diameters of 0.78 mm that have a tip at one end pulled to an inner diameter of ~1–3 μm using a micropipette puller (Sutter Instruments Model P-87, Novato, CA). A platinum wire inserted into the other end of the capillary, in contact with the solution, was used as the electrode. Most ions were formed from solutions containing 10 μM protein in 200 mM aqueous ammonium acetate at pH 7.0. For charge reduction experiments, ions were formed from aqueous solutions containing 2.5 μM protein, 200 mM ammonium acetate, and 10 mM triethylamine at pH 7.0. Solution conditions for insulin[21] and sources for all proteins are included in the Supporting Information Table S6.1.

Native mass spectrometry and ion mobility spectrometry data were measured using a modified Waters Synapt G2 HDMS instrument.[22] To minimize any compaction or unfolding of these native-like ions,[23] activation conditions were reduced to those near the threshold for ion transmission. For most experiments, values for the sampling cone voltage, injection voltage into the trap cell, and injection voltage into the ion mobility cell were 20, 4, and 5–10 V, respectively. These same conditions were used in experiments with and without the addition of triethylamine. Other instrument conditions were optimized for high-m/z ions.[24]

This modified Synapt G2 HDMS contains an RF-confining drift cell,[22,25] which replaced the traveling-wave ion mobility cell of the original instrument. The 25.2 cm drift cell consists of 168, 7 mm internal diameter ring electrodes with applied DC potentials that establish a time-

averaged electric field that is constant between the entrance and exit electrodes.[22] Alternate phases of a 2.8 MHz, 100 V peak-to-peak waveform were applied to adjacent electrodes. 2.0 Torr of helium gas was introduced through a 17 mm diameter hole positioned in the center of the top plate of the cell, minimizing any net flow of gas and gas streaming. Pressures were measured for each mobility measurement using an absolute pressure transducer (MKS Baratron Type 626B) that was connected directly to the drift cell. Ω values were determined directly from the slopes of drift time versus reciprocal drift voltage plots, using drift voltages ranging from 100 to 350 V.

The mean and width of each charge-state distribution was determined by fitting the experimental spectrum using Gaussian functions for both the distribution of charge states and the mass spectral peak for each charge state. This fit depends on the abundance, mass, effective mass analyzer resolution, average charge state, and the standard deviation of the charge-state distribution. These five parameters were first guessed and then optimized with respect to the experimental spectrum using the Levenberg−Marquardt, least-squares minimization algorithm as implemented in SciPy.[26]

6.4 Results and Discussion

Intuitively, it would seem that protein ions in the gas phase that have charge states that are closest to those in solution would most resemble the native structures. The net charge states of proteins in solution depend on solution pH, amino acid composition, structure, and interactions with other cellular components. To a crude first approximation, the net charge can be estimated based on the pK_a values of all the individual amino acids, *e.g.*, at physiological pH amino acids that have side chains with acidic functional groups are deprotonated whereas those

with basic functional groups are protonated. Figure 6.1A shows the net charge determined using this approximation, as implemented by Putnam,[27] for the species in Table 6.1. These values range from strongly positive to strongly negative, and are not correlated with protein mass.

The vast majority of native mass spectrometry experiments investigate cations of proteins and protein complexes generated using nanoelectrospray ionization from an aqueous ammonium acetate buffer at a physiologically relevant pH. For example, the mass spectrum of the β-galactosidase homotetramer measured using this approach exhibits peaks assigned to the +46 to +51 charge states (Figure 6.1B). The average charge state observed for β-galactosidase and the other species in Table 6.1 are shown in Figure 6.1E. Clearly, these gas-phase charge states are not correlated with the corresponding charge states in solution (Figure 6.1A). This is consistent with comparisons for peptides[28] and non-native proteins[29,30] between solution charge states and those observed using electrospray ionization that showed no correlation between condensed and gas-phase charge states.

Proteins and protein complexes can alternatively be analyzed as anions by changing the polarity of all power supplies. Performing this experiment, using the same solution containing β-galactosidase, results in the formation of anions that have significantly lower charge states (Figure 6.1C). Interestingly, each native-like anion exhibited a lower average charge state than the corresponding cation generated from the same electrospray solutions (Figure 6.1E), an observation that has been reported previously[9,10] and the origin of which will be discussed later. In the following sections we characterize the relationship between polarity, gas-phase protein charge state, and structure, and evaluate the merits of using charge-state manipulation in native ion mobility mass spectrometry applications focused on characterizing condensed-phase biological structure.
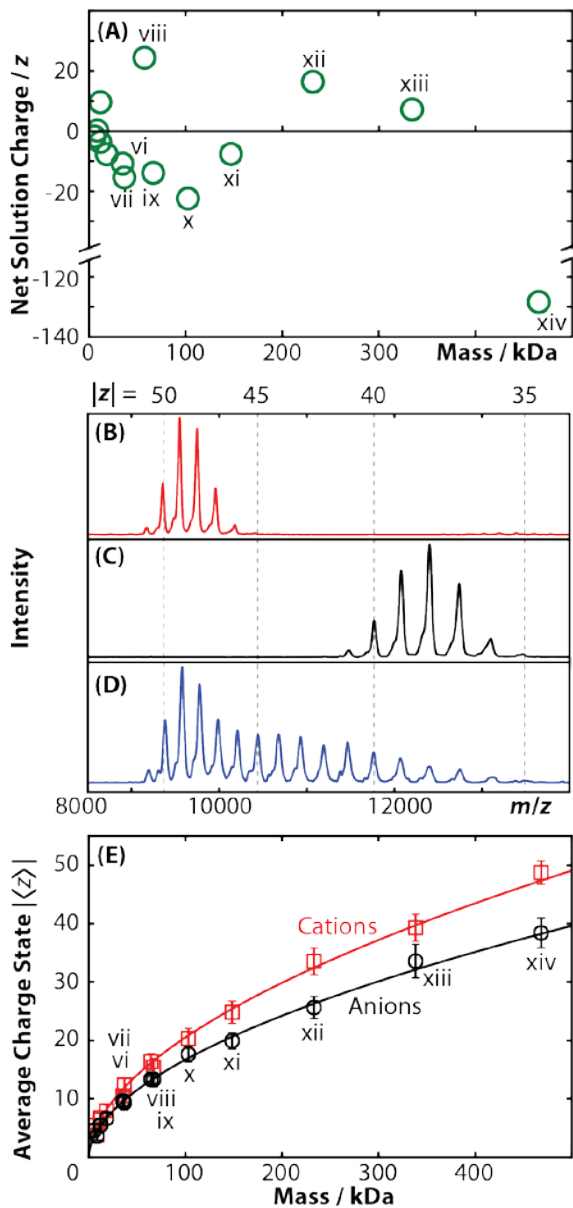
Figure 6.1. (**A**) Net charges in solution estimated based on the pK_a of constituent amino acids.[27] Nanoelectrospray ionization of β-galactosidase in 200 mM ammonium acetate at pH 7.0 measured in (**B**) positive and (**C**) negative polarities. (**D**) is similar to (**B**), but the solution also contained 10 mM triethylamine and additional charge-reduced cations were also observed. (**E**) Absolute value of the

average charge states of selected protein and protein complex ions in positive

(red) and negative (black) ion mode as a function of mass. Power functions are fit

to the data to serve as a guide to the eye. Error bars on those markers span two

standard deviations of the observed charge-state distribution. The mean and width

of each charge-state distribution varied little between experiments performed over

several months. Roman numerals are used to identify specific proteins and protein

complexes (Table 6.1).

6.4.1 Native-Like Ion Structure. Collision cross section (Ω) values were measured

using an RF-confining drift cell that replaced the traveling-wave drift cell in a Waters Synapt G2

HDMS.[22] A previous version of this RF-confining drift cell[25] has directly measured accurate Ω

values for cations of drug-like small molecules,[31] peptides,[32] carbohydrates,[33] non-native

proteins,[25] and native-like protein complexes.[21,25] Drift times measured in an RF-confining drift

cell depend on ion interactions with a buffer gas in the presence of a weak, time-averaged

uniform electric field along the axis of ion transmission.[25] Ion velocities (v) are proportional to

the electric field (E) and the mobility (K) under the conditions in the drift cell:[25]

$$v = KE \tag{6.2}$$

Measured drift times (t_D) in these experiments depend on K, E, and the transport time of ions

from the exit of the drift region to the time-of-flight mass analyzer (t_0):

$$t_D = \frac{\text{drift cell length}}{KE} + t_0 \tag{6.3}$$

Ω values were determined from the experimental K and the Mason-Schamp equation:[18]

$$\Omega = \frac{3ez}{16N} \left(\frac{2\pi}{\mu k_B T} \right)^{1/2} \frac{1}{K} \tag{6.4}$$

where N is the drift-gas number density, μ is the reduced mass of the ion and drift gas, k_B is the Boltzmann constant, and T is the drift-gas temperature. Note that the Ω values reported here depend on the approximations in the Mason-Schamp equation,[20,34,35] which do not affect the conclusions of this work.

Using an RF-confining drift cell, mobilities in helium were measured for the native-like species in Table 6.1. All Ω values measured here are shown in Figure 6.2A and reported in Table S6.2. These Ω values are the averages of multiple mobility measurements, each made on separate days using 7–10 different electric fields. Linear regressions of the data result in R^2 values of 0.9997–0.9999, indicating that any higher-order effects on drift times are very small. Mobility results from this drift cell were validated using values reported previously[21,25,36–38] with differences of less than 3%, demonstrating that the new RF-confining drift cell yields accurate Ω values.

Because the average charge state and polarity are strongly correlated for the higher mass native-like ions, it is challenging to differentiate between the relative contributions of those factors to gas-phase ion structure. To enable a more direct comparison between anions and cations, experiments were also performed in which the charge states were reduced for protein complex cations with masses greater than 60 kDa by adding triethylamine to the electrospray solution. This resulted in the robust and reproducible generation of additional charge-reduced protein charge states spanning a wide m/z range. For example, the native mass spectrum of β-galactosidase measured from a solution with triethylamine (Figure 6.1D) exhibits peaks spanning the charge states observed for both polarities from the original solution containing only aqueous ammonium acetate (Figures 6.1B and 6.1C). No additional energy was deposited into these ions

to generate reduced charge states; the observed charge reduction depends most strongly on the

electrospray voltage and tip position.

Table 6.1. Selected Proteins and their Properties

	Name	n^a	Mass / kDa	$z_{solution}{}^b$	$z_{CRM}{}^c$	$\langle z_{cation}\rangle^d$	$\langle z_{anion}\rangle^d$	$\langle\Omega\rangle^e$ / nm^2
i	insulin	1	5.81	−1.8	5.96	3.78	3.56	7.43
ii	ubiquitin	1	8.57	0.2	7.22	5.46	4.60	9.66
iii	insulin	2	11.6	−3.6	8.40	6.40	5.61	12.3
iv	cytochrome c	1	12.4	9.6	8.61	6.80	5.52	12.6
v	β-lactoglobulin	1	18.4	−7.7	10.6	7.96	6.63	17.0
vi	insulin	6	35.3	−10.8	14.6	10.5	9.63	23.9
vii	β-lactoglobulin	2	36.8	−15.4	14.9	12.4	9.34	28.2
viii	avidin	4	64.3	24.4	19.6	16.4	13.4	36.6
ix	bovine serum albumin	1	67.0	−13.9	20.0	15.4	13.3	40.7
x	concanavalin A	4	103	−22.4	24.7	20.3	17.6	55.1
xi	alcohol dehydrogenase	4	148	−7.6	29.6	24.8	19.9	70.3
xii	pyruvate kinase	4	233	16.4	37.0	33.6	25.6	103
xiii	glutamate dehydrogenase	6	337	7.2	44.5	39.3	33.6	128
xiv	β-galactosidase	4	468	−128.4	52.3	48.8	38.4	166

[a] Oligomeric state.

[b] Estimated net charge in solution.[27]

[c] Charge state calculated using Equation 6.1 and a protein density of 1.0 g cm^{-3}.

[d] Mean of measured charge-state distributions for proteins and protein complexes generated from 200 mM aqueous ammonium acetate.

[e] Mean of all measured collision cross sections. Includes values for cations, charge-reduced cations (rows viii–xiv), and anions.

Comparing the Ω values in Figure 6.2A reveals that cations, anions, and charge-reduced cations of the same species share very similar structures over a wide range of charge states. Standard deviations of Ω measured for all charge states (both polarities) of a given protein or protein complex are less than 2%, indicating that the structures of native-like ions depend weakly on gas-phase charge state and polarity. For peptides or proteins that have masses below those investigated here, structure may depend more strongly on charge state and polarity. To look at subtle differences in structure between polarities, observed Ω values of anions are compared to the average Ω, $\langle\Omega\rangle$, from all measurements (cations, anions, and charge-reduced cations) for that protein (Figure 6.2B). This comparison shows that the Ω values of protein and protein complex anions vary little (less than 2%) from $\langle\Omega\rangle$. There are only small differences between Ω values measured for individual charge states of cations generated from solutions with and without triethylamine, suggesting that the addition of triethylamine does not significantly disrupt native-like structure for the charge states common to both measurements. Comparing observed charge-reduced cation Ω values to $\langle\Omega\rangle$ reveals a subtle trend of increasing Ω value (less than 5%) with decreasing charge state (Figure 6.2C). Additionally, comparing the distributions for the mobilities of ions with the same charge but opposite polarity shows that the structural distributions are similar. For example, Figure S6.1 shows that the mobility distributions for $z = 15$ of bovine serum albumin electrosprayed in positive and negative polarity in the native buffer are indistinguishable. The centroid of the distribution for cations generated from the charge-reducing buffer was indistinguishable from those measured in the native buffer, but interestingly, was slightly wider. Similar mobility centroids and widths were observed in both polarities for the other native-like ions in this study, suggesting that similar structural distributions are present for both polarities.
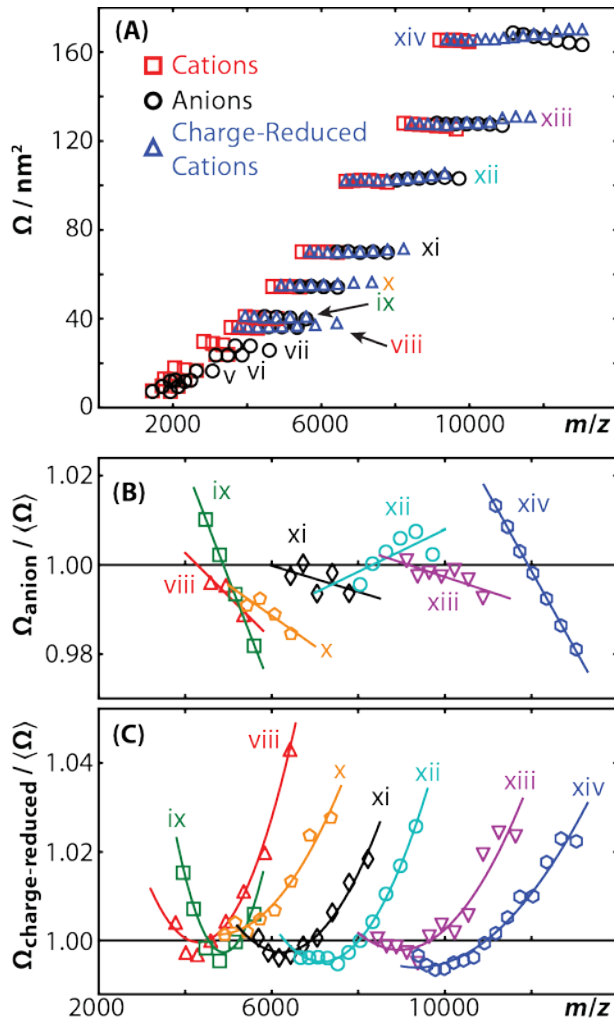
Figure 6.2. (**A**) Collision cross section (Ω) values of protein and protein complex

cations (red), anions (black), and charge-reduced cations (blue) as a function of

m/z. Standard deviations for all Ω values of a given protein show small

differences between the three data sets (less than 2%) indicating that Ω values

depend more on analyte identity than charge state. To show subtle trends in the

data, observed Ω values of protein complex (**B**) anions and (**C**) charge-reduced

cations are plotted relative to the average Ω, $\langle\Omega\rangle$, for all measurements. Data in

(**B**) were fit using linear regressions and those in (**C**) were fit using binomial

regressions. These functions were selected to serve as guides to the eye and are

not intended to imply any mechanistic significance. Roman numerals are used to identify specific proteins and protein complexes (Table 6.1).

6.4.2 Comparisons with Previously Reported Collision Cross Sections. The Ω values for native-like cations generated from solutions containing only aqueous ammonium acetate are similar to values reported previously (less than a 3% difference),[21,25] which validates this experimental approach. There are very few Ω results for native-like anions in the literature, thus it is challenging to make general comparisons. An example is that anions of ubiquitin generated from a pure water solution yielded Ω values of 9.5, 9.7, and 10.2 nm^2 for the –6, –7, and –8 charge states, respectively,[4] whereas we measured Ω values of 9.5 and 9.6 nm^2 for the –4 and –5 charge states generated from solutions containing the protein in 200 mM aqueous ammonium acetate.

Several studies have measured the effects of charge reduction on ion structure. Previous RF-confining drift cell measurements for alcohol dehydrogenase electrosprayed from a solution containing triethylamine indicated that charge reduction has little impact on the overall structure.[39] Traveling-wave ion mobility measurements of avidin, alcohol dehydrogenase, and pyruvate kinase that were charge reduced using 1,8-diazabicyclo[5.4.0]undec-7-ene vapor indicate that the Ω values of the charge-reduced cations increase with decreasing charge state (less than 10%).[40] Recently, an atmospheric pressure corona discharge at the inlet to a mass spectrometer was used to reduce the charge states of native-like pyruvate kinase, whose Ω values were then measured using traveling-wave ion mobility spectrometry.[41] This approach yields a very broad range of charge-reduced cations ($z = 14$–35), including many with significantly lower charge states than those observed here. Calibrated Ω values were reported for $z = 24$–35, with

these values decreasing by 19% with decreasing charge.[41] In contrast, we observe a 4% increase in Ω value across that range with decreasing charge.

Therefore, our results for charge-reduced cations are generally consistent with the previous RF-confining drift cell[39] and the former traveling-wave ion mobility study,[40] but are inconsistent with the latter traveling-wave ion mobility study.[41] This may be attributable to the use of different charge-reduction methods. Alternatively, the former traveling-wave study used constant wave velocity and amplitude during the separation,[40] which has been validated in several studies,[21,25,42] whereas the latter ramped the traveling-wave amplitude during the course of the separation.[41] Therefore, both contributions to this discrepancy will be the subject of future studies.

6.4.3 Origin of Average Charge States. Based on the charged-residue model (CRM), macromolecular charging should follow the Rayleigh limit, which does not depend on polarity. To estimate particle diameter, we first assume a density of 1.0 g cm^{-3}, which is consistent with results from recent differential mobility analysis experiments.[34] Comparing gas-phase charge states predicted by the Rayleigh limit to those measured here for native-like ions generated from 200 mM aqueous ammonium acetate solutions shows that cation and anion charge states are 60–90% and 60–75% of that predicted by the Rayleigh limit, respectively (Table 6.1). These results are comparable to a previous report that cation and anion charge states are up to 90% and 70% of that predicted by the Rayleigh limit, respectively.[10] Since the Rayleigh limit does not depend on polarity and the ion mobility data indicate that both polarities of ions have very similar sizes (Figure 6.2A), differences in average charge state between polarities (Figure 6.1E) cannot be explained solely by the CRM.

Hogan *et al.* have proposed an electrospray ionization mechanism for native-like ions in which the observed charge-state distributions of macromolecules are limited by both the Rayleigh limit and the emission of small charge carriers from nanodroplets during the final stages of ion desolvation (Combined Charged Residue Field Emission Model).[15,43] Briefly, the emission of small charge carriers from the surface of a droplet can occur when the electric field at the surface exceeds the critical electric field strength (E^*) of a charge carrier, which depends on its solvation energy.[44] Charge-carrier emission reduces the electric field strength at the droplet surface, but further neutral solvent evaporation will increase that field. This process can be affected by the presence of multiple charge carriers, each with its own critical field strength, whose emissions become sequentially accessible as the more weakly solvated charge carriers are depleted and the surface field strength increases. The number of charges on the macromolecule (z) for a given E^* is limited by:[15,43]

$$z = \frac{\pi \varepsilon_0 E^*}{e} D^2 \tag{6.5}$$

Average charge states for protein and protein complex cations are plotted versus particle diameter (Figure 6.3A) using a protein density of 1.0 g cm^{-3}. If macromolecular charging was limited by the CRM, the observed protein charge states should agree well with Rayleigh limit values calculated using Equation 6.1 (Figure 6.3, solid black lines). Instead, protein charging falls below the Rayleigh limit, presumably due to charge-carrier emission processes.

The charge states observed for native-like cations i–iv and v–viii are consistent with the average charge states that would be expected if their charge were limited by charge-carrier emission with the critical field strengths for E^*_1 and E^*_2, respectively, that were reported previously.[15] Those critical field strengths suggest that charge-carrier emission will affect the observed charge states of proteins less than 130 kDa; larger native-like ions charged at the

Rayleigh limit would not have adequate surface field strengths to eject the charge carriers associated with E^*_1 and E^*_2.[15] We instead observe that those ions are consistent with a lower-energy, charge-carrier emission process ($E^*_3 = 2.3$ V nm^{-1}). This lower-energy process may correspond to the ejection of small charged clusters that do not contribute to the observed charge states of smaller protein ions generated from lower concentration electrospray buffers (10 mM versus 200 mM). This E^*_3 would limit the charge of proteins up to a particle diameter of ~10 nm. The charge states of larger native-like ions may be limited by either the CRM or perhaps even lower-energy, charge-carrier emission processes.

The diameters in Equations 6.1 and 6.5 depend on the choice of protein density. Two earlier studies reported native-like protein ions having effective densities of 0.6 g cm^{-3},[25,45] which in one case[25] can be attributed to the use of a different collision model to relate the measured ion mobilities with the corresponding particle diameters.[20,34,46] Use of this lower density would suggest that native-like cations adopt charge states that are significantly below the Rayleigh limit, even for megaDalton ions (Figure S6.2A, Table 6.2). For comparison, the density of the solvent-excluded region of proteins is estimated to be ~1.2 g cm^{-3},[47,48] which could be considered the maximum upper limit of protein ions in these experiments. Use of this greater density (Figure S6.3A, Table 6.2) would suggest that the largest native-like cations observed here may be charged at the Rayleigh limit. This possibility could be tested by measuring mass spectra for even larger native-like cations, *e.g.*, virus capsids.
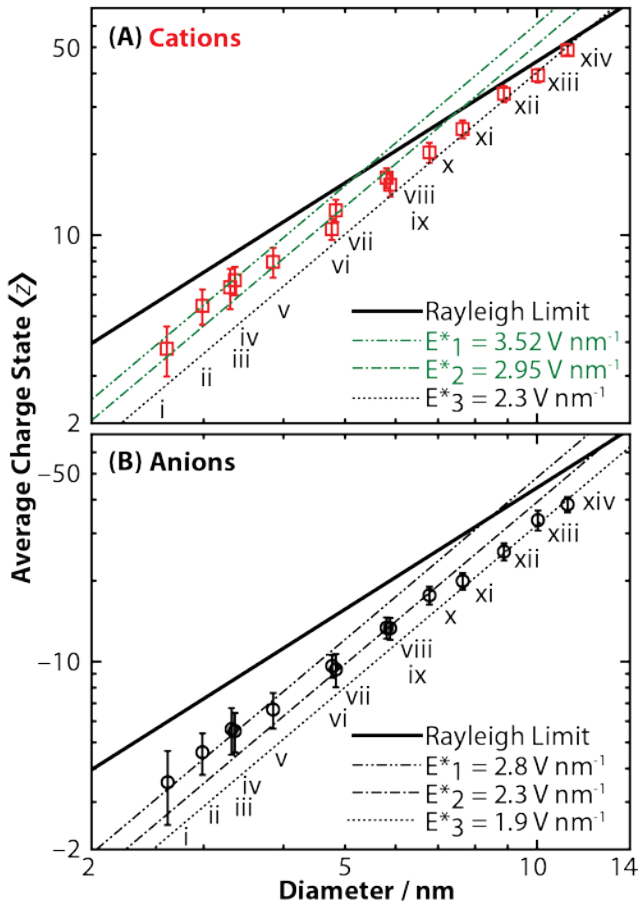
Figure 6.3. Average charge states of proteins and protein complexes measured for (**A**) cations and (**B**) anions as a function of particle diameter calculated using a protein density of 1.0 g cm^{-3}. The charge states observed for cations with diameters less than 6 nm are consistent with the E^*_1 and E^*_2 values reported previously.[15] Those previous results suggested that the charge states of larger native-like ions would be limited by the CRM,[15] whereas the current results are instead consistent with a lower-energy, charge-carrier emission process (E^*_3). The charge states observed for anions are all significantly below the CRM, and are well-explained by three charge-carrier emission processes (E^*_1, E^*_2, and E^*_3) that are systematically lower than the corresponding processes observed for cations.

Analogous plots using proteins densities of 0.6 and 1.2 g cm^{-3} are shown in

Figures S6.2 and S6.3, respectively.

In summary, the combined results of this work and that reported previously[15] are most

consistent with the charge states of native-like cations being limited by discrete charge-carrier

emission processes, although it is possible that these emission energies depend on protein size.

The chemical identity of the charge carriers emitted in these experiments is not known, but

identifying these ions will be the subject of ongoing investigations.

The charge-state distributions of native-like anions were also analyzed using the

Combined Charged Residue Field Emission Model, which has previously only been used for

cations. Results using protein densities of 0.6, 1.0, and 1.2 g cm^{-3} are shown in Figures S6.2B,

6.3B, and S6.3B, respectively, and are summarized in Table 6.2. This analysis shows that these

charge-state distributions are consistent with three charge-carrier emission channels that have

critical field strengths that are systematically lower than the corresponding channels for native-

like cations. These results indicate that the charge states of native-like anions will be limited by

charge-carrier emission for anions with diameters of at least 10 nm, and potentially much larger.

6.5 Conclusions

Over the last two decades, native mass spectrometry has proven to be a powerful tool to

gain insights into condensed-phase protein structure. A common concern regarding these

measurements is that proteins are often electrosprayed in positive ion mode even if they are

predominately negatively charged in solution. In this work, we address these concerns using

charge manipulation and ion mobility spectrometry to probe how gas-phase charge states affect

protein structure in both positive and negative polarities. Native mass spectra and Ω values were measured for the native-like cations and anions of 14 species ranging in mass from 6–468 kDa. Differences in gas-phase charge states were seen between the two polarities with anions having lower average charge states than cations. Interestingly, the Ω values of the ions generated in both polarities were similar, suggesting that gas-phase structure can depend weakly on charge and polarity under native-like conditions. For peptides and low-mass proteins, polarity and charge-state dependent structural changes may be more significant.

This work also provides insights into the electrospray mechanism for proteins and protein complexes in both polarities. The widely accepted electrospray mechanism for macromolecular charging is the CRM, which does not depend on polarity (Equation 6.1). Instead, the observed charge-state distributions are most consistent with charge-carrier emissions during the final stages of analyte desolvation. For all species characterized here, cation charging is consistent with multiple emissions of charge carriers that produce charge states lower than those predicted by the Rayleigh limit. Anions also follow this model, but exhibit lower average charge states than cations, which can be attributed to the lower-energy, charge-carrier emission processes that are available to anions. These results suggest that the observed charge-state distributions in most native mass spectrometry experiments are determined by the emission of charge carriers, although the charge states for some of the largest native-like ions investigated to date[49,50] may be limited by the Rayleigh limit instead of charge-carrier emission. More generally, these results provide a framework for understanding the effects of electrospray polarity on the generation of gas-phase ions and how their structures can provide insights into the corresponding condensed-phase biological structure.

6.6 Acknowledgements

6.7 Supporting Information Available

Supporting Information Table S6.1, Table S6.2, Figure S6.1, Figure S6.2, and Figure S6.3. This

material is available free of charge via the Internet at http://pubs.acs.org.

6.8 References

(1)   Heck, A. J. R. Native Mass Spectrometry: A Bridge between Interactomics and Structural Biology. *Nat. Methods* **2008**, *5* (11), 927–933.

(2)   Ekeowa, U. I.; Freeke, J.; Miranda, E.; Gooptu, B.; Bush, M. F.; Perez, J.; Teckman, J.; Robinson, C. V.; Lomas, D. A. Defining the Mechanism of Polymerization in the Serpinopathies. *Proc. Natl. Acad. Sci.* **2010**, *107* (40), 17146–17151.

(3)   Bleiholder, C.; Dupuis, N. F.; Wyttenbach, T.; Bowers, M. T. Ion Mobility–mass Spectrometry Reveals a Conformational Conversion from Random Assembly to β-Sheet in Amyloid Fibril Formation. *Nat Chem* **2011**, *3* (2), 172–177.

(4)   Wyttenbach, T.; Bowers, M. T. Structural Stability from Solution to the Gas Phase: Native Solution Structure of Ubiquitin Survives Analysis in a Solvent-Free Ion Mobility–Mass Spectrometry Environment. *J. Phys. Chem. B* **2011**, *115* (42), 12266–12275.

(5)   Hilton, G. R.; Benesch, J. L. P. Two Decades of Studying Non-Covalent Biomolecular Assemblies by Means of Electrospray Ionization Mass Spectrometry. *J Roy Soc Interface* **2012**, *9* (70), 801–816.

(6)   Harvey, S. R.; Porrini, M.; Stachl, C.; MacMillan, D.; Zinzalla, G.; Barran, P. E. Small-Molecule Inhibition of c-MYC:MAX Leucine Zipper Formation Is Revealed by Ion Mobility Mass Spectrometry. *J. Am. Chem. Soc.* **2012**, *134* (47), 19384–19392.

(7)   Walldén, K.; Williams, R.; Yan, J.; Lian, P. W.; Wang, L.; Thalassinos, K.; Orlova, E. V.; Waksman, G. Structure of the VirB4 ATPase, Alone and Bound to the Core Complex of a Type IV Secretion System. *Proc. Natl. Acad. Sci.* **2012**, *109* (28), 11348–11353.

(8)   Lu, C.; Turley, S.; Marionni, S. T.; Park, Y.-J.; Lee, K. K.; Patrick, M.; Shah, R.; Sandkvist, M.; Bush, M. F.; Hol, W. G. J. Hexamers of the Type II Secretion ATPase GspE from Vibrio Cholerae with Increased ATPase Activity. *Structure* **2013**, *21* (9), 1707–1717.

(9)   Fernandez de la Mora, J. Electrospray Ionization of Large Mutliply Charged Species Proceeds via Dole's Charged Residue Mechanism. *Anal. Chim. Acta* **2000**, *406* (1), 93–104.

(10)   Heck, A. J. R.; van den Heuvel, R. H. H. Investigation of Intact Protein Complexes by Mass Spectrometry. *Mass Spectrom. Rev.* **2004**, *23* (5), 368–389.

(11)   Kaltashov, I. A.; Mohimen, A. Estimates of Protein Surface Areas in Solution by Electrospray Ionization Mass Spectrometry. *Anal. Chem.* **2005**, *77* (16), 5370–5379.

(12)   Dole, M.; Mack, L. L.; Hines, R. L.; Mobley, R. C.; Ferguson, L. D.; Alice, M. B. Molecular Beams of Macroions. *J. Chem. Phys.* **1968**, *49* (5), 2240–2249.

(13)   Konermann, L.; Ahadi, E.; Rodriguez, A. D.; Vahidi, S. Unraveling the Mechanism of Electrospray Ionization. *Anal. Chem.* **2013**, *85* (1), 2–9.

(14)   Rayleigh, L. On the Equilibrium of Conducting Masses Charged with Electricity. *Philos. Mag.* **1882**, *14*, 184–186.

(15)   Hogan, C. J.; Carroll, J. A.; Rohrs, H. W.; Biswas, P.; Gross, M. L. Combined Charged Residue-Field Emission Model of Macromolecular Electrospray Ionization. *Anal. Chem.* **2009**, *81* (1), 369–377.

(16)   Kebarle, P.; Peschke, M. On the Mechanisms by Which the Charged Droplets Produced by Electrospray Lead to Gas Phase Ions. *Anal. Chim. Acta* **2000**, *406* (1), 11–35.

(17)   Konermann, L.; Douglas, D. J. Unfolding of Proteins Monitored by Electrospray Ionization Mass Spectrometry: A Comparison of Positive and Negative Ion Modes. *J. Am. Soc. Mass Spectrom.* **1998**, *9* (12), 1248–1254.

(18)   Mason, E. A.; McDaniel, E. W. *Transport Properties of Ions in Gases*; Wiley: New York, 1988.

(19)   Fenn, L. S.; Kliman, M.; Mahsut, A.; Zhao, S. R.; McLean, J. A. Characterizing Ion Mobility-Mass Spectrometry Conformation Space for the Analysis of Complex Biological Samples. *Anal. Bioanal. Chem.* **2009**, *394* (1), 235–244.

(20)   Wyttenbach, T.; Bleiholder, C.; Bowers, M. T. Factors Contributing to the Collision Cross Section of Polyatomic Ions in the Kilodalton to Gigadalton Range: Application to Ion Mobility Measurements. *Anal. Chem.* **2013**, *85* (4), 2191–2199.

(21)   Salbo, R.; Bush, M. F.; Naver, H.; Campuzano, I.; Robinson, C. V.; Pettersson, I.; Jørgensen, T. J. D.; Haselmann, K. F. Travelling Wave Ion Mobility Mass Spectrometry: Calibrants and Instrumental Conditions Are Crucial for Correct Collision Cross-Section Measurements. *Rapid Commun. Mass Spectrom.* **2012**, *26*, 1181–1193.

(22)   Allen, S. J.; Marionni, S. T.; Giles, K.; Gilbert, T.; Bush, M. F. Design and Characterization of a New Ion Mobility Cell for Protein Complexes. In *60th American Society for Mass Spectrometry Conference*; Vancouver, BC, 2012.

(23)   Hall, Z.; Politis, A.; Bush, M. F.; Smith, L. J.; Robinson, C. V. Charge-State Dependent Compaction and Dissociation of Protein Complexes: Insights from Ion Mobility and Molecular Dynamics. *J. Am. Chem. Soc.* **2012**, *134* (7), 3429–3438.

(24)   Benesch, J. L. P.; Ruotolo, B. T.; Simmons, D. A.; Robinson, C. V. Protein Complexes in the Gas Phase: Technology for Structural Genomics and Proteomics. *Chem. Rev.* **2007**, *107* (8), 3544–3567.

(25)   Bush, M. F.; Hall, Z.; Giles, K.; Hoyes, J.; Robinson, C. V.; Ruotolo, B. T. Collision Cross Sections of Proteins and Their Complexes: A Calibration Framework and Database for Gas-Phase Structural Biology. *Anal. Chem.* **2010**, *82* (22), 9557–9565.

(26)   Jones, E.; Oliphant, T.; Peterson, P. *SciPy: Open Source Scientific Tools for Python*; 2001.

(27) Putnam, C. *Protein Calculator*; 2006.

(28) Wang, G.; Cole, R. B. Disparity Between Solution-Phase Equilibria and Charge State Distributions in Positive-Ion Electrospray Mass Spectrometry. *Org. Mass Spectrom.* **1994**, *29* (8), 419–427.

(29) Kelly, M. A.; Vestling, M. M.; Fenselau, C. C. Electrospray Analysis of Proteins: A Comparison of Positive-Ion and Negative-Ion Mass Spectra at High and Low pH. *Org. Mass Spectrom.* **1992**, *27*, 1143–1147.

(30) Carbeck, J. D.; Severs, J. C.; Gao, J.; Wu, Q.; Smith, R. D.; Whitesides, G. M. Correlation between the Charge of Proteins in Solution and in the Gas Phase Investigated by Protein Charge Ladders, Capillary Electrophoresis, and Electrospray Ionization Mass Spectrometry. *J. Phys. Chem. B* **1998**, *102* (51), 10596–10601.

(31) Campuzano, I.; Bush, M. F.; Robinson, C. V.; Beaumont, C.; Richardson, K.; Kim, H.; Kim, H. I. Structural Characterization of Drug-like Compounds by Ion Mobility Mass Spectrometry: Comparison of Theoretical and Experimentally Derived Nitrogen Collision Cross Sections. *Anal. Chem.* **2012**, *84* (2), 1026–1033.

(32) Bush, M. F.; Campuzano, I. D. G.; Robinson, C. V. Ion Mobility Mass Spectrometry of Peptide Ions: Effects of Drift Gas and Calibration Strategies. *Anal. Chem.* **2012**, *84* (16), 7124–7130.

(33) Pagel, K.; Harvey, D. J. Ion Mobility–Mass Spectrometry of Complex Carbohydrates: Collision Cross Sections of Sodiated N-Linked Glycans. *Anal. Chem.* **2013**, *85* (10), 5138–5145.

(34) Maißer, A.; Premnath, V.; Ghosh, A.; Nguyen, T. A.; Attoui, M.; Hogan, C. J. Determination of Gas Phase Protein Ion Densities via Ion Mobility Analysis with Charge Reduction. *Phys. Chem. Chem. Phys.* **2011**, *13* (48), 21630–21641.

(35) Siems, W. F.; Viehland, L. A.; Hill, H. H., Jr. Improved Momentum-Transfer Theory for Ion Mobility. 1. Derivation of the Fundamental Equation. *Anal. Chem.* **2012**, *84* (22), 9782–9791.

(36) Valentine, S. J.; Counterman, A. E.; Clemmer, D. E. Conformer-Dependent Proton-Transfer Reactions of Ubiquitin Ions. *J. Am. Soc. Mass Spectrom.* **1997**, *8*, 954–961.

(37) Shelimov, K. B.; Clemmer, D. E.; Hudgins, R. R.; Jarrold, M. F. Protein Structure in Vacuo: Gas-Phase Conformations of BPTI and Cytochrome c. *J. Am. Chem. Soc.* **1997**, *119* (9), 2240–2248.

(38) Counterman, A. E.; Valentine, S. J.; Srebalus, C. A.; Henderson, S. C.; Hoaglund, C. S.; Clemmer, D. E. *J Am Soc Mass Spectrom* **1998**, *9*, 743–759.

(39) Hall, Z.; Robinson, C. V. Do Charge State Signatures Guarantee Protein Conformations? *J. Am. Soc. Mass Spectrom.* **2012**, *23* (7), 1161–1168.

(40) Bornschein, R. E.; Hyung, S.-J.; Ruotolo, B. T. Ion Mobility-Mass Spectrometry Reveals Conformational Changes in Charge Reduced Multiprotein Complexes. *J. Am. Soc. Mass Spectrom.* **2011**, *22* (10), 1690–1698.

(41) Campuzano, I. D. G.; Schnier, P. D. Coupling Electrospray Corona Discharge, Charge Reduction and Ion Mobility Mass Spectrometry: From Peptides to Large Macromolecular Protein Complexes. *Int. J. Ion Mobil. Spectrom.* **2013**, *16* (1), 51–60.

(42) Ruotolo, B. T.; Benesch, J. L. P.; Sandercock, A. M.; Hyung, S.-J.; Robinson, C. V. Ion Mobility–mass Spectrometry Analysis of Large Protein Complexes. *Nat. Protoc.* **2008**, *3* (7), 1139–1152.

(43)   Hogan, C. J.; Carroll, J. A.; Rohrs, H. W.; Biswas, P.; Gross, M. L. Charge Carrier Field Emission Determines the Number of Charges on Native State Proteins in Electrospray Ionization. *J. Am. Chem. Soc.* **2008**, *130* (22), 6926–6927.

(44)   Labowsky, M.; Fenn, J. B.; Fernandez de la Mora, J. A Continuum Model for Ion Evaporation from a Drop: Effect of Curvature and Charge on Ion Solvation Energy. *Anal. Chim. Acta* **2000**, *406* (1), 105–118.

(45)   Kaddis, C. S.; Lomeli, S. H.; Yin, S.; Berhane, B.; Apostol, M. I.; Kickhoefer, V. A.; Rome, L. H.; Loo, J. A. Sizing Large Proteins and Protein Complexes by Electrospray Ionization Mass Spectrometry and Ion Mobility. *J. Am. Soc. Mass Spectrom.* **2007**, *18* (7), 1206–1216.

(46)   Hogan, C. J.; Fernandez de la Mora, J. Ion Mobility Measurements of Nondenatured 12–150 kDa Proteins and Protein Multimers by Tandem Differential Mobility Analysis–Mass Spectrometry (DMA-MS). *J. Am. Soc. Mass Spectrom.* **2011**, *22* (1), 158–172.

(47)   Quillin, M. L.; Matthews, B. W. Accurate Calculation of the Density of Proteins. *Acta Crystallogr.* **2000**, *D56* (7), 791–794.

(48)   Fischer, H.; Polikarpov, I.; Craievich, A. F. Average Protein Density Is a Molecular-Weight-Dependent Function. *Protein Sci.* **2004**, *13* (10), 2825–2828.

(49)   Shoemaker, G. K.; van Duijn, E.; Crawford, S. E.; Uetrecht, C.; Baclayon, M.; Roos, W. H.; Wuite, G. J. L.; Estes, M. K.; Prasad, B. V. V.; Heck, A. J. R. Norwalk Virus Assembly and Stability Monitored by Mass Spectrometry. *Mol. Cell. Proteomics* **2010**, *9* (8), 1742–1751.

(50)   Snijder, J.; Rose, R. J.; Veesler, D.; Johnson, J. E.; Heck, A. J. R. Studying 18 MDa Virus Assemblies with Native Mass Spectrometry. *Angew. Chem. Int. Ed.* **2013**, *52* (14), 4020–4023.

CHAPTER 7

Supercharging of Native-like Protein and Protein Complex Cations and Anions: Insights into Electrospray Mechanisms

This chapter is reproduced with permission from Allen, S. J.; Stachl, C. N.; Bush, M. F. "Supercharging of Native-like Protein and Protein Complex Cations and Anions: Insights into Electrospray Mechanisms" **2017**, manuscript in preparation.

7.1 Abstract

Native-like protein and protein complexes are typically electrosprayed from aqueous buffered solutions at biologically relevant pH. The resulting ions have shapes that correlate well with their condensed-phase structures, but have relatively low charge states that can be more challenging to mass analyze and dissociate. Alternatively, supercharging reagents, such as m-NBA or sulfolane, can be added to the electrospray buffer to generate ions with higher charge states than observed for solutions without those additives. Several supercharging mechanisms have been proposed, but a detailed molecular understanding of this process remains elusive. Here, ion mobility mass spectrometry was used to investigate the effects of supercharging on the structures and charge states of protein and protein complex cations. Native-like cations are produced by electrospray ionization from solutions containing 200 mM ammonium acetate with either 1% m-NBA, 1% sulfolane, or 3% sulfolane. In general, sulfolane is more effective at supercharging the proteins and protein complexes studied here, especially at higher concentrations. Ion mobility reveals that the structures of supercharged cations are independent

of supercharging reagent identity and concentration. Anions produced from 200 mM ammonium acetate solutions containing 3% sulfolane were compared to the corresponding cations. Interestingly, the structures of supercharged ions can depend on polarity. Significant mass adduction to supercharged charge states observed in these experiments suggests an enrichment of supercharging reagent during droplet desolvation, which may inhibit charge-carrier emission that contributes to higher observed charge states.

7.2 Introduction

Electrospray ionization of proteins and protein complexes from aqueous buffered solutions at biologically relevant pH (native-like solutions) produce a range of ion charge states that are narrower and lower in magnitude than those produced from acidified aqueous/organic solutions (denaturing solutions). The charged-residue model (CRM) is commonly used to describe the origin of charge states from electrospray ionization of native-like solutions.[1,2] In the CRM,[3,4] initial charged droplets formed by electrospray evaporate and undergo Coulomb fission when the charge repulsion exceeds the surface tension of the droplet (the Rayleigh limit):[5]

$$z \cdot e = \pi (8\varepsilon_0 \gamma)^{1/2} D^{3/2} \qquad (7.1)$$

where z is the number of charges, e is the elementary charge, ε_0 is the permittivity of free space, γ is the surface tension (72 mN m^{-1} for water at 25 °C), and D is the droplet diameter (often calculated from the mass and an estimated density). Other mechanisms of biomolecule charging in the gas phase are the charge-carrier field emission model[6–8] and the chain ejection model.[9,10]

Understanding how condensed-phase and gas-phase charge states and structures compare is paramount in interpreting mass spectrometry data. Many studies have focused on the effects of solvent on the charge-state distributions of biomolecules in the gas phase.[11–16] Specifically, Williams and coworkers observed significantly enhanced gas-phase charge states when m-

nitrobenzyl alcohol (m-NBA) or glycerol were added to denaturing electrospray solutions.[14,15] These "supercharged" ions are useful because they are more amendable to fragmentation methods (such as collision-induced[17,18] and electron-capture[18] dissociation) and the lower m/z values ions are more efficiently detected by mass analyzers.[19]

Foundational studies on the mechanism of supercharging from aqueous/organic solutions suggest low boiling point, high surface tension supercharging additives are preferentially enriched in the droplet during desolvation,[14,15,20] resulting in a higher charge (according to Equation 7.1, $\gamma^{1/2}$ is proportional with z). Although, results of other organic compounds added to pure water contradict this theory.[21] Interestingly, enhanced charge states are observed from aqueous buffered solutions even though the surface tension of water is higher than that of common supercharging reagents.[22–24]

It is well understood that enhanced charge states occur in the electrospray droplet, rather than from supercharging reagent interactions with the analytes in bulk solution. For example, circular dichroism and hydrogen deuterium exchange data show that addition of supercharging reagents to protein solutions does not affect solution structure.[25,26] A study by Sterling et al. showed that when 0.05% m-NBA was added to a protein solution then dialyzed out, typical charge states were observed.[27] Recently, Going et al. used guanidine HCl melts and tryptophan fluorescence to measure protein unfolding of cytochrome c in solutions containing various supercharging reagents.[24] They found that supercharging reagent concentrations up to 10% v/v did not affect protein structure in solution. These studies and others[28,29] suggest that preferential enrichment of supercharging reagents occur during droplet desolvation. Studies by Williams and coworkers suggest that a combination of surface tension effects and protein unfolding due to thermal denaturation are the primary mechanisms of supercharging.[26,27] This is in contrast to

reports claiming that supercharged charge states are not a result of protein unfolding. For example, supercharging from aqueous solutions demonstrates that these protein ions can retain native-bound ligands[25] and exhibit only modest increases in structure.[30]

Clearly there are discrepancies among previous supercharging studies of native-like protein and protein complexes which stem from specific examples with limited parameter spaces, rather than a broad, unified data set of supercharged proteins and protein complexes ranging in mass and oligomeric states. Here, ion mobility mass spectrometry is used to characterize native-like proteins and protein complexes, ranging from 6 to 337 kDa, supercharged using either 1% m-NBA or 1 to 3% sulfolane in ammonium acetate solutions. Samples are electrosprayed in positive and negative ion mode to study the effects of polarity on supercharging. Ion mobility data is used to determine the gas-phase structures of supercharged charge states.

7.3 Experimental Section

7.3.1 Samples and Ionization. All reagents and protein samples were purchased from Sigma-Aldrich. Protein and protein complex samples were dissolved in 200 mM ammonium acetate at pH 7.0 to a concentration of 10 μM. Samples were desalted using Micro Bio-spin 6 columns (Bio-Rad, Hercules, CA) that were equilibrated to the same buffer. After buffer exchange, sulfolane or m-nitrobenzyl alcohol (m-NBA) was added (1 to 3% v/v) to a solution containing a final protein concentration of ~5 μM. Ions were formed using nanoelectrospray ionization using pulled borosilicate capillaries; capillary dimensions and procedures have been described elsewhere.[31]

7.3.2 Ion Mobility Mass Spectrometry. All ion mobility mass spectrometry measurements were performed on a modified Waters Synapt G2 HDMS in which the traveling-

wave ion mobility cell was replaced with an RF-confining drift cell[32] filled with 2 Torr helium

gas. Field-dependent measurements were performed to determine the transport times of ions

outside of the drift region. Using these results, field-independent measurements at a drift voltage

of 161 V were used to determine a collision cross section (Ω), described by the Mason-Schamp

equation:[33]

$$\Omega = \frac{3ez}{16N}\left(\frac{2\pi}{\mu k_B T}\right)^{1/2}\frac{1}{K} \tag{7.2}$$

where e is the elementary charge, z is the ion charge state, N is the drift-gas number density, μ is

the reduced mass of the ion and drift gas, k_B is the Boltzmann constant, and T is the drift-gas

temperature (300 K), and K is the mobility of the ion.

7.4 Results and Discussion

7.4.1 Effects of Reagents and Concentrations on the Supercharging of Native-Like

Ions. Typical native mass spectrometry results of proteins and protein complexes electrosprayed

in ammonium acetate solutions exhibit narrow charge-state distributions that are relatively low in

charge compared to charge states produced from conventional electrospray solutions (acidified

aqueous/organic solutions). An example of a native mass spectrum of the protein concanavalin A

is shown in Figure 7.1a. Concanavalin A exist as a monomer, dimer, and tetramer in solution,

which results in three separate charge-state distributions corresponding to the different

oligomeric states.

To investigate the effects of supercharging reagent identity and concentration, m-NBA

and sulfolane were used to supercharge native-like proteins and protein complexes ranging in

mass from 6 to 337 kDa. The supercharging reagents were selected based on their extensive use

and characterization in literature. Two different v/v ratios were selected for sulfolane to study the

effects of concentration on supercharging effectiveness. Solutions containing 1% m-NBA were selected as a direct comparison to 1% sulfolane; m-NBA is not soluble at higher concentrations in aqueous solutions. Figures 7.1b and 7.1c show the resulting mass spectra of concanavalin A when 1% m-NBA or 1% sulfolane, respectively, is added to the 200 mM ammonium acetate solution. In this example, 1% m-NBA produces tetrameric concanavalin A ions with a highest charge state of 27+ while 1% sulfolane produces charge states up to 26+. Adding 3% sulfolane (Figure 7.1d) results in significantly higher charge states with a highest observed charge state of 31+. Supercharging with 3% sulfolane (Figure 7.1d) results in a 41% increase in highest observed charge state compared to solutions not containing supercharging reagents (Figure 7.1a).
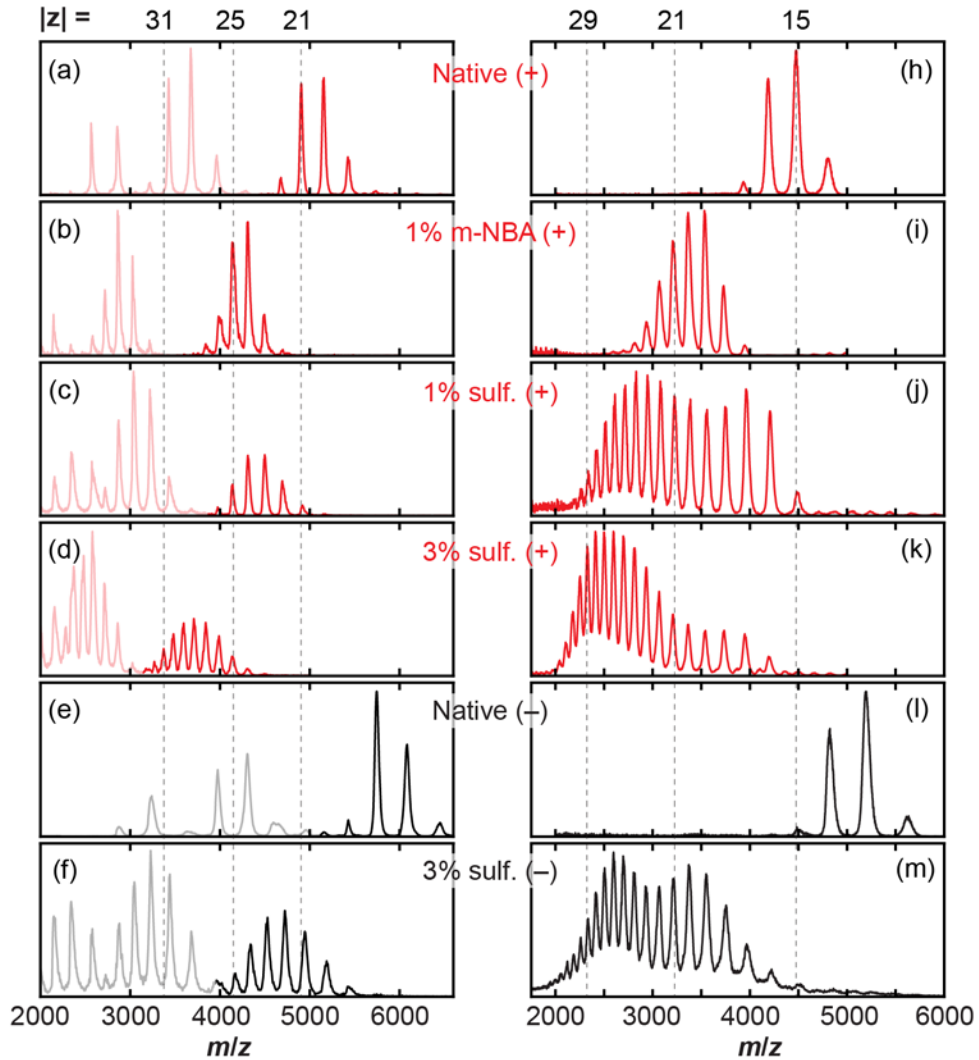
Figure 7.1. (a – f) Mass spectra of concanavalin A. The charge-state distribution corresponding to the tetramer complex is shown in bold. (h – m) Mass spectra of bovine serum albumin. Ions were produced using positive ion mode (+) electrospray ionization from solutions containing 200 mM ammonium acetate (native, a and h) or also containing 1% m-NBA (b and i), 1% sulfolane (c and j), or 3% sulfolane (d and k). Ions were also produced using negative ion mode (–) electrospray ionization from solutions containing 200 mM ammonium acetate (native, e and i) or also containing 3% sulfolane (f and m).

Another example of supercharging using the same reagents and concentrations used above are shown in Figure 7.1h to 7.1k for bovine serum albumin (67 kDa monomeric protein). In contrast to the results for concanavalin A, bovine serum albumin solutions containing 1% sulfolane (Figure 7.1j) produced higher charge states than solutions containing 1% m-NBA (Figure 7.1i). Bovine serum albumin ions produced from solutions containing 3% sulfolane (Figure 7.1k) resulted in a 94% increase in the highest observed charge state compared to solutions not containing supercharging reagents (Figure 7.1h). Electronic Supplementary Material Figure S7.1 shows a summary of percent increase in highest charge state produced from solutions with and without supercharging reagents, for several proteins and protein complexes. In general, sulfolane was more effective at supercharging proteins and protein complexes studied here, especially at higher v/v. The effectiveness of m-NBA to increase charge states, relative to sulfolane, decreased with increasing analyte mass.

7.4.2 Effects of Polarity on the Supercharging of Native-Like Ions. The structures of native-like ions have been shown to be weakly dependent on the polarity of charge states.[8] That study investigated the charge states of native-like ions produced from 200 mM ammonium acetate solutions. Here, the effects of polarity on the charge states of native-like ions from buffered solutions containing 3% sulfolane is investigated. Figure 7.1e shows negative ion mode electrospray ionization of bovine serum albumin ions from 200 mM ammonium acetate solutions. Consistent with previous observations,[8] native-like concanavalin A anions (Figure 7.1e) exhibit lower magnitude charges states than native-like cations (Figure 7.1a). Supercharged anions were produced from 200 mM ammonium acetate solutions containing 3% sulfolane and are shown in Figure 7.1f. The percent increase in highest observed charge state for concanavalin A anions produced from 3% sulfolane versus solutions without is 32%, which is smaller than the

percent increase observed for the corresponding cations. In contrast, significantly enhanced

supercharging was observed for bovine serum albumin anions produced from 3% sulfolane

solutions (Figure 7.1m) compared to solutions without (Figure 7.1l). Bovine serum albumin

anions produced from solutions containing 3% sulfolane resulted in a 113% increase in the

highest observed charge state compared to solutions not containing supercharging reagents.

Interestingly, solutions containing m-NBA that were electrosprayed in negative ion mode

resulted in suppressed ion signal and no supercharged charge states for the analytes studied here.

Early studies of supercharging in negative ion mode showed minimal increases in charge state.[26]

A recent study reported significant supercharging of cytochrome c, myoglobin, and a single-

stranded DNA 12-mer anions electrosprayed from 100 mM ammonium acetate containing 1% m-

NBA, although, their experimental conditions involved very high temperatures which may have

enabled the production of highly charged anions.[22]

7.4.3 Effects of Supercharging on the Structures of Protein Ions. Ion mobility was

used to investigate the effects of supercharging reagents on the structures of protein and protein

complex ions and the retention of native-like properties. First, the effects of supercharging

reagent identity and concentration on the Ω values of protein and protein complex ions were

evaluated. Figure 7.2a to 7.2c shows Ω distributions of selected charge states of tetrameric

concanavalin A. The Ω distribution of the 21+ charge state produced from solutions containing

1% sulfolane is indistinguishable from that observed from solutions without supercharging

reagents (Figure 7.2a). Figure 7.2b shows Ω distributions of the 25 charge state produced from

varying supercharging reagents and concentrations in positive and negative ion mode.

Interestingly, all Ω distributions are similar and are subtly shifted to higher Ω values relative to

the 21+ charge state. Figure 7.2c shows the Ω distribution of the 31+ charge state produced from

solutions containing 3% sulfolane, which is shifted (by ~9%) to higher Ω values relative to the Ω distribution of the 21+ (Figure 7.2a). This example shows that for concanavalin A, the subtle changes in Ω are independent of supercharging reagent and the polarity.
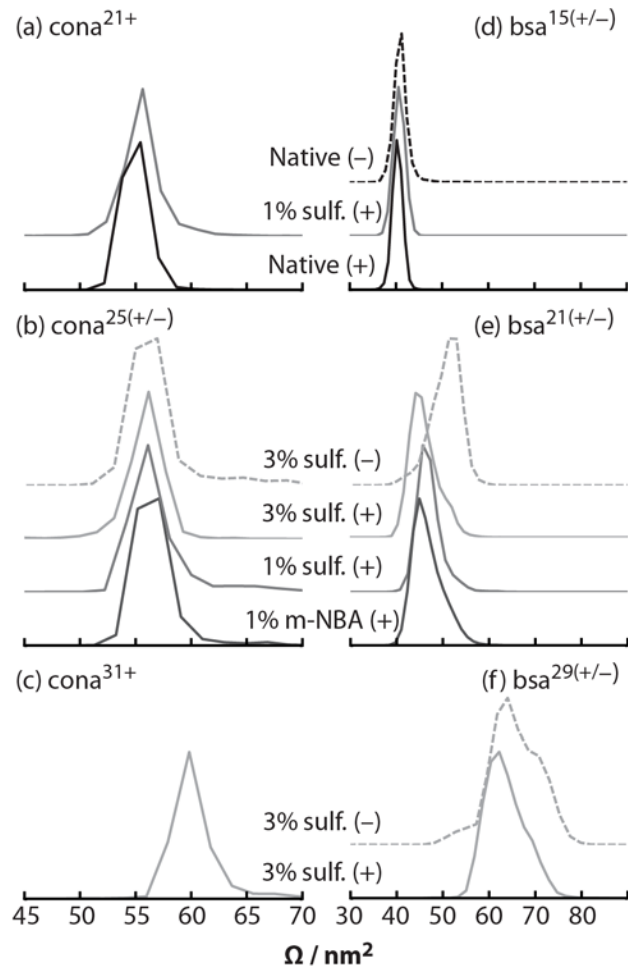
Figure 7.2. Collision cross section (Ω) distributions of selected charge states of (a – c) concanavalin A and (d – f) bovine serum albumin. Ions are produced using either positive (+, solid lines) or negative (–, dashed lines) ion mode electrospray ionization from solutions containing 200 mM ammonium acetate (native) or also containing 1% m-NBA, 1% sulfolane, or 3% sulfolane.

For comparison, the Ω distributions for selected charge states of bovine serum albumin are shown in Figure 7.2d to 7.2f. A common charge state of 15 is shared by cations produced from solutions with and without 1% sulfolane, and anions produced from solutions without supercharging reagents (Figure 7.2d). The Ω distributions of the 15 charge state are indistinguishable for ions produced from those solutions. Additionally, the 21+ charge state of bovine serum albumin ions produced from varying supercharging reagents and concentrations show very similar Ω distributions (Figure 7.2e). Interestingly, the 21– Ω distribution is different from the 21+ distribution, suggesting polarity specific structural changes for supercharged bovine serum albumin ions. At a charge state of 29, Ω distributions ions produced from solutions containing 3% sulfolane in positive or negative ion mode are similar (Figure 7.2f). Similar to concanavalin A, the Ω distributions of bovine serum albumin ions are independent of supercharging reagent identity. But, the Ω distributions of some bovine serum albumin charge states depend strongly on polarity. Additionally, Figure 7.1f shows a significant increase in Ω values of supercharged bovine serum albumin ions relative to the Ω values of native-like ions (Figure 7.1d).

To further investigate the trends observed for concanavalin A and bovine serum albumin, ion mobility measurements for several other protein and protein complex cations from 200 mM ammonium acetate solutions containing 1% m-NBA, 1% sulfolane, or 3% sulfolane are shown in Figure 7.3a. Because not all Ω distributions are Gaussian-like in shape, critical values from the cumulative distribution functions (CDF) were used to represent the distributions, as illustrated in Electronic Supplementary Material Figure S7.2. Briefly, the CDF is the probability of the distribution's density, *e.g.*, the Ω at which the CDF has a value of 50% corresponds to the center of the density of the Ω distribution. The markers in Figure 7.3 correspond to that critical value

for each Ω distribution ($\Omega_{50\%}$). Similar to the observations from Figure 7.2, Figure 7.3 shows that the Ω values of these selected proteins and protein complexes are independent of supercharging identity and concentrations. For all of the ions investigated, charge states that were shared between solutions with and without supercharging reagents showed similar Ω values, which suggests that ions can be produced from supercharging solutions without resolvable changes to protein structure. Additionally, most higher mass proteins (avidin and greater) exhibit intermediate supercharged charge states that have Ω values similar to native-like Ω values. Though, the highest charge states produced from supercharging solutions can exhibit significantly higher Ω values than native-like ions, which is indicative of structural unfolding and a disruption of native-like conformations.

The effect of polarity on Ω values of ions produced from 200 mM ammonium acetate solutions containing 3% sulfolane was investigated for the selected proteins and protein complexes (Figure 7.3b). For avidin, bovine serum albumin, and pyruvate kinase, the Ω values of some charge states are dependent on the polarity. Specifically, the charge states that exhibit different Ω values between polarities are all larger than native-like Ω values, suggesting a polarity-specific behavior is observed at intermediate unfolding pathways for supercharged ions. The Ω values for supercharged cations and anions of several other proteins and protein complexes are shown in Electronic Supplementary Material Figure S7.3.
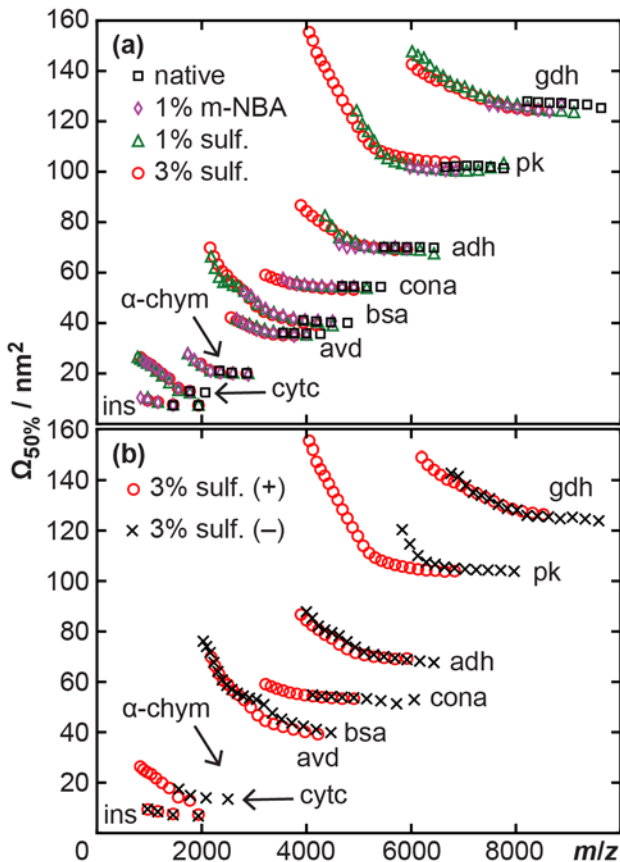
Figure 7.3. 50% critical values of the CDF of Ω distributions ($\Omega_{50\%}$) for insulin (ins), cytochrome c (cytc), α-chymotrypsinogen (α-chymo), avidin (avd), bovine serum albumin (bsa), tetrameric concanavalin A (cona), alcohol dehydrogenase (adh), pyruvate kinase (pk), and glutamate dehydrogenase (gdh). (a) Ions produced from positive ion mode electrospray ionization from 200 mM ammonium acetate solutions (native, black squares) or also containing 1% m-NBA (magenta diamonds), 1% sulfolane (green triangles), or 3% sulfolane (red circles). (b) Ions produced from either positive (+, red circles) or negative (−, black x's) ion mode electrospray ionization from 200 mM ammonium acetate solutions containing 3% sulfolane.

In general, ions produced from solutions containing supercharging reagents can result in enhanced charge states with Ω values that are similar to native-like Ω values. Although, for the highest observed charge states here, significantly larger Ω values relative to native-like Ω values suggests that supercharging proteins and protein complexes can result in significant unfolding and loss of native-like structure.

7.4.4 Insights into Supercharging Mechanisms. The extent of supercharging is highly dependent on the electrospray conditions. Figure 7.4a shows the mass spectrum of β-galactosidase (~468 kDa tetrameric protein complex) electrosprayed in positive ion mode from a 200 mM ammonium acetate solution. When 3% sulfolane was added to the solution and the electrospray was operated at 0.74 kV, the mass spectra shows a subtle enhancement in charge state, but significant adduction (Figure 7.4b). At a lower electrospray voltage of 0.56 kV, ions are observed at higher charge states and with additional adduction (Figure 7.4b). Collisionally activating these ions (165 V Trap Collision Energy) results in a mass spectrum of enhanced charge states but without adduction (Figure 7.4d). Activating the supercharged charge states does result in some charge-stripping, but enhanced charge states persist, suggesting that the enhanced charging in this experiment is not a result of adducting charge carriers. Figure 7.4d shows a summary of the mass measured for the corresponding charge states from Figure 7.4a to 7.4c. The mass spectrum obtained for ions produced from 3% sulfolane solutions at an electrospray voltage of 0.74 kV show that there is an additional ~2000 Da in adducted mass compared to ions produced from solutions without supercharging reagents. Interestingly, at an electrospray voltage of 0.56 kV the mass is not constant for each observed charge state; the mass increases with increasing charge state.
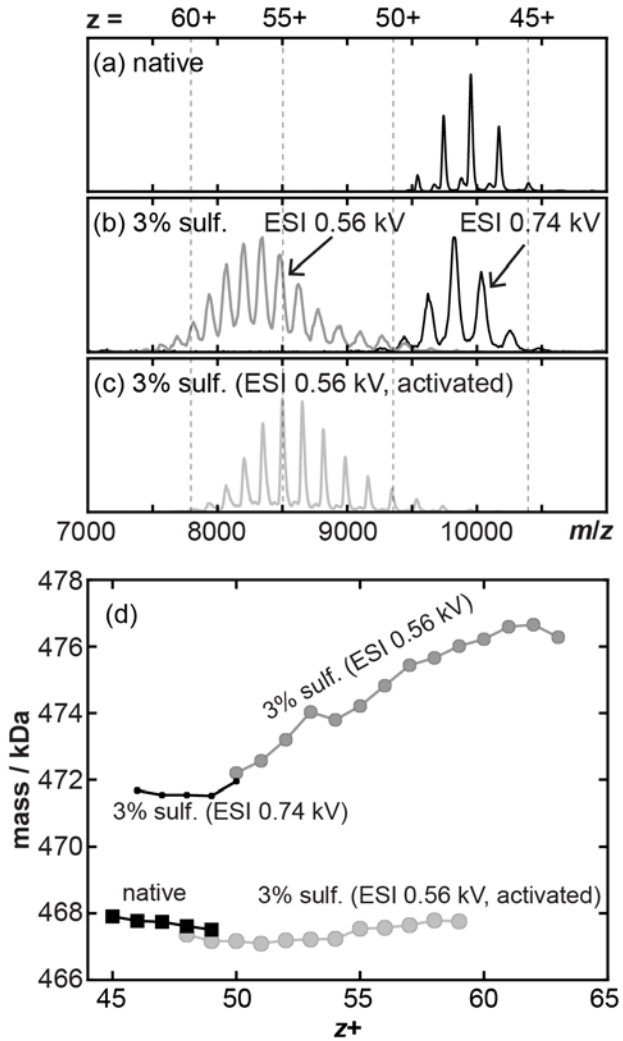
Figure 7.4. Mass spectra of β-galactosidase. (a) Ions produced from 200 mM ammonium acetate solutions. (b) Ions produced using an electrospray ionization (ESI) voltage of 0.56 or 0.74 kV from 200 mM ammonium acetate solutions with 3% sulfolane. (c) Activated ions produced using an ESI voltage of 0.56 kV from 200 mM ammonium acetate solutions with 3% sulfolane. (d) Summary of the mass measured versus charge state for mass spectra in panels a to c.

The heavily adducted mass associated with enhanced charge states in the supercharging experiments here is most consistent with a recent report by Konermann and coworkers that used MD simulations to study the mechanism of supercharging. In that study, as droplets containing sulfolane or m-NBA desolvate, the supercharging reagents are preferentially enriched and the emission of charge-carriers is impeded.[34] Any charge-carriers that do not leave the droplet during desolvation will contribute to the observed charge state of the ion. In typical native mass spectrometry experiments, charge-carriers are ejected via the ion evaporation model, and result in ion charge states that are dependent on the size of the ion and identity of the charge-carriers.[8] Thus, supercharged charge states in these experiments are a result of charge-carrier suppression that is a direct result from supercharging reagent enrichment during droplet desolvation.

7.5 Conclusions

The goal of this work was to create a unified set of data that included ion mobility mass spectrometry results of ions produced from solutions containing different supercharging reagents and concentrations. Figure 7.1 shows mass spectra for concanavalin A and bovine serum albumin electrosprayed from 200 mM ammonium acetate solutions containing 1% m-NBA, 1% sulfolane, or 3% sulfolane. In general, the results from those experiments, and the combined set of data shown in Electronic Supplementary Material Figure S7.1, show that sulfolane is more effective at supercharging the proteins and protein complexes studied here, especially at higher v/v. The effectiveness of m-NBA to increase charge states, relative to sulfolane, decreased with increasing mass. The effects of supercharging on protein structure was investigated using ion mobility. Figure 7.3a shows that the Ω values of these ions are independent of supercharging reagent identity and concentration. Figure 7.3b shows that polarity can have a significant effect

on the unfolding pathways of some ions but not on others, suggesting that the Ω dependence on supercharged charge state is likely protein specific.

Significant adduction to supercharged charge states was observed for the highest mass protein complexes studied here (Figure 7.4). The extent of adducted mass depends on electrospray conditions and increased with charge state. Likely, changing the electrospray voltage produces droplets that contain varying amounts of supercharging reagent. The supercharged charge states observed here are consistent with enrichment of supercharging reagent during droplet desolvation, which inhibits charge-carrier emission that contributes to higher observed charge states.

7.6 Acknowledgements

7.7 Supporting Information Available. The online version of this article contains supplementary material, which is available to authorized users.

7.8 References

(1)   Kebarle, P.; Verkerk, U. H. Electrospray: From Ions in Solution to Ions in the Gas Phase, What We Know Now. *Mass Spectrom. Rev.* **2009**, *28* (6), 898–917.
(2)   McAllister, R. G.; Metwally, H.; Sun, Y.; Konermann, L. Release of Native-like Gaseous Proteins from Electrospray Droplets via the Charged Residue Mechanism: Insights from Molecular Dynamics Simulations. *J. Am. Chem. Soc.* **2015**, *137* (39), 12667–12676.

(3)   Fernandez de la Mora, J. Electrospray Ionization of Large Mutliply Charged Species Proceeds via Dole's Charged Residue Mechanism. *Anal. Chim. Acta* **2000**, *406* (1), 93–104.

(4)   Dole, M.; Mack, L. L.; Hines, R. L.; Mobley, R. C.; Ferguson, L. D.; Alice, M. B. Molecular Beams of Macroions. *J. Chem. Phys.* **1968**, *49* (5), 2240–2249.

(5)   Rayleigh, L. On the Equilibrium of Conducting Masses Charged with Electricity. *Philos. Mag.* **1882**, *14*, 184–186.

(6)   Hogan, C. J.; Carroll, J. A.; Rohrs, H. W.; Biswas, P.; Gross, M. L. Charge Carrier Field Emission Determines the Number of Charges on Native State Proteins in Electrospray Ionization. *J. Am. Chem. Soc.* **2008**, *130* (22), 6926–6927.

(7)   Hogan, C. J.; Carroll, J. A.; Rohrs, H. W.; Biswas, P.; Gross, M. L. Combined Charged Residue-Field Emission Model of Macromolecular Electrospray Ionization. *Anal. Chem.* **2009**, *81* (1), 369–377.

(8)   Allen, S. J.; Schwartz, A. M.; Bush, M. F. Effects of Polarity on the Structures and Charge States of Native-Like Proteins and Protein Complexes in the Gas Phase. *Anal. Chem.* **2013**, *85* (24), 12055–12061.

(9)   Ahadi, E.; Konermann, L. Modeling the Behavior of Coarse-Grained Polymer Chains in Charged Water Droplets: Implications for the Mechanism of Electrospray Ionization. *J. Phys. Chem. B* **2012**, *116* (1), 104–112.

(10) Konermann, L.; Rodriguez, A. D.; Liu, J. On the Formation of Highly Charged Gaseous Ions from Unfolded Proteins by Electrospray Ionization. *Anal. Chem.* **2012**, *84* (15), 6798–6804.

(11) Cole, R. B.; Harrata, A. K. Solvent Effect on Analyte Charge State, Signal Intensity, and Stability in Negative Ion Electrospray Mass Spectrometry; Implications for the Mechanism of Negative Ion Formation. *J. Am. Soc. Mass Spectrom.* **1993**, *4* (7), 546–556.

(12) Wang, G.; Cole, R. B. Effect of Solution Ionic Strength on Analyte Charge State Distributions in Positive and Negative Ion Electrospray Mass Spectrometry. *Anal. Chem.* **1994**, *66* (21), 3702–3708.

(13) Iavarone, A. T.; Jurchen, J. C.; Williams, E. R. Effects of Solvent on the Maximum Charge State and Charge State Distribution of Protein Ions Produced by Electrospray Ionization. *J. Am. Soc. Mass Spectrom.* **2000**, *11* (11), 976–985.

(14) Iavarone, A. T.; Jurchen, J. C.; Williams, E. R. Supercharged Protein and Peptide Ions Formed by Electrospray Ionization. *Anal. Chem.* **2001**, *73* (7), 1455–1460.

(15) Iavarone, A. T.; Williams, E. R. Supercharging in Electrospray Ionization: Effects on Signal and Charge. *Int. J. Mass Spectrom.* **2002**, *219* (1), 63–72.

(16) Hewavitharana, A. K.; Herath, H. M. D. R.; Shaw, P. N.; Cabot, P. J.; Kebarle, P. Effect of Solvent and Electrospray Mass Spectrometer Parameters on the Charge State Distribution of Peptides – a Case Study Using Liquid Chromatography/Mass Spectrometry Method Development for Beta-Endorphin Assay. *Rapid Commun. Mass Spectrom.* **2010**, *24* (24), 3510–3514.

(17) Iavarone, A. T.; Williams, E. R. Collisionally Activated Dissociation of Supercharged Proteins Formed by Electrospray Ionization. *Anal. Chem.* **2003**, *75* (17), 4525–4533.

(18) Yin, S.; Loo, J. A. Top-down Mass Spectrometry of Supercharged Native Protein–ligand Complexes. *Int. J. Mass Spectrom.* **2011**, *300* (2–3), 118–122.

(19) Chen, X.; Westphall, M. S.; Smith, L. M. Mass Spectrometric Analysis of DNA Mixtures: Instrumental Effects Responsible for Decreased Sensitivity with Increasing Mass. *Anal. Chem.* **2003**, *75* (21), 5944–5952.

(20) Iavarone, A. T.; Williams, E. R. Mechanism of Charging and Supercharging Molecules in Electrospray Ionization. *J. Am. Chem. Soc.* **2003**, *125* (8), 2319–2327.

(21) Šamalikova, M.; Grandori, R. Protein Charge-State Distributions in Electrospray-Ionization Mass Spectrometry Do Not Appear To Be Limited by the Surface Tension of the Solvent. *J. Am. Chem. Soc.* **2003**, *125* (44), 13352–13353.

(22) Chingin, K.; Xu, N.; Chen, H. Soft Supercharging of Biomolecular Ions in Electrospray Ionization Mass Spectrometry. *J. Am. Soc. Mass Spectrom.* **2014**, *25* (6), 928–934.

(23) Cassou, C. A.; Williams, E. R. Desalting Protein Ions in Native Mass Spectrometry Using Supercharging Reagents. *Analyst* **2014**, *139* (19), 4810–4819.

(24) Going, C. C.; Xia, Z.; Williams, E. R. New Supercharging Reagents Produce Highly Charged Protein Ions in Native Mass Spectrometry. *Analyst* **2015**, *140* (21), 7184–7194.

(25) Lomeli, S. H.; Yin, S.; Ogorzalek Loo, R. R.; Loo, J. A. Increasing Charge While Preserving Noncovalent Protein Complexes for ESI-MS. *J. Am. Soc. Mass Spectrom.* **2009**, *20* (4), 593–596.

(26) Sterling, H. J.; Daly, M. P.; Feld, G. K.; Thoren, K. L.; Kintzer, A. F.; Krantz, B. A.; Williams, E. R. Effects of Supercharging Reagents on Noncovalent Complex Structure in Electrospray Ionization from Aqueous Solutions. *J. Am. Soc. Mass Spectrom.* **2010**, *21* (10), 1762–1774.

(27) Sterling, H. J.; Williams, E. R. Origin of Supercharging in Electrospray Ionization of Noncovalent Complexes from Aqueous Solution. *J. Am. Soc. Mass Spectrom.* **2009**, *20* (10), 1933–1943.

(28) Grimm, R. L.; Beauchamp, J. L. Evaporation and Discharge Dynamics of Highly Charged Multicomponent Droplets Generated by Electrospray Ionization†. *J. Phys. Chem. A* **2010**, *114* (3), 1411–1419.

(29) Sterling, H. J.; Prell, J. S.; Cassou, C. A.; Williams, E. R. Protein Conformation and Supercharging with DMSO from Aqueous Solution. *J. Am. Soc. Mass Spectrom.* **2011**, *22* (7), 1178–1186.

(30) Hogan Jr., C. J.; Ogorzalek Loo, R. R.; Loo, J. A.; Mora, J. F. de la. Ion Mobility–mass Spectrometry of Phosphorylase B Ions Generated with Supercharging Reagents but in Charge-Reducing Buffer. *Phys. Chem. Chem. Phys.* **2010**, *12* (41), 13476.

(31) Davidson, K. L.; Oberreit, D. R.; Hogan, C. J.; Bush, M. F. Droplet Sizes, Ionization Currents, and Nonspecific Aggregation in Native Electrokinetic Electrospray Ionization. *Int. J. Mass Spectrom.* **2017**, DOI: 10.1016/j.ijms.2016.09.013.

(32) Allen, S. J.; Giles, K.; Gilbert, T.; Bush, M. F. Ion Mobility Mass Spectrometry of Peptide, Protein, and Protein Complex Ions Using a Radio-Frequency Confining Drift Cell. *Analyst* **2016**, *141*, 884–891.

(33) Mason, E. A.; McDaniel, E. W. *Transport Properties of Ions in Gases*, pg. 276.; Wiley: New York, 1988.

(34) Metwally, H.; McAllister, R. G.; Popa, V.; Konermann, L. Mechanism of Protein Supercharging by Sulfolane and M-Nitrobenzyl Alcohol: Molecular Dynamics Simulations of the Electrospray Process. *Anal. Chem.* **2016**, *88* (10), 5345–5354.

APPENDIX A

Useful Equations and Relationships

Mason-Schamp Equation:

$$\Omega = \frac{3ez}{16N} \sqrt{\frac{2\pi}{\mu k_B T}} \frac{1}{K} \tag{A.1}$$

Define K (mobility) and N (gas number density):

$$K = K_0 \frac{T}{T_0} \frac{P_0}{P} \tag{A.2}$$

$$N = \frac{n}{V} \tag{A.3}$$

$$N_0 = \frac{n}{V_0} = \frac{P_0}{RT_0} N_a \tag{A.4}$$

$$N_a = Avogadro's\ Constant = 6.02214057\ x\ 10^{23}\ mol^{-1}$$

$$P_0 = 760\ Torr$$

$$T_0 = 273.15\ K$$

$$R = 62.363577\ \frac{L\ Torr}{K\ mol}$$

Express Equation A.4 using the above values to arrive at Avogadro's constant and the volume of an ideal gas:

$$N_0 = \frac{N_a}{22.4139619\ \frac{L}{mol}} \tag{A.5}$$

Convert N_0 to N:

$$\frac{T}{P} N = N_0 \frac{T_0}{P_0} \tag{A.6}$$

Combine equations A.5 and A.6:

$$\frac{T}{P} N = \frac{N_a}{22.4139619 \frac{L}{mol}} \frac{T_0}{P_0} \tag{A.7}$$

Rearrange:

$$N = \frac{N_a}{22.4139619 \frac{L}{mol}} \frac{T_0}{T} \frac{P}{P_0} \tag{A.8}$$

Combine equations A.1, A.2, and A.8:

$$\Omega = \frac{3ez}{16} \sqrt{\frac{2\pi}{\mu k_B T}} \frac{1}{K_0} \frac{T_0}{T} \frac{P}{P_0} \frac{22.4139619 \frac{L}{mol}}{N_A} \frac{T}{T_0} \frac{P_0}{P} \tag{A.9}$$

Cancel out pressures/temperatures and separate constants from experimental inputs:

$$\Omega = \left(\frac{z}{K_0} \sqrt{\frac{1}{\mu T}} \right) \quad \left(\frac{3e}{16} \frac{22.4139619 \frac{L}{mol}}{N_A} \sqrt{\frac{2\pi}{k_B}} \right) \tag{A.10}$$

The first half of equation A.10 contains experimental inputs and the second half contains

constants:

$$e = elementary\ charge = 1.60217662\ x\ 10^{-19}\ C\ \left(\frac{kg\ m^2}{s^2\ V} \right)$$

$$C = Coulomb = \frac{kg\ m^2}{s^2\ V}$$

$$k_B = Boltzmann\ Constant = 1.38062485\ x\ 10^{-23}\ \frac{kg\ m^2}{s^2\ K}$$

The first half of equation A.10 will have units of:

$$\frac{V\ s}{cm^2} \sqrt{\frac{1}{Da\ K}} \tag{A.11}$$

Correct the second half of equation A.10 by adding in the unified atomic mass unit (Da) to kg

conversion, and other stoichiometry:

$$Da = Dalton = 1.66053904\ x\ 10^{-27}\ kg$$

$$\Omega = \left(\frac{z}{K_0}\sqrt{\frac{1}{\mu T}}\right) \quad \left(\frac{3e}{16}\frac{22.4139619\frac{L}{mol}}{N_A}\sqrt{\frac{2\pi}{k_B}}\right)\left(\frac{0.001\ m^3}{1\ L}\right)\left(\frac{10000\ cm^2}{1\ m^2}\right)\sqrt{\frac{1}{Da}} \tag{A.12}$$

Add in a conversion to go from m^2 to angstroms squared (Å^2):

$$\Omega = \left(\frac{z}{K_0}\sqrt{\frac{1}{\mu T}}\right) \quad \left(\frac{3e}{16}\frac{22.4139619\frac{L}{mol}}{N_A}\sqrt{\frac{2\pi}{k_B}}\right)\left(\frac{0.001\ m^3}{1\ L}\right)\left(\frac{10000\ cm^2}{1\ m^2}\right)\sqrt{\frac{1}{amu}}\left(\frac{1\ x\ 10^{20}\text{Å}^2}{1\ m^2}\right) \tag{A.13}$$

Calculating all of this out:

$$\Omega = \left(\frac{z}{K_0}\sqrt{\frac{1}{\mu T}}\right)\ 18510.022 \tag{A.14}$$

Validate unit cancellation:

$$\frac{V\ s}{cm^2}\sqrt{\frac{1}{Da\ K}}\quad \frac{kg\ m^2}{s^2\ V}\ \frac{L}{mol}\,mol\sqrt{\frac{K\ s^2}{m^2\ kg}}\ \frac{m^3\ cm^2}{L\ m^2}\sqrt{\frac{Da\ A^2}{kg\ m^2}} \tag{A.15}$$

We arrive at Ω that are in Angstroms squared.

APPENDIX B

Collision Cross Section Values

Tables are reproduced from the Supporting Information of Chapter 3.

Table B.1 Collision cross sections with helium and nitrogen gas (Ω_{He} and Ω_{N2}, respectively) of poly-DL-alanine anions $(Ala_n - zH)^{z-}$ and Ω_{He} of poly-DL-alanine cations $(Ala_n - zH)^{z+}$. The monoisotopic mass of oligomers (n) are provided. Mobility measurements were conducted in 2.0 Torr helium or 1.5 Torr nitrogen gas. Note, improved transmission of lower-mobility ions was observed when the pressure of nitrogen gas from dropped from 2.0 to 1.5 Torr. Ω values were determined by measuring drift times for 10 different drift voltages ranging from 104 to 354 V.

	z	1+	1−	1−	2+	2−	2−
n	mass	Ω_{He} / Å^2	Ω_{He} / Å^2	Ω_{N2} / Å^2	Ω_{He} / Å^2	Ω_{He} / Å^2	Ω_{N2} / Å^2
3	231.1	88	89	150			
4	302.2	99	104	165			
5	373.2	113	117	179			
6	444.2	126	131	195			
7	515.3	139	143	209			
8	586.3	156	155	223			
9	657.3	169	167	238			
10	728.4	181	179	253			
11	799.4	192	190	267	196	202	297
12	870.5	204	200	279	205	215	309
13	941.5	215	213	294	215	226	322
14	1012.5	226	226	308	226	237	333
15	1083.6	238	237	322	239	248	344
16	1154.6	249	248	335	250	257	355
17	1225.6		260	348	262	267	366
18	1296.7		271	361	272	277	377
19	1367.7		283	374	287	286	387
20	1438.8		294	387	294	296	399
21	1509.8		305		310	306	410
22	1580.8		317		315	316	422
23	1651.9		329		330	327	434
24	1722.9				335	337	445
25	1793.9				349	347	457
26	1865.0				356	358	469
27	1936.0					367	481
28	2007.0					378	492
29	2078.1					389	

Table B.2 Collision cross section values of small molecule, peptide, denatured protein, and native-like protein and protein complex cations ($\Omega+$) and anions ($\Omega-$) measured in 2.0 Torr helium gas. Oligomeric states (n), charge (z), and mass are provided. [†] symbol represents values previously reported in Allen et al. *Anal. Chem.* **2013**, *85*, 12055 – 12061.

	Sample	n	mass (Da)	z	$\Omega+$ / nm^2	$\Omega-$ / nm^2
Small Molecules	N-ethylaniline	1	121.1	1	0.63	-
	acetominophen	1	151.1	1	0.67	0.67
	alprenolol	1	149.2	1	0.97	-
	ondanestron	1	293.2	1	1.05	1.06
	clozapine N-oxide	1	342.2	1	1.12	1.13
	betamethasone	1	392.2	1	1.15	1.15
	dexamethasone	1	392.2	1	1.16	1.15
	colchicine	1	399.2	1	1.30	1.29
	verapamil	1	454.3	1	1.42	-
	reserpine	1	609.2	1	1.77	-
Peptides	GRGDS	1	490	1	1.32	1.26
				2	1.41	1.44
	SDGRG	1	490	1	1.30	1.26
				2	1.44	1.42
	leucine enkephalin	1	555.6	1	1.57	1.52
	bradykinin	1	1060	2	2.41	-
Denatured Proteins	denatured ubiquitin *bovine erythrocytes*	1	8.57k	9	16.5	-
				10	17.3	-
				11	18.2	-
				12	19.1	-
				13	19.8	-
	denatured cytochrome *c* *equine heart*	1	12.4k	13	23.6	-
				14	24.8	-
				15	25.7	-
				16	26.4	-
				17	27.2	-
				18	27.8	-
				19	28.4	-
				20	28.7	-

	Sample	*n*	mass	*z*	Ω+ / nm²	Ω– / nm²
Denatured Proteins	denatured myoglobin	1	16.9k	19	35.9	-
	equine heart			20	36.7	-
				21	37.4	-
				22	38.0	-
				23	38.5	-
				24	39.0	-
				25	39.4	-
				26	39.9	-
				27	40.4	-
Native-like Proteins and Protein Complexes	insulin[†]	1	5.81k	3	7.43	7.28
	recombinant human			4	7.68	7.32
	ubiquitin[†]	1	8.57k	4	9.72	9.50
	bovine erythrocytes			5	9.82	9.60
	insulin[†]	2	11.6k	5	12.3	11.8
	recombinant human			6	12.9	12.0
	cytochrome *c*[†]	1	12.4k	5	-	12.4
	equine heart			6	12.4	12.5
				7	13.0	-
	ribonuclease A	1	13.8k	5	-	13.0
	bovine pancreas			6	12.9	13.0
				7	13.4	-
				8	13.9	-
	α-lactalbumin	1	14.2k	5	-	13.5
	bovine milk			6	13.6	13.5
				7	13.8	13.8
				8	14.4	-
	lysozyme	1	14.3k	5	-	13.5
	chicken egg white			6	13.6	13.6
				7	13.7	14.0
				8	14.6	-
	β-lactoglobulin[†]	1	18.4k	6	-	16.6
	bovine milk			7	16.7	16.6
				8	17.1	-
				9	18.0	-
	α-chymotrypsinogen A	1	25.7k	7	-	20.4
	bovine pancreas			8	-	20.2
				9	20.2	20.3
				10	20.3	-
				11	21.1	-

Sample	*n*	mass	*z*	Ω+ / nm²	Ω– / nm²
carbonic anhydrase	1	31.5k	8	-	24.9
bovine erythrocytes			9	-	24.8
			10	24.3	25.2
			11	24.3	-
			12	24.5	-
insulin[†]	6	35.3k	10	24.0	23.7
recombinant human			11	24.1	23.7
β-lactoglobulin[†]	2	36.8k	8	-	25.9
bovine milk			9	-	27.9
			10	-	27.9
			11	28.4	-
			12	29.0	-
			13	29.9	-
ovalbumin	1	43.3k	11	30.1	30.5
egg white			12	30.1	30.5
			13	30.4	-
			14	30.5	-
avidin[†]	4	64.3k	12	-	36.2
egg white			13	-	36.4
			14	-	36.4
			15	35.7	-
			16	35.9	-
			17	36.1	-
			18	36.2	-
albumin[†]	1	67.0k	12	-	40.0
bovine serum			13	-	40.5
			14	40.1	40.8
			15	40.3	41.2
			16	40.7	-
			17	41.1	-
holotransferrin	1	78.6k	14	-	44.1
bovine			15	-	44.7
			16	-	45.0
			17	44.2	45.2
			18	45.0	-
			19	45.4	-
			20	45.7	-

Native-like Proteins and Protein Complexes

Sample	n	mass	z	$\Omega+$ / nm²	$\Omega-$ / nm²
lactoferrin	1	81.0k	15	-	45.8
human milk			16	-	45.9
			17	-	46.3
			18	45.9	-
			19	46.4	-
			20	46.3	-
			21	46.7	-
enolase	2	93.9k	15	-	48.7
saccharomyces cerevisiae			16	-	48.8
			17	-	48.7
			18	48.0	-
			19	48.3	-
			20	48.4	-
			21	48.7	-
concanavalin A[†]	4	103k	16	-	54.2
jack bean			17	-	54.5
			18	-	54.6
			19	54.4	54.6
			20	54.5	-
			21	54.6	-
			22	54.6	-
glyceraldehyde-3-phosphate dehydrogenase	4	145k	20	-	69.5
			21	-	70.0
rabbit muscle			22	-	70.0
			23	68.6	70.0
			24	69.6	70.1
			25	69.9	-
			26	70.0	-
			27	70.6	-
alcohol dehydrogenase[†]	4	148k	19	-	69.9
saccharomyces cerevisiae			20	-	70.2
			21	-	69.8
			22	-	70.3
			23	69.9	70.1
			24	70.2	-
			25	70.2	-
			26	70.2	-
			27	70.2	-

Native-like Proteins and Protein Complexes

Sample	n	mass	z	$\Omega+$ / nm^2	$\Omega-$ / nm^2
aldolase	4	158k	20	-	78.0
rabbit muscle			21	-	77.9
			22	-	77.6
			23	-	77.7
			24	76.1	-
			25	76.9	-
			26	77.2	-
			27	77.3	-
phosphorylase b	2	196k	24	-	90.3
rabbit muscle			25	-	90.6
			26	-	90.4
			27	90.3	90.6
			28	90.7	-
			29	90.9	-
			30	91.2	-
pyruvate kinase[†]	4	233k	24	-	103
rabbit muscle			25	-	104
			26	-	104
			27	-	103
			28	-	103
			29	-	102
			30	101	-
			31	102	-
			32	102	-
			33	102	-
			34	102	-
			35	102	-
catalase	4	236k	24	-	90.3
bovine liver			25	-	90.7
			26	-	91.2
			27	-	91.0
			32	90.5	-
			33	90.6	-
			34	90.5	-
			35	90.9	-
			35	90.5	-

Native-like Proteins and Protein Complexes

Native-like Proteins and Protein Complexes

Sample	*n*	mass	*z*	$\Omega+$ / nm^2	$\Omega-$ / nm^2
glutamate dehydrogenase[†]	6	337k	31	-	127
bovine liver			32	-	128
			33	-	128
			34	-	128
			35	125	128
			36	127	128
			37	127	128
			38	127	-
			39	127	-
			40	128	-
			41	128	-
β-galactosidase[†]	4	468k	36	-	163
Escherichia coli			37	-	164
			38	-	165
			39	-	166
			40	-	167
			41	-	168
			42	-	169
			47	165	-
			48	165	-
			49	166	-
			50	165	-
			51	165	-